Δ Electroproduction in ^{12}C

Steven T M^{c}Lauchlan

Presented as a Thesis for the Degree of Doctor of Philosophy

Nuclear Physics Experimental Group
Department of Physics and Astronomy
University of Glasgow

January 2003

Abstract

The Δ-nucleus potential is a crucial element in the understanding of the nuclear system. Previous electroexcitation measurements in the Δ region reported a Q^2 dependence of the Δ mass indicating that this potential is dependent on the momentum of the Δ. Such a dependence is not observed for protons and neutrons in the nuclear medium. This thesis presents the experimental study of the electroexcitation of the Δ resonance in ^{12}C, performed using the high energy electron beam at the Thomas Jefferson National Accelerator Facility, and the near 4π acceptance detector CLAS that enables the detection of the full reaction final state.

Inclusive, semi inclusive, and exclusive cross sections were measured with an incident electron beam energy of $1.162\,GeV$ over the Q^2 range $0.175 - 0.475$ $(GeV/c)^2$. A Q^2 dependence of the Δ mass was only observed in the exclusive measurements indicating that the Δ-nucleus potential is affected by the momentum of the Δ.

Acknowledgements

Firstly, I would like to thank my supervisor, Dr. D Ireland, for all his help and guidance throughout the course of this project. Thanks to all members of the Nuclear Physics Experimental Group, past and present, including Ken Livingston, Bob Owens, and Günther Rosner.

Thank you to Westley for sharing my sufferings as a JLab PhD student and for allowing me to realise my true vocation as a computer programmer. Also to Andreas for putting up with my unrelenting moans about physics and football, cricket, skiing, snow boarding, snooker, tennis, American football, baseball, basketball...

Thank you to the E2 run group for providing support and knowledge when required, particularly Derek Branford, Stepan Stepanyan, Larry Weinstein, Maurik Holtrop, Bin Zhang, Rustam Niyazov, and Dan Protopopescu. Also to the Engineering and Physical Sciences Research Council and the Nuclear Physics Experimental Group for providing financial support and travel expenses during my time as a student.

As always, I owe much gratitude to my Gran for her never ending (financial) support.

Finally, love and thanks to Ruth - without your support and encouragement this thesis would not have been completed on time.

Declaration

The data presented in this thesis were obtained as part of the e2a run group for the CLAS Collaboration at Jefferson Laboratory, Virginia, USA. I participated fully in the execution of the experiment. The analysis of the experimental data is entirely my own work. This thesis was composed by myself.

<u>**Steven T M^c^Lauchlan**</u>

January 2003

Contents

List of Figures

List of Tables

Chapter 1

Introduction and Theory

1.1 Introduction

The nucleus can be viewed as an interacting system of nucleons, pions and the Δ resonance [1]. The protons and neutrons make up the majority of the nucleus with the pions carrying the force that binds them. Higher energy nucleons interacting in the nucleus can excite Δ resonances. The contribution of Δ particles in the nucleus is estimated at $1 - 2\%$ of the total wave function in two and three nucleon systems and there is no reason to suggest that it should be any smaller at higher A nuclei [2]. Therefore, for a complete theoretical description and understanding of the nucleus, the potential that the Δ experiences is a crucial element to understand. The aim of this investigation was to study the mass of the Δ resonance. It was reported in the work of Sealock *et al.* [3] that the mass of the Δ varied with its momentum. This implies that the potential the Δ experiences in the nucleus is dependent on its momentum. The potential that nucleons (protons and neutrons) experience in nuclei does not exhibit this type of dependence [4]. Sealock and O' Connell extended their analysis and derived a momentum dependent potential that described their observations [5].

Electroproduction of nucleon resonances in nuclei is a good tool for studying the effect that the strong force has on baryon structure. Since the interaction of electrons with nuclei and nucleons is electromagnetic, the initial reaction mechanism is well understood and the results of an experiment can be directly related to nuclear properties [6]. This is not the case for strongly interacting probes where it is necessary to separate the effects of the poorly understood reaction mechanisms from the nuclear structure effects [6]. The entire volume of the nucleus is probed using electron scattering, allowing a better estimation of the medium effects being studied. Furthermore, the interaction is weak so the structure of the target is not greatly disturbed by the measurement process [6].

Particle	Quark Content	I_3	Charge
Δ^-	ddd	$-3/2$	-1
Δ^0	udd	$-1/2$	0
Δ^+	uud	$+1/2$	$+1$
Δ^{++}	uuu	$+3/2$	$+2$

Table 1.1: Properties of the Δ resonance.

1.2 The $\Delta\,(1232)$ Resonance

Protons and neutrons can be thought of as different charge substates of the nucleon. Nucleons are ascribed a quantum number, isospin (I)[1], with value $I = \frac{1}{2}$ and two substates $I_3 = \pm\frac{1}{2}$ [7]. The charge of a nucleon is then $Q/e = \frac{1}{2} + I_3$, if $I_3 = +\frac{1}{2}$ for the proton and $I_3 = -\frac{1}{2}$ for the neutron. Isospin is a useful quantum number because it is conserved in strong interactions [7]. Consequently, strong interactions depend on I and not I_3. The strong interactions between nucleons are described by I and we do not distinguish between protons and neutrons. The Δ resonance has an isospin of $\frac{3}{2}$ with four degenerate substates $I_3 = \pm\frac{3}{2}, \pm\frac{1}{2}$. These correspond to the four charge states of the Δ (see table 1.1). To obtain an isospin of $\frac{3}{2}$, the spins of the individual quarks comprising the Δ must all be aligned. In fact in the $N \to \Delta$ transition, both the spin and isospin change from $\frac{1}{2}$ to $\frac{3}{2}$. In an electron scattering experiment no charge is exchanged between the electron and target nucleon so the only possible excitations are the Δ^0 and Δ^+. The other two can be excited in charge exchange reactions. Therefore in the context of this experiment the Δ resonance is thought of as the lowest lying excited state of the nucleon that has different quantum numbers but the same quark content.

The Δ, being a resonance, has a mass and lifetime of existence before decaying. An example W excitation spectrum of the proton is shown in figure 1.1. The details of the method for obtaining this spectrum are discussed in section 1.3. On the plot, the Δ resonance is shown. The free Δ has a mass of $1.230 - 1.234\,GeV/c^2$ and a width of $0.115 - 0.125\,GeV/c^2$ [8]. It decays via the strong interaction in a time of the order of $10^{-24}\,s$ with a branching ratio of $> 99\%$ into a nucleon and a pion [8]. The other decay mechanism is $\Delta \to N\gamma$. This is very inefficiently detected in this experimental setup. As far as we are concerned this does not contribute and is not considered any further.

In the nuclear medium the Δ resonance demonstrates different properties to those of the free Δ due to processes that are unique to Δ production in nuclei. The width of the Δ resonance is increased as a result of the Fermi motion of the nucleons smearing the position of the peak. When the nucleon decay particle has an energy below the Fermi

[1] Low energy nuclear physicists usually refer to isospin as T. The notation used in [7] was followed here.

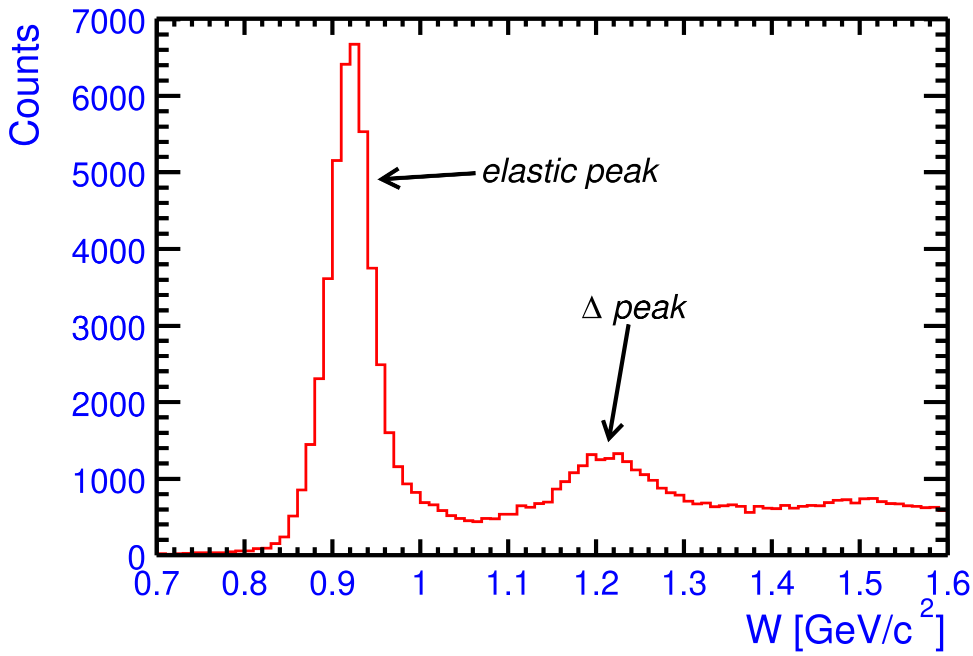

Figure 1.1: Example W spectrum for ^1H. The elastic and Δ peaks are shown.

level, Pauli blocking increases the lifetime of the Δ and as a result reduces the width of the resonance [9]. Finally, an important additional decay channel is available to the Δ in a nucleus which has a greater effect than Pauli blocking. The $N + \Delta \rightarrow N + N$ interaction increases the width of the resonance [9]. All these effects combine to alter the width of the Δ in the nuclear medium compared with the free Δ. However, it is thought that these processes do not contribute to a shift in the Δ peak position [10].

1.3 Electron Scattering

In electron scattering a virtual photon is transferred between the incident electron and the target (see figure 1.2). All quantities are stated in units where $\hbar = c = 1$. The excitation of a Δ resonance requires about 300 MeV of energy to be transferred to a nucleon but, by probing the nucleus with an electron, the momentum transferred can be varied independently. The virtual photon energy, ω $[GeV]$, and momentum, $\mathbf{q}$ $[GeV/c]$, are defined as follows:

$$\omega = E_e - E_{e'} \tag{1.1}$$

and

$$\mathbf{q} = \mathbf{k}_e - \mathbf{k}_{e'} \tag{1.2}$$

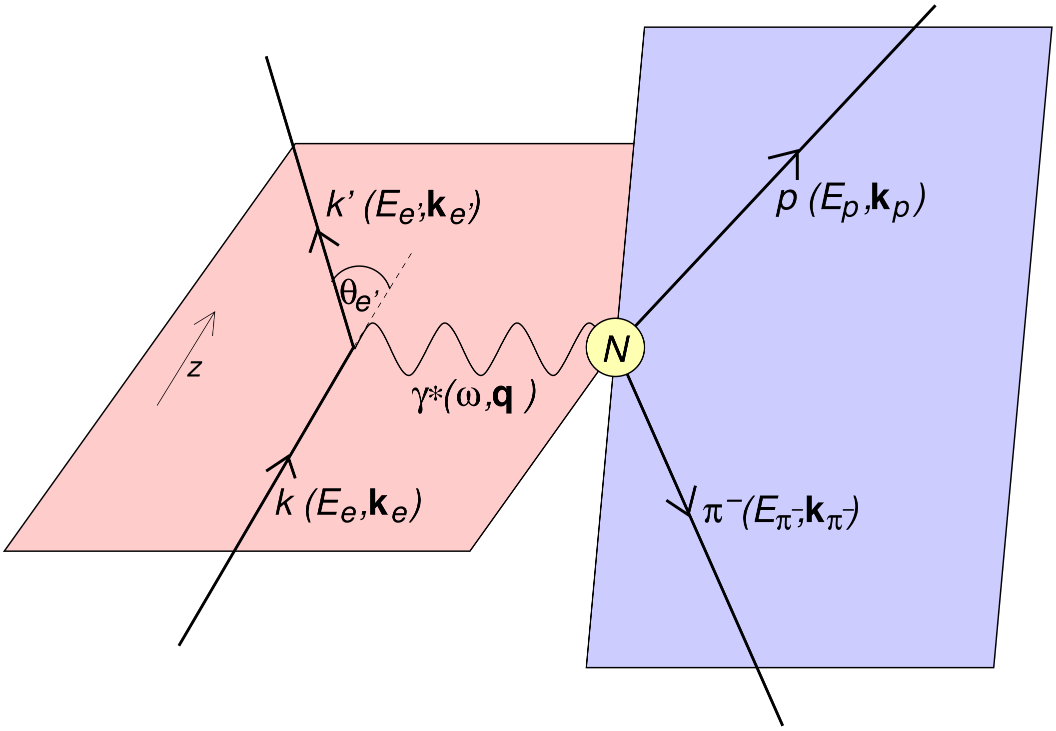

Figure 1.2: Diagram of electron scattering. The incoming electron, k, transfers a virtual photon, γ^*, to the target nucleon and scatters at an angle $\theta_{e'}$. The specific case where the product particles are a proton and π^- is shown here.

where $k = (E_e, \mathbf{k}_e)$ is the four vector of the incoming electron and $k' = (E_{e'}, \mathbf{k}_{e'})$ The invariant mass squared of the exchanged photon

$$Q^2 = \mathbf{q}^2 - \omega^2 \tag{1.3}$$

is therefore a measure of the momentum transferred to the nucleon. As Q^2 is invariant it is a good quantity to use for investigation. Where the four vector of the virtual photon is known, the mass of the recoiling hadronic system, W $[GeV/c^2]$, can be calculated as

$$W^2 = m_N^2 + 2m_N\omega - Q^2 \tag{1.4}$$

where m_N is the nucleon mass. An example W spectrum is shown in figure 1.4. The general features are discussed below in section 1.3.2.

The cross section for electron scattering can be written

$$\frac{d^2\sigma}{d\Omega dE_{e'}} = \sigma_{Mott}\left(\frac{Q^2}{\mathbf{q}^2}\right)\left\{R_L(\mathbf{q},\omega) + \epsilon^{-1}R_T(\mathbf{q},\omega)\right\} \tag{1.5}$$

where

$$\sigma_{Mott} = \left(\frac{\alpha}{2E_e}\right)^2 \frac{\cos^2(\theta_{e'}/2)}{\sin^4(\theta_{e'}/4)} \tag{1.6}$$

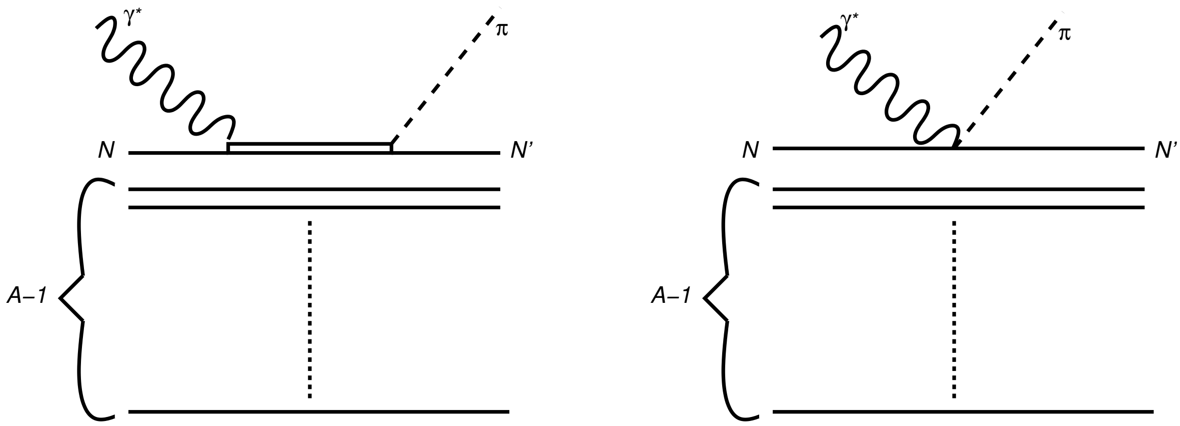

(a) Resonant pion production

(b) Non-resonant pion production

Figure 1.3: Feynman diagrams in electroexcitation of the Δ resonance.

is the Mott cross section, R_L and R_T are the longitudinal and transverse response functions, and we define

$$\epsilon^{-1} = 1 + 2\frac{\mathbf{q}^2}{Q^2}\tan^2\left(\frac{\theta_{e'}}{2}\right) \tag{1.7}$$

This is commonly used because the polarisation of the virtual photon has both longitudinal and transverse contributions which pick out the different response functions. It provides a link between real and virtual photon experiments since real photons only contain transverse polarisation. The advantage of writing the scattering cross section in this form is that the response functions can be separated experimentally by varying the electron kinematics. In a plot of the cross section as a function of ϵ^{-1}, at two or more values of the scattering angle $\theta_{e'}$, for fixed values of ω and $\mathbf{q}$, the slope gives R_L and the intercept with the vertical axis ($\epsilon^{-1} = 0$) gives R_T. This type of analysis is not performed here but is common in inclusive electron scattering experiments. However, equation 1.5 is used in the analysis of the present experiment.

1.3.1 Δ Excitation in Electron Scattering

The most important processes involved in Δ excitation in electron scattering are shown in figure 1.3. Other process contribute but these form the majority of the cross section in the Δ region. In these diagrams it is assumed that only one photon is exchanged between the incoming electron and target nucleon and also that the $(A-1)$ nucleons are spectators. Figure 1.3(a) shows the production of a pion through the excitation of the Δ resonance. Figure 1.3(b) also shows pion production but in this case there is no intermediate resonant state. This is often called the Born term. To extract the Δ production from the inclusive cross section, the contribution of non-resonant pion

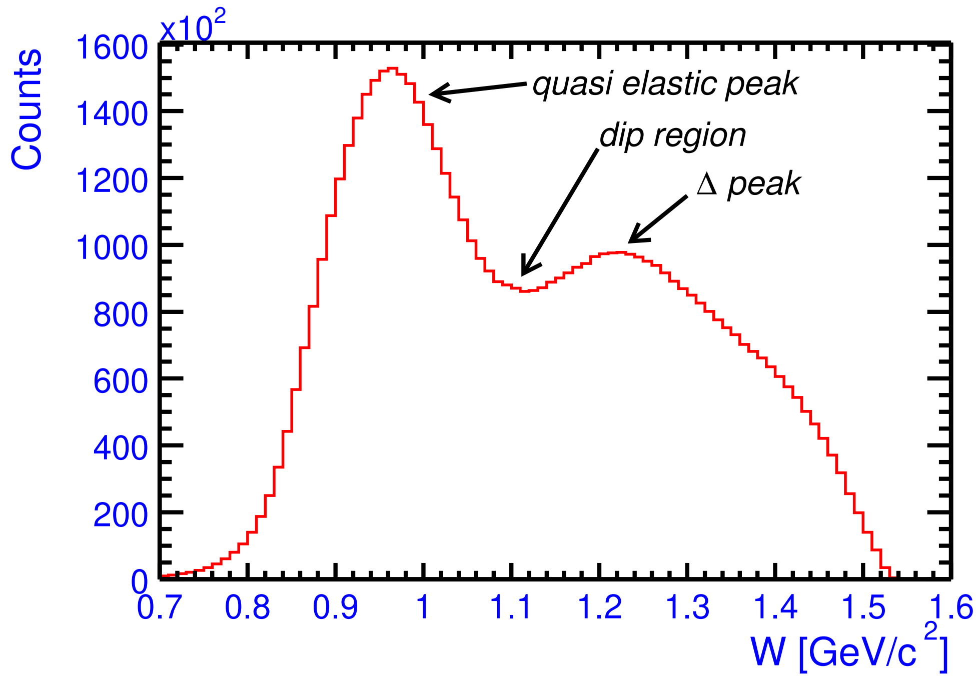

Figure 1.4: Example W spectrum for ^{12}C. The quasi elastic peak, Δ peak and dip region are shown.

production (figure 1.3(b)) must be estimated.

1.3.2 Inclusive Electron Scattering

In inclusive electron scattering only the scattered electron is detected. In the past this has been the most common type of experiment performed because only recently have high duty factor accelerators and detector systems evolved to enable the detection of more final state particles.

Detecting the scattered electron enables the momentum and the energy transferred to the nucleus or nucleon to be calculated. Using this information a W excitation spectrum can be calculated such as the example given in figure 1.4. The main features of this spectrum are the quasi elastic peak and the Δ peak. The quasi elastic peak appears where the transferred virtual photon is absorbed on a single nucleon and no excitation occurs. The properties of the Δ resonance are discussed above (section 1.2). Both the quasi elastic and Δ peaks are broadened in the nuclear medium, primarily due to Fermi motion, compared to the W spectrum for ^1H (free proton) shown in figure 1.1. The region between the quasi elastic and Δ peaks is called the "dip region". In this region the majority of the cross section is due to reactions where the virtual photon is absorbed on two interacting nucleons but tails from both the quasi elastic and Δ peaks also influence the strength of the cross section in this region. There are a number of nucleon resonances that exist above the Δ peak. In the present experiment the combination of incident electron beam energy and detector acceptance do not allow the peak regions of the higher energy resonances to be probed. However, the tails from these resonances contribute in the Δ region.

Inclusive scattering does not enable specific properties of individual reaction mechanisms to be easily investigated since all possible mechanisms are included in the analysis. The information of interest must be extracted by estimating and subtracting the contributions of "background" processes. The properties of the Δ cannot be unambiguously extracted from the inclusive excitation spectrum because the competing reaction mechanisms mentioned above, whose individual cross sections are poorly known, are responsible for a major part of the cross section.

1.3.3 Semi Inclusive Electron Scattering

Semi inclusive electron scattering involves the detection of more particles than just the scattered electron but not necessarily the full final state. Since more than one particle is detected, more complicated detector systems are required than those for an inclusive measurement.

In the particular case presented here, semi inclusive scattering refers to the detection of events where a scattered electron and a π^- are detected i.e. $^{12}C\,(e,e'\pi^-)\,X$. The resulting W spectrum contains events where a π^- is produced and thus a more limited range of reaction mechanisms are included in the data than the inclusive case. Figure 1.5 gives an example of a semi inclusive excitation spectrum. The main difference between the semi inclusive and inclusive W spectrum is that the quasi elastic peak is removed. Where a π^- is detected the contributing reaction channels are further restricted to electron-neutron interactions to conserve charge. The two body interactions are also removed. The spectrum shows the pion production threshold at around $W = 1.073\,GeV/c^2$. Non resonant pion production exists above threshold and extends above the Δ region. Tails from higher resonances that decay by emission of a π^- still contribute in the Δ region. Since the complete final state is not detected it is not possible to restrict the contamination using the kinematics of the event.

1.3.4 Exclusive Electron Scattering

In exclusive electron scattering the whole final state is detected for each event. Therefore, the interaction of interest can be isolated. Detector systems for this type of analysis are very complicated and have only become available recently. In the context of this thesis the exclusive analysis refers to the reaction channel $^{12}C\,(e,e'p\pi^-)^{11}\,C$. A large acceptance is required to detect three final state particles and acquire enough

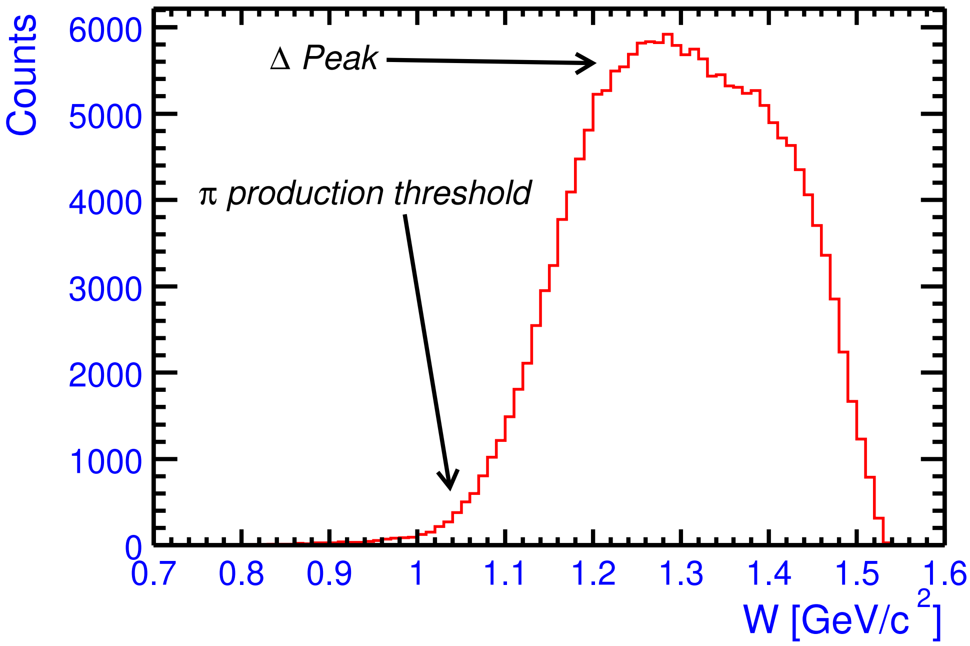

Figure 1.5: Example semi inclusive W spectrum. The Δ peak and π production threshold are shown.

statistics to perform an analysis.

Detecting the final state particles that are being studied is not enough to class the event exclusive. For example, the residual nucleus can be left in an excited state and decay to the ground state emitting a particle that is not detected. The incident or scattered electron could radiate a photon (see section 1.3.5) rendering the event semi inclusive. These contaminations can be excluded using the kinematics of the exclusive channel. The mass of the recoiling system can be calculated and events where the residual system is in the ground state are classed exclusive. An example of a W spectrum, calculated in the exclusive case, is shown in figure 1.6. The spectrum has some of the features of the semi inclusive spectrum. The pion production threshold is shown again around $W = 1.073\, GeV/c^2$. The data covers the same range in W as defined by the beam energy (and detector acceptance). However, the shape of the distribution is different to the semi inclusive case. In the exclusive case more of the background processes are rejected resulting in a shape more like the classical resonance distribution.

1.3.5 Radiative Corrections

Electron scattering data requires radiative corrections. There are three reasons why an electron may have lost more energy than given by the experimental kinematics [6]:

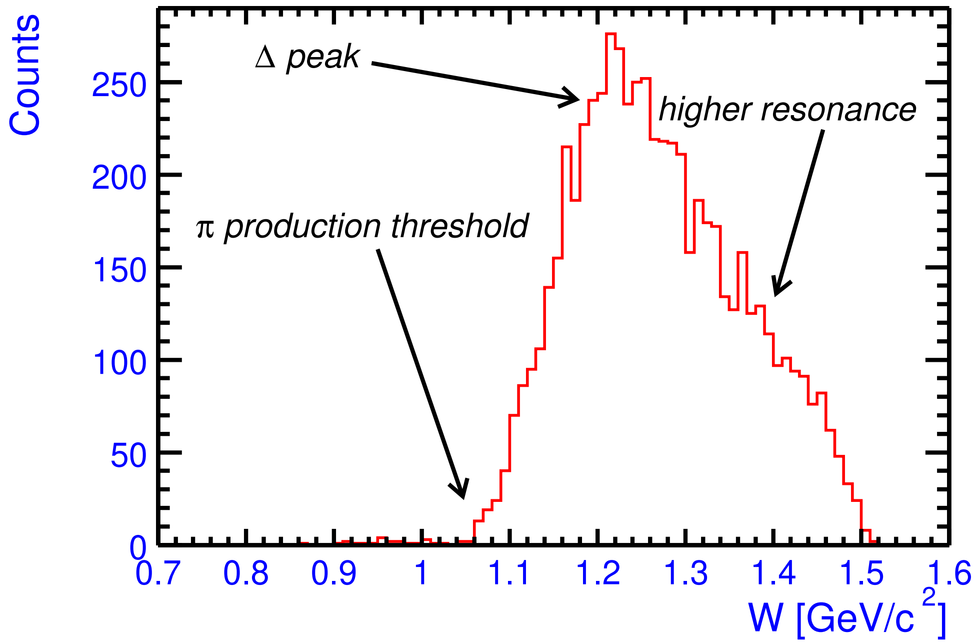

Figure 1.6: Example exclusive W spectrum. The Δ peak, π production threshold and contribution from a higher resonance are shown.

- ionisation of target atoms (Landau straggling);
- bremsstrahlung in the Coulomb field of the target atoms (external bremsstrahlung);
- bremsstrahlung in the Coulomb field of the atom where the nuclear scattering takes place (internal bremsstrahlung) (see figure 1.7).

The radiative processes introduce tails to lower energy on the peaks in experimental spectra. The measured cross sections are further influenced by the processes shown in figure 1.7. To obtain values such as peak positions from cross sections, a radiative correction must be applied to experimental data. The correction for the processes in figure 1.7 is called the Schwinger correction [6] and has to be applied to the measured cross sections.

Radiative corrections for this experiment are discussed in section 4.7.

1.4 Previous Measurements

Inclusive electron scattering in the Δ region for a range of targets has been studied at a range of values of Q^2 [3, 5, 11–21]. All these data show that the cross section per nucleon is independent of A at the Δ peak implying quasi free Δ production from individual nucleons.

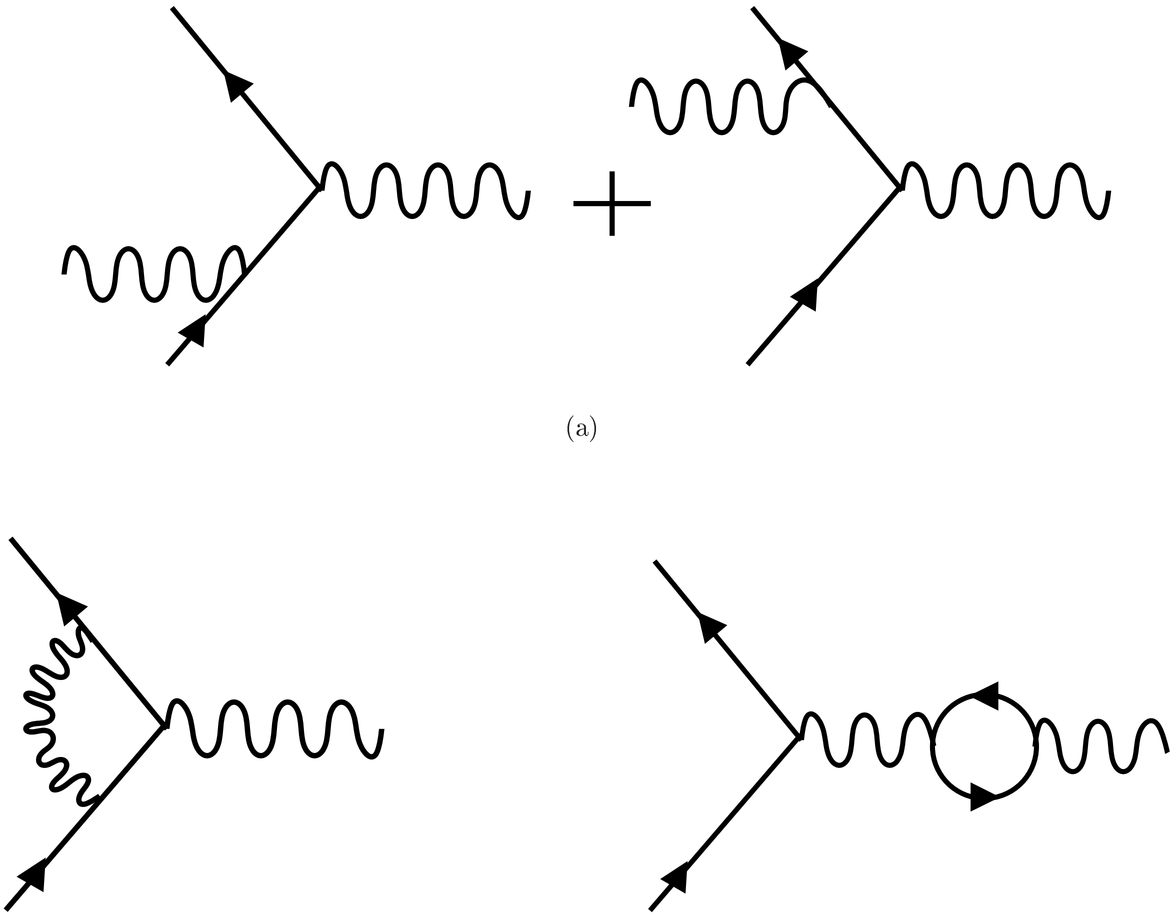

(a)

(b)

(c)

Figure 1.7: Radiative processes in electron scattering: (a) is internal bremsstrahlung and processes (b) and (c) also influence the measured cross section.

The earliest of these measurements were made by Titov *et al.* with Q^2 near 0.2 and 0.3 $(GeV/c)^2$. They measured the elastic scattering of electrons with energies $1.000 - 1.178\,GeV$ by C, Al, Ni, Mo, and W in the scattering angle interval $20 - 60°$ [11–13] and on the inelastic scattering of $1.180\,GeV$ electrons at angles of $15 - 55°$ by ^6Li and protons in a liquid hydrogen target [14]. These measurements were performed using the electron beam from the LUÉ-2000 linear accelerator at the Physico-technical institute of the Ukranian Academy of Sciences. However, the energy resolution and statistical accuracy were insufficient to determine nuclear-medium effects on resonances [3].

In 1974 Heimlich *et al.* [15] reported measurements of electron scattering from ^6Li and ^{12}C for invariant masses of the hadronic system $W \leq 1.5\,GeV/c^2$ and four momentum transfers in the range $0.2 \leq Q^2 \leq 0.4$ $(GeV/c)^2$ at the electron facility at DESY, Hamburg. A re-analysis was presented by Glawe *et al* [16] in 1979. The scattered electrons were detected with a spectrometer that consisted of a bending magnet with a homogeneous field, four wire spark chambers with ferrite-core readout, and scintillation counters, including a shower counter resulting in a spectrometer covering a solid angle of $0.69\,msr$. An additional Cerenkov counter was used to test the pion background. Since the scattering angle of each detected electron was measured, the angular dependence of the energy could be taken into account, improving the energy resolution of the spectrometer and leading to $\Delta p/p = 1.2\%$ FWHM for the scattered electrons. The resulting electron spectra demonstrated a prominent quasi elastic peak and a smaller Δ resonance peak. Comparison of the cross section from the two nuclei with that from the free electron-nucleon cross section demonstrated no dependence on either Q^2 or A.

Barreau *et al.* [17] investigated deep inelastic scattering from ^{12}C in the momentum transfer interval $0.2 \leq |q| \leq 0.6\,GeV/c$ at the electron scattering facilities of the Saclay Linear Accelerator. The detector array in the focal plane of the spectrometer consisted of two multiwire proportional counter chambers and a plane of plastic scintillators with a set of Cerenkov detectors to aid the rejection of the pion background [22, 23]. The resulting pion electroproduction cross section at an electron energy of $0.68\,GeV$ and scattering angle of $36°$ ($Q^2 = 0.09$ $(GeV/c)^2$) indicated a Δ resonance position in the nucleus $30\,MeV/c^2$ lower than that of the free nucleon resonance in agreement with results for real photons [24]. However at an electron scattering angle of $60°$, i.e. at a higher momentum transfer ($Q^2 = 0.13\,(GeV/c)^2$), the position of the Δ resonance was closer to that of the free one indicating a Q^2 dependence of the position of the Δ peak.

O'Connell *et al.* [18,19] measured inclusive cross sections for the proton and nuclear targets of ^4He, ^9Be, ^{12}C, and ^{16}O for $0.537\,GeV$ and $0.730\,GeV$ electrons scattered at $37.1°$ at the Bates Linear Accelerator [25, 26]. The scattered electrons were detected using a magnetic spectrometer with a focal plane array of wire chambers and a gas

Cerenkov detector [27–29]. Pion background rejection was achieved by requiring a coincidence between events detected at the flowing-gas Cerenkov detector and the wire chambers. The Δ peaks in the resulting cross sections demonstrated the same shape for all the nuclei studied and were clearly broadened compared to the free proton peak. The cross sections per nucleon integrated over the Δ peak were observed to be 34% greater for light nuclei than for the proton. While there was a clear shift of the quasi free peak to higher energy loss with increasing A, no evidence of any such shift in the Δ peak position was observed but there was the hint of a shift to lower energy loss relative to the free proton Δ peak (by $\sim 10\,MeV$).

Meziani *et al.* [20] studied deep inelastic inclusive electron scattering on ^{40}Ca, ^{48}Ca, and ^{56}Fe at scattering angles of $60°$, $90°$, and $140°$ with incident energies ranging from 0.120 to $0.695\,GeV$ at the Saclay Linear Accelerator. This utilised the same experimental procedure as that of Barreau *et al.* discussed above [17] and also demonstrated a Δ resonance peak position at a higher energy loss than the free nucleon resonance at an incident energy of $0.695\,GeV$ and $60°$ scattering angle ($Q^2 = 0.16\ (GeV/c)^2$), the same region of momentum transfer as [17].

Baran *et al.* also studied electroproduction of the Δ resonance [21]. Measurements were made on C and Fe at the Stanford Linear Accelerator Laboratory at scattering angles from $11.9°$ to $13.5°$ for beam energies of 1.3, 1.5, and $1.65\,GeV$ and at scattering angles from $33°$ to $53°$ for $0.653\,GeV$ corresponding to $Q^2 = 0.1\ (GeV/c)^2$. As for the measurements discussed above, the cross section per nucleon was found to be independent of A in the Δ region. The quasi free $(e, e'N)$ peak in Fe was broader than that of carbon because of the increased Fermi momentum, and a quasi free tail appeared to extend into the region between the two peaks.

Sealock *et al.* [3] presented a systematic study of Δ electroexcitation in nuclei, measuring the inclusive electron scattering cross sections for $A = 1$ to 184 (targets ^1H, ^4He, C, Fe, and W) in order to cover the widest practical range of nuclear volume, density, and binding energy. Incident electron energies of 0.96, 1.1, 1.3, and $1.5\,GeV$ were used and the scattered electrons were measured at an angle of $37.5°$ corresponding to $Q^2 = 0.20 - 0.52\ (GeV/c)^2$ at the Δ peak. At the low end of this Q^2 range quasi elastic scattering is more probable than Δ excitation and at the high end deep inelastic scattering and low energy tails from the production of high energy resonances start to become dominant [3]. The facilities at the Stanford Linear Accelerator were used with a $1.6\,GeV/c$ spectrometer [30] and an electron detector constructed specifically for this experiment consisting of three multiwire drift chambers (each with four planes of wires) an atmospheric-pressure, isobutane-filled Cerenkov detector, two planes of scintillator hodoscope, and a 35 segment Pb-glass shower counter. The quasi elastic and Δ peaks for ^{12}C appeared at W values of around 0.970 and $1.250\,GeV/c^2$ respectively. The Δ

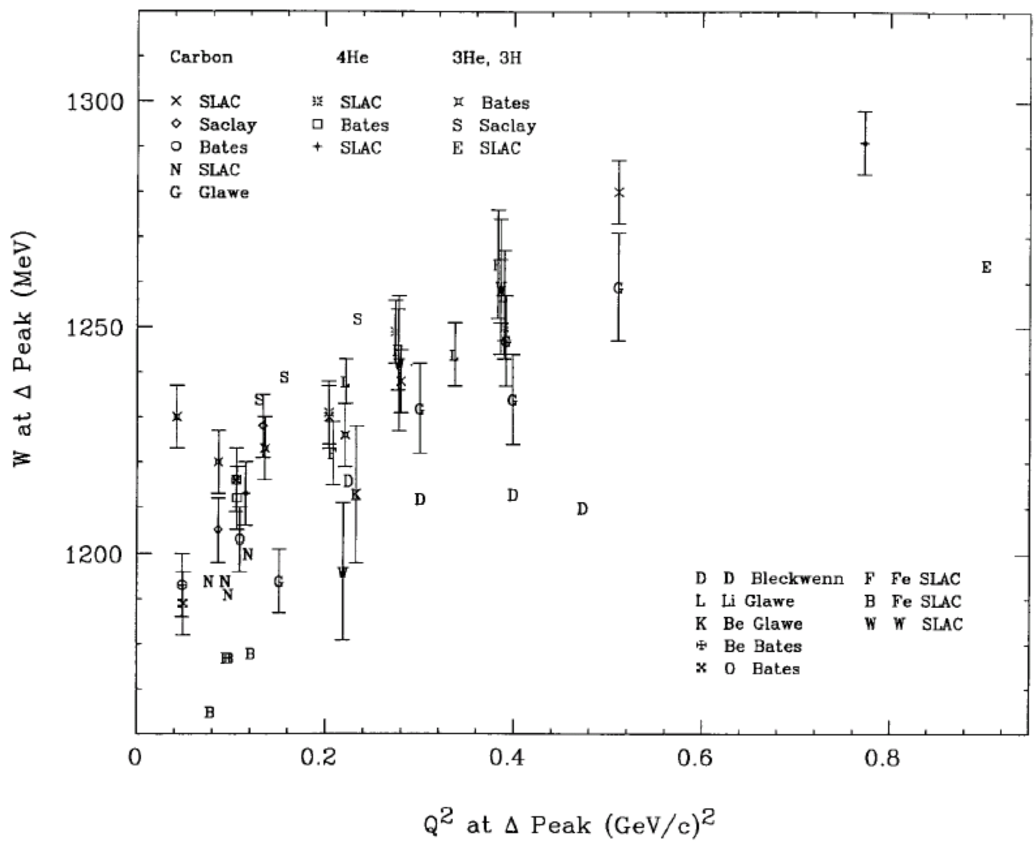

Figure 1.8: Summary of inclusive electron scattering results. The Δ peak is shown to increase with Q^2. Figure taken from [31].

peak was broadened, primarily by Fermi motion, to about $250\,MeV/c^2$ FWHM from the $118-127\,MeV/c^2$ FWHM observed in the H data. The cross sections decreased by a factor of 5 as the momentum transfer increased from 0.20 $(GeV/c)^2$ at the Δ centroid for $0.96\,GeV$ beam energy to 0.52 $(GeV/c)^2$ for $1.5\,GeV$ beam energy. Sealock *et al.* found much less enhancement of the cross sections per nucleon than that reported by O'Connell *et al.* at lower Q^2 [18, 19]: 8% at $Q^2 = 0.2$ $(GeV/c)^2$ decreasing to only 1% at $Q^2 = 0.4$ $(GeV/c)^2$. At all beam energies there was no observed A dependence of the cross section per nucleon in the Δ region. At low Q^2 the centroid of the Δ region peak for excitation in light nuclei was up to $30\,MeV$ lower in energy loss than for excitation from the free nucleon. The apparent Δ centroid was found to occur at higher invariant mass for nuclei than for the nucleon except for the lowest Q^2 tungsten data. A change in the position of the Δ peak with Q^2 first noted by Barreau *et al.* [17] was also indicated in this work.

Results from many of the inclusive measurements discussed above are summarised in figure 1.8 which shows the apparent centroid of the Δ peak for Q^2 in the range $0.05-0.9$ $(GeV/c)^2$. There is a striking Q^2 dependence of the Δ position.

In principle the strength and momentum dependence of the Δ-nucleus potential can be extracted from the Δ peak positions. The Δ peak shifts with Q^2 observed by Sealock *et al.* [3] were described phenomenologically in terms of a momentum dependent Δ-nucleus potential by O' Connell and Sealock [5]. It was found that the depth derived for this potential was greater than that for the nucleon-nucleus potential and similar to that found by Danos and Williams [32] in an effective shell model for the Δ-nucleus system. However, Horikawa, Thies and Lenz [33] found that the Δ nucleus interaction is less attractive than the nucleon-nucleus interaction.

The group at the Laboratory for Nuclear Science, Massachusets Institute of Technology, made a series of measurements on ^{12}C in the dip and Δ regions [34–36] at the MIT-Bates Linear Accelerator using the spectrometers MEPS and OHIPS to detect electrons and protons in the late 1980's [37]. Each spectrometer was equipped with a two-plane vertical drift chamber to measure the particle coordinates (x, y, θ, ϕ) and a scintillator array for trigger definition [36]. The electron spectrometer was also equipped with an aerogel Cerenkov counter for pion rejection. Lourie *et al.* used an incident energy of $0.459\,GeV$ with the electron kinematics held constant at $\omega = 0.2\,GeV$, $|\mathbf{q}| = 0.4\,GeV/c$, and a scattering angle of $60°$. Protons in the kinetic energy range 60 to $200\,MeV$ were detected at $34°$ [34]. Baghaei *et al.* investigated the Δ region with two sets of electron kinematics: (1) beam energy of $0.460\,GeV$ with $\omega = 0.275\,GeV$, $|\mathbf{q}| = 0.401\,GeV/c$, and an electron scattering angle of $60°$, and (2) beam energy of $0.647\,GeV$, $\omega = 0.382\,GeV$, $|\mathbf{q}| = 0.473\,GeV/c$, and scattering angle $39.5°$. In the first case, protons were detected at $-23.6°$ in the kinetic energy range 55 to $275\,MeV$, and in the second they were detected at $-20.8°$ in the kinetic energy range of 62 to $382\,MeV$ [35]. Weinstein *et al.* performed their measurements at momentum transfers $|\mathbf{q}|$ of 0.585, 0.775 and $0.827\,GeV/c$. Both these measurements indicated that scattering from quasi deuterons is a major component of the dip region cross section and that this component extends, although decreasing, under the Δ peak.

There have also been studies of the medium properties of the Δ using pion photoproduction, most recently by Branford *et al.* [38] but also by Liang *et al.* [39] and MacKenzie *et al.* [40]. Although these are not discussed in detail, they show the necessity to understand the medium modifications of the Δ resonance if an understanding of its interaction in the nuclear medium is to be understood.

1.5 Present Measurement

As described above, most electroexcitation measurements in the Δ region used inclusive scattering due to the limitations of the available detector systems. The inclusive measurements give a good overview of the structure of the nucleons and their excitations but it is hard to pick out any particular property of one particle. Contributions from other processes have to be estimated to extract information on the Δ peak position. In the measurements summarised above, it is possible that the Δ peak position is heavily influenced by the Q^2 dependencies of the background contributions. At low Q^2 the two body process has a slope that could shift the centroid of the apparent Δ peak to lower invariant mass [34, 36]. This effect decreases as Q^2 increases. At high Q^2 the sloping non-resonant background could shift the centroid to higher invariant mass [41]. This effect increases as Q^2 increases. Without eliminating these background contributions, any interpretation of the Δ position is limited by uncertainties in models of the background. This emphasises the need for exclusive measurements where the Δ production cross section can be isolated using the reaction kinematics. This is now possible because high duty factor accelerators and large acceptance detectors are available where multi particle final states can be measured.

In April 1999 a measurement was performed at the Jefferson Laboratory (formerly CEBAF - Continuous Electron Beam Accelerator Facility) using the CLAS (CEBAF Large Acceptance Spectrometer) detector system in Virginia, USA [42] to investigate the properties of the Δ resonance mentioned above. The measurement used ^3He and ^{12}C targets. The combination of electron beam energy and magnetic field was chosen so that the kinematics of the data overlapped the data taken in [3] (see sections 2.1 and 2.2.1 for more details). The CLAS detector has $\sim 4\pi$ acceptance and allows the detection of complete final states through a complicated array of detectors. The detector system is described in more detail in chapter 2. As the experimental trigger for detecting an event only required the detection of an electron, inclusive, semi inclusive and exclusive measurements could all be performed on the data. This allowed a comparison with, and extension of, the inclusive results published in [3].

The first results from ^3He have been reported in a recent thesis [43]. The data presented here represents the first exclusive measurement of the Δ mass in nuclei as a function of Q^2 for ^{12}C.

Chapter 2

Experimental Setup

The e2a experiment ran from April 15 to May 27, 1999. The data recorded in this period covered a range of beam and detector settings. The setup analysed for the present measurement used an electron beam energy of $1.162\,GeV$ and magnetic field strength of $0.5\,T$ (corresponding to a torus current of $1500\,A$). These data were taken between the 14th and 18th of May 1999.

2.1 The Thomas Jefferson National Accelerator Facility

The studies reported here were carried out at the Thomas Jefferson National Accelerator Facility (Jefferson Laboratory), located in Newport News, Virginia, USA. The Jefferson Laboratory contains the Continuous Electron Beam Accelerator Facility (CEBAF) supplying three experimental halls with multi-GeV electron beams. A schematic diagram of the accelerator is shown in figure 2.1. The electrons are produced at the injector. A laser focused on a gallium arsenide cathode produces photo-electrons which are accelerated and sent into the first linear accelerator (LINAC) with an energy of $62\,MeV$. The accelerator consists of two parallel LINACs in a "race track" configuration which boost the beam energy by $1.1\,GeV$ in each complete circuit. The electrons can complete, at most, five circuits resulting in a maximum energy of around $5.5\,GeV$[1]. Both LINACs consist of twenty cryomodules, each containing five super-conducting niobium radio frequency (RF) cavities that accelerate the electrons [44]. Liquid Helium keeps the accelerating cavities superconducting at a temperature of $2\,K$. The LINAC energies are set identical and the RF cavities are phased to provide maximum acceleration. Subsequent passes through the accelerator are phased to maximum energy gain by adjusting the length of travel in the preceding arc.

[1] These values were recorded at the time of data taking. Since then, the energies have increased.

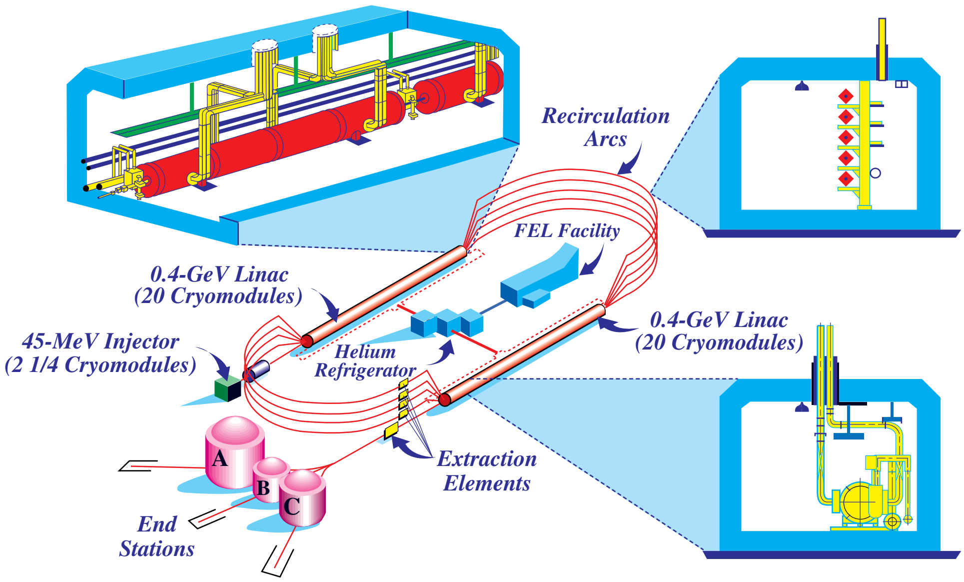

Figure 2.1: Schematic diagram of the Jefferson Laboratory facility. The LINACs were designed as $0.4\,GeV$ but the energy actually reached about $0.55\,GeV$ at the time of this experiment and the injector LINAC provided $62\,MeV$ electrons. The three blow up boxes show (clockwise from upper left hand side): one of the LINAC cryomodules; a cross section of the tunnel with the five recirculating arcs; a cross section of a cryomodule.

The beam can be extracted from the accelerator at the end of any of the five passes and sent to each of the three experimental halls (A, B and C). The energy spread of the beam is $\Delta E/E < 10^{-4}$. The $1.497\,GHz$ RF wave in the accelerating cavities allows simultaneous beams to be delivered to each hall at a frequency of $499\,MHz$. This means that each hall receives one of every three RF pulses i.e. the beam arrives in bunches or "buckets" $2\,ns$ apart. The beam buckets can be loaded with different electron densities which allow the three experimental halls to operate with different beam currents.

The experimental halls are equipped with detectors for different experimental programmes. Hall A houses two high resolution spectrometers which are instrumented for electron and hadron detection. Hall C contains two medium resolution magnetic spectrometers with different momentum ranges. Hall B houses the CEBAF Large Acceptance Spectrometer (CLAS) which is used for exclusive multi-particle final state measurements. The CLAS detector was used for the measurement being reported and is described in more detail below.

2.2 CEBAF Large Acceptance Spectrometer (CLAS)

The present measurement took place in Experimental Hall B of the Jefferson Laboratory, which contains the CEBAF Large Acceptance Spectrometer (CLAS). This near 4π acceptance detector was designed to study multi-particle final state reactions, induced by electrons and tagged photons at luminosities $\sim 10^{34} cm^{-2}s^{-1}$. CLAS is constructed around six iron-free super-conducting coils that segment the detector into six independent magnetic spectrometers, or "sectors", having six-fold symmetry around the beam axis. The coils generate a toroidal magnetic field about the beam axis that bends charged particles towards or away from it while their azimuthal angle remains essentially unchanged. The particle detection system consists of drift chambers, to determine charged particle trajectories, Cherenkov detectors for scattered electron identification, scintillation counters for flight-time measurements and electromagnetic calorimeters to detect scattered electrons and high energy neutral particles. Each of these sub-detector systems, as well as target, magnetic field and trigger settings, is described below. Figure 2.2 shows a schematic diagram of the CLAS setup.

2.2.1 Magnetic Fields

There are two magnetic fields that can be applied during an experimental run using CLAS - the mini torus and the main torus. These have different purposes and the properties and both are described in the this section.

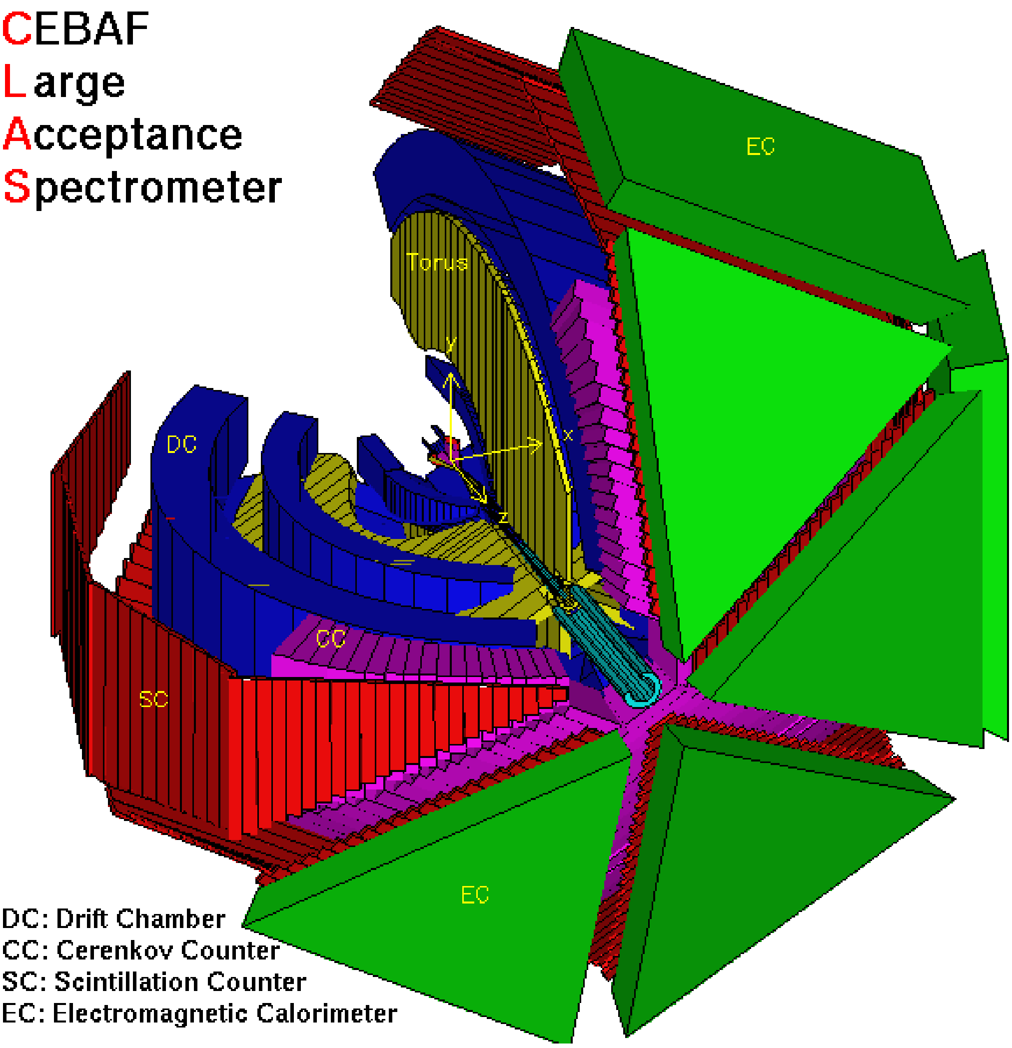

Figure 2.2: The CLAS detector. A section has been cut out to view the internal components of the detector.

The main torus in CLAS is used to measure the momentum of charged particles. Six toroidal iron-free superconducting coils are arranged around the beam axis, located between the instrumented sectors in the region 2 area of the CLAS tracking system (see section 2.2.2), to produce a circular field with a maximum intensity of $2\,T$. The magnetic field has its maximum value in the forward direction, in order to bend the higher energy particles, and drops by a factor of five at large angles. The centre region of the spectrometer is field-free to allow operation with polarised targets.

The mini torus, a small toroidal coil inserted into the cavity of the large superconducting magnet, generates a magnetic field to sweep away low energy (background) electrons. The field created by this shield is small compared with the field of the main coils, but provides excellent elimination of the Møller electron background: nearly a factor of 100 background rejection in the region enclosed by the first drift chambers layer (DC Region 1 in figure 2.3).

The tracking system is used in conjunction with the magnetic field to build tracks of charged particles emerging from the target. The momentum of charged particles is calculated given the time of flight from the target to the scintillators (see section 2.2.4) and the curvature of the track. These tracks are projected back to the target to find the point of interaction or event vertex.

The field strength used during the experiment was $0.5\,T$ corresponding to a torus current of $1500\,A$. This enabled the detection of the low Q^2 events, at which the biggest variation in Δ mass had previously been reported [3].

2.2.2 Drift Chambers

The trajectories and momenta of charged particles are measured in CLAS using the Drift Chambers [45] which are a collection of 18 separate chambers arranged in three radial locations from the target, in each of the six sectors (see figures 2.3 and 2.2). The radial locations are referred to as "regions". The region 1 (R1) chambers are closest to the target, in an area of low magnetic field. The region 2 (R2) chambers are larger than the region 1 chambers and reside between the coils of the magnet, in the area of highest magnetic field. The region 3 chambers (R3) are the largest and are located radially outward of the R2 chambers, in an area of low magnetic field (see figure 2.3).

The wires inside the chambers are arranged in "layers" of concentric circles around the target. For pattern recognition and tracking redundancy, the wire layers in each chamber are grouped into two "superlayers". The wires in the "axial" superlayer are parallel to the magnetic field and the "stereo" superlayer contains wires at a 6° stereo angle around the radius of each layer to provide azimuthal information. Each superlayer consists of six layers of drift cells as shown in figure 2.4. The wires are arranged in a hexagonal pattern, with each sense wire surrounded by six shared field wires. This

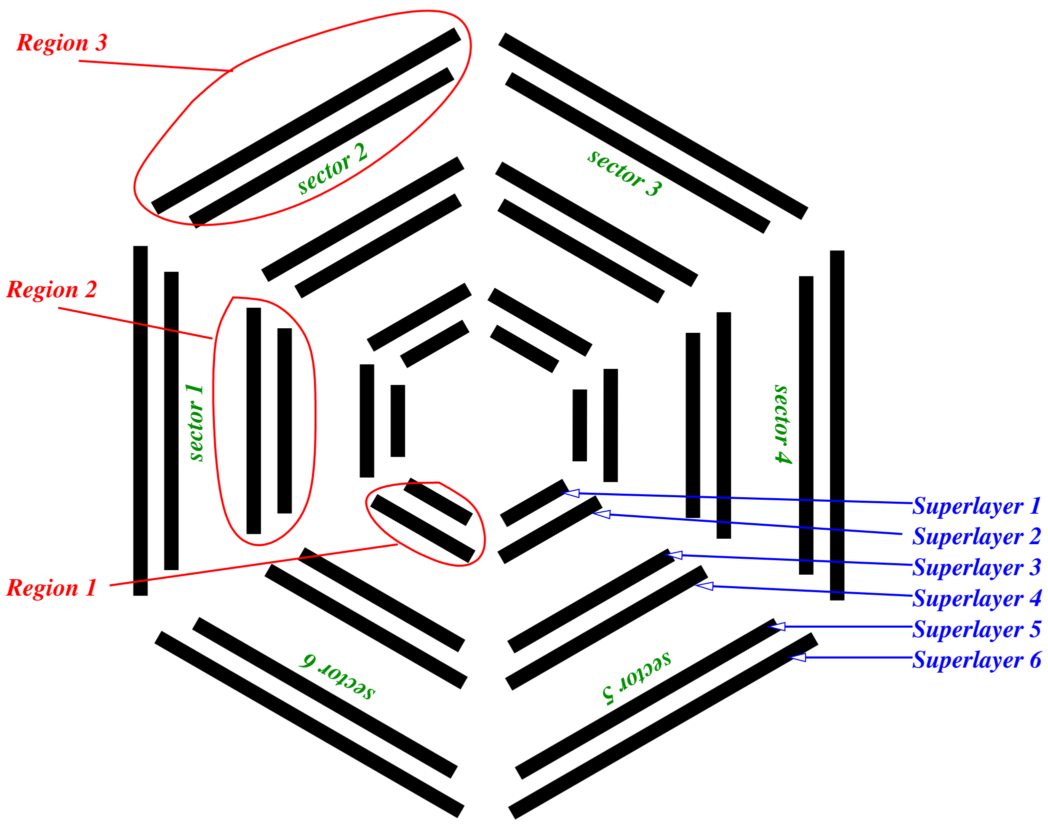

Figure 2.3: Diagram of the Drift Chambers in CLAS viewed from the direction of the beam. The regions and superlayers are shown.

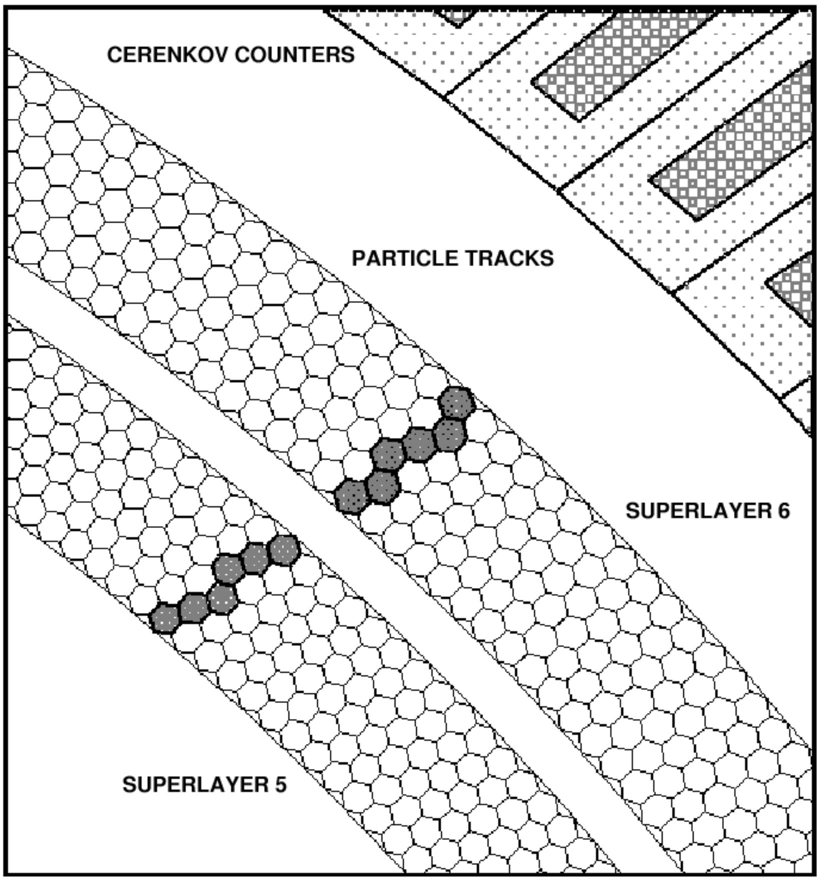

Figure 2.4: A schematic of part of a drift chamber showing two superlayers. Each hexagon represents a drift cell with sense wires at the centre and field wires at the vertices. The shaded cells represent a track from a charged particle crossing the drift chamber.

hexagonal configuration was chosen as a good approximation of the ideal circular cell in which the drift/time relation is independent of the entrance angle. Each superlayer is surrounded by a row of guard wires to minimise edge effects.

The ionising gas used in the chambers is a 90% argon, 10% carbon dioxide mixture. When a charged particle passes through the chambers, it will cause ionisation in the gas. The electric field created by the wires in the chambers causes the electrons and the ions to drift in opposite directions where they are collected by the anode and cathode wires. When the electrons drift close to the anode wires where the electric field is very strong, they can collide with the gas atoms causing secondary ionisation and creating an amplification effect. Argon provides a gain of 10^4 while CO_2 can prevent uncontrolled avalanches from occurring. This gas mixture gives a drift velocity of up to $0.04\,m/\mu s$ and an operating voltage plateau of several hundred volts. The average layer efficiency is greater than 98 %.

The CLAS detector tracks charged particles emerging from the target with momenta greater than $200 MeV/c$ over a polar angle range from 8° to 142°, while covering 80% of the azimuthal range. The resolution is about $400\,\mu m$ for the trajectory positions, $\leq 1\,\%$ for the reconstructed momentum and a few $mrad$ for the angles.

2.2.3 Cherenkov Detector

The Cherenkov detectors [46] are used primarily for two purposes in CLAS: quick identification of electrons in the trigger and separation of electrons and pions.

When a particle travels through a medium faster than the speed of light in that medium, the particle produces Cherenkov light. The CLAS Cherenkov Counters have six identical counters, one for each sector, and each collects the Cherenkov light using a complex system of mirrors. The light collection system of each sector is split into 18 regions of θ from 8° to 45° and the Cherenkov light is focused in the ϕ direction. Each θ region is divided into two “modules” about the symmetry plane bisecting each sector. This results in a total of 216 light collection modules (36 per sector) and is shown in figure 2.5.

The optics of each θ module was designed to focus the light onto the photo-multiplier tube associated with that module. Figure 2.6 shows the focusing of the Cherenkov light from a passing electron. Each module consists of two focusing mirrors (one elliptical and one hyperbolic), a “Winston” light collection cone and a cylindrical mirror at the base of the cone.

The gas used in the detector is perfluorobutane (C_4F_{10}). This was chosen for its high refractive index (1.00153) and excellent light transmission properties. The resulting energy threshold for producing Cherenkov light is $9.24\,MeV$ for electrons and $2.51\,GeV$ for pions [47].

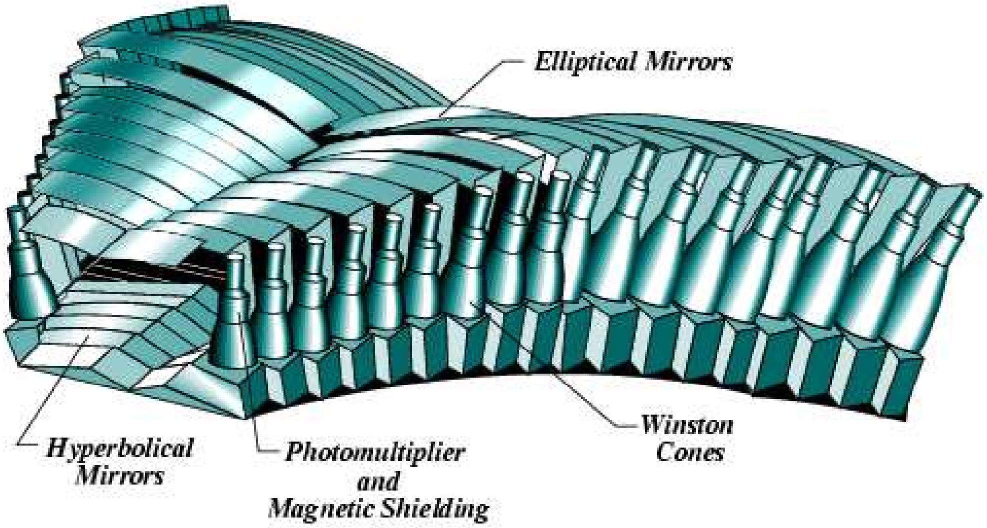

Figure 2.5: A CLAS Cherenkov detector.

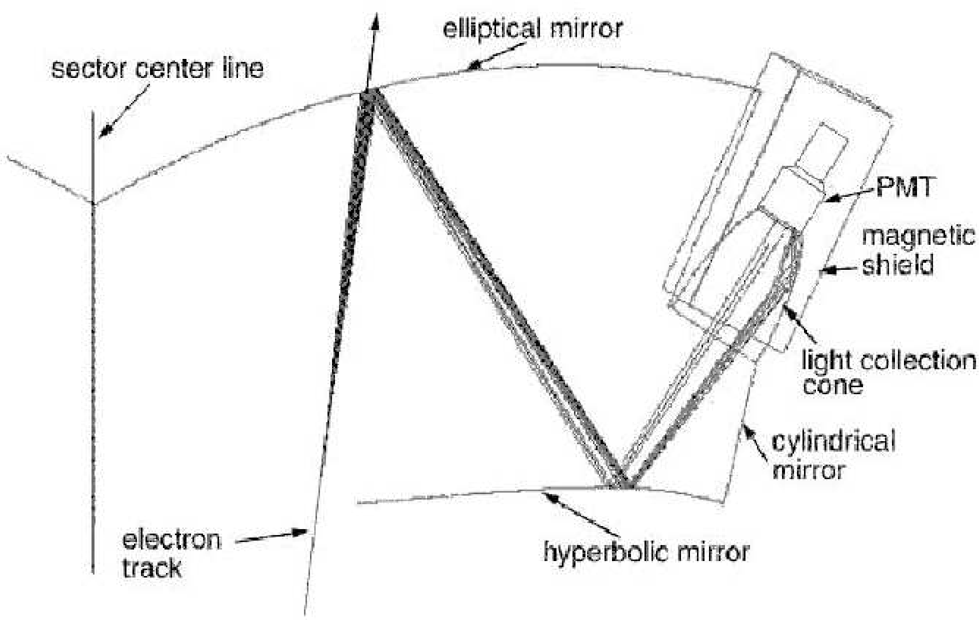

Figure 2.6: Simplified ray tracking scheme in a Cherenkov detector module. Cherenkov light from electrons is reflected twice from the mirrors into the Winston cone which focuses the light into the photomultiplier (PMT).

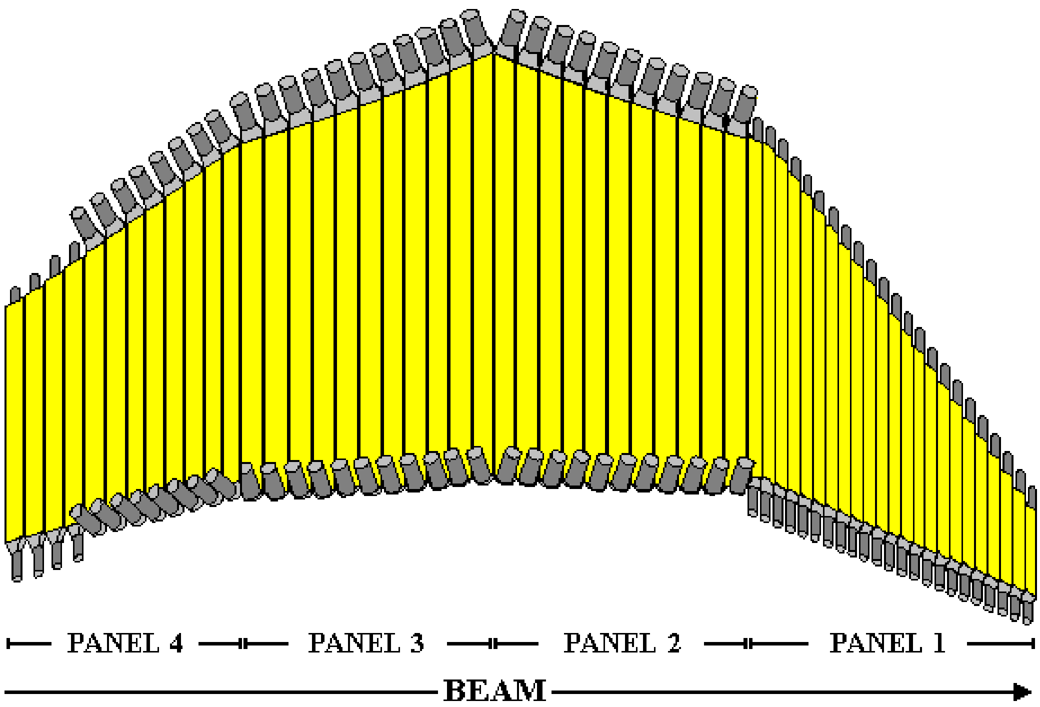

Figure 2.7: Time of Flight bars: four panels of scintillators equip each sector.

2.2.4 Time of Flight Detector

The time of flight system [48] is used for particle identification in CLAS. The scintillators form a "shell" around the target and are located between the Cherenkov detectors and Electromagnetic Calorimeters (see figure 2.2) to reduce multiple scattering and the production of knockout electrons. The counters cover a polar angle range from 8° to 142° and all the azimuth between the coils. Each scintillator is rectangular with two photo-multiplier tubes, one at each end. The counters are mounted in four panels in each of the six sectors. Scintillators 1-23 are mounted in panel 1 and are referred to as the "forward angle" counters. They correspond to scattering angles less than 45°. Panels 2, 3 and 4 are called the "large angle" counters. Figures 2.7 and 2.2 show the setup of the panels in CLAS. Each scintillator is placed perpendicular to the direction of incident particles such that the width of the counter subtends about 2° of the scattering angle. The counters are parallel to the axial drift chamber wires and span the azimuthal angular range of each sector.

Each sector has 57 scintillators, each with a photo-multiplier tube at both ends. The last 18 of these are paired into 9 logical counters. This grouping results in the system having a total of 48 logical counters per sector. The lengths of the counters vary from 445 *cm* in the centre region to 32 *cm* at the forward and backward edges. The first 23 paddles (right hand side in figure 2.7) and the last four paddles are 15 *cm* wide while the rest of them are 22 *cm* wide. The average time resolution for electrons is 163 ps [48].

2.2.5 Electromagnetic Calorimeter

The Electromagnetic Calorimeter [49] is used to detect and trigger on scattered electrons. It can also detect neutral particles with an efficiency up to 60%.

The Calorimeter is a sampling calorimeter i.e. the energy deposited in the scintillators by a particle is less than the energy of the particle. It consists of alternating layers of scintillator strips and lead sheets with a total thickness of 16 radiation lengths. The thickness ratio of lead to scintillator is 0.21, requiring 39 cm of scintillator and 8.4 cm of lead per module. With this ratio, around one third of the shower energy is deposited in the scintillators.

The lead-scintillator sandwich covers a polar angle range from 8° to 45° with azimuthal coverage matched to that of the drift chambers (see figure 2.2). The detector forms an equilateral triangle in each of the six sectors, each composed of 39 layers of BC412 scintillator 10 mm thick with a 2.2 mm thick layer of lead in between. Each scintillator layer is made of 36 strips parallel to one side of the triangle, with the orientation of the strips rotated by 120° in each successive layer. Thus there are three orientations or "views" (labelled U, V and W), each containing 13 layers which provide stereo information on the location of energy deposition. The three views provide transverse shower information. This is shown in figure 2.8. Each view is further sub-divided into an inner (5 layers) and outer (8 layers) stack to provide longitudinal sampling of the shower, allowing improved hadron identification. Figure 2.9 shows the 13 layers and two stacks.

The Calorimeter uses a "projective" geometry, in which the area of each successive layer increases. This minimises leakage at the edges of the active volume. The detector thus forms a truncated triangular pyramid with a projected vertex at the CLAS target point 5m away.

The Electromagnetic Calorimeter's overall position resolution is about 2.3 cm. The energy resolution is

$$\frac{\Delta E}{E} = 0.003 + \frac{0.093}{\sqrt{E\,(GeV)}} \tag{2.1}$$

The time resolution for electrons is about 200 ps, while that for neutral particles is about 600 ps [49].

2.3 Event Trigger

The trigger is used to tell the Data Acquisition System when to read out the detector state. Firstly, signals from the Electromagnetic Calorimeter and Cherenkov detectors

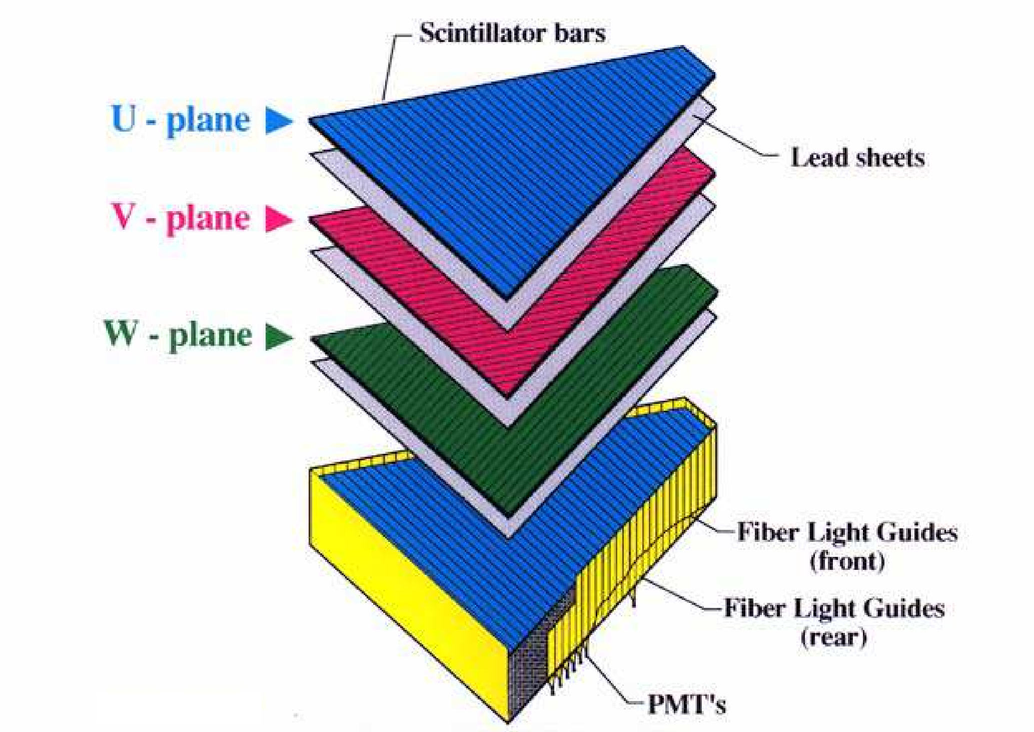

Figure 2.8: Exploded view of one of the six CLAS Electromagnetic Calorimeter modules.

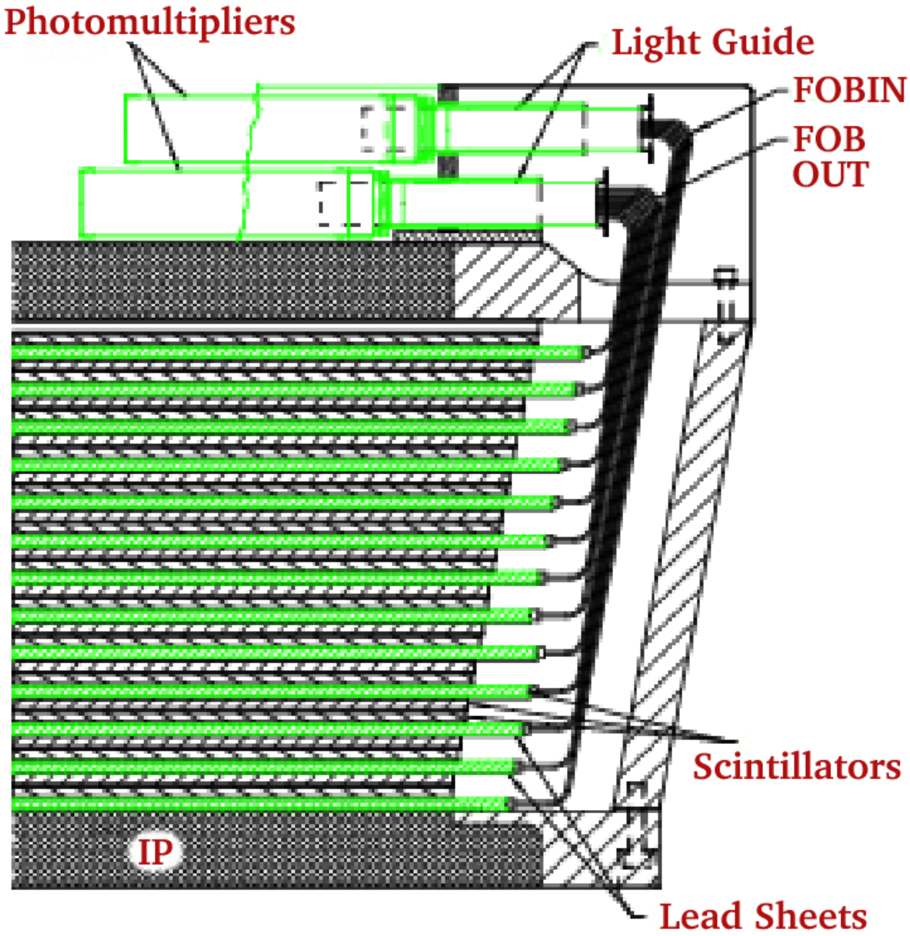

Figure 2.9: Cross section of the Electromagnetic Calorimeter. PMT - photomultiplier; LG - light guide; FOBIN - inner fibre optic bundle; FOBOUT - outer fibre optic bundle; SC - scintillators; PB - lead; IP - inner plate.

Detector	Threshold $[mV]$	Threshold
Electromagnetic Calorimeter	100	$\sim 0.250\,GeV$
Cherenkov	20	<1 photo-electron

Table 2.1: Electromagnetic Calorimeter and Cherenkov detector thresholds.

are fed to the pre-trigger discriminators. They store threshold values for both detectors which can be programmed for different experimental conditions. The threshold values used are listed in table 2.1. The values of threshold used in an experiment depends on the beam energy and torus current combination. These particular values were chosen so that as large a range of scattered electrons could be detected. If the signals are above threshold, the event is passed to the Level 1 trigger, which requires a hit in the same sector for both the Cherenkov detector and Electromagnetic Calorimeter. This signaled a potential electron and initiated a readout of the event by the Data Acquisition System.

2.4 Data Acquisition and On-line Monitoring Systems

The setup of the electronics in the Data Acquisition System is given in figure 2.10. When a trigger is generated the signal is passed to the Trigger Supervisor which instructs the FASTBUS and VME controllers to read out, digitise and transmit the data signals through Read Out Control memory to the network and Event Builder. From the Event Builder the data pass to the Event Recorder which stores the data on a local disk awaiting transfer to the tape silo of Jefferson Laboratory.

After the event has passed the Event Builder, as well as being passed to the Event Recorder, it was passed to monitoring software (with a frequency of $20\,Hz$) that was used continuously to monitor the detector status, and beam and data quality during data taking. The monitoring software consisted mainly of detector occupancy plots but an event viewer, CLAS Event Display (CED), was also used to show the detector hit patterns in the various detector subsystems. The most important run characteristics, such as total number of triggers, integrated beam charge, averaged live time of the Data Acquisition System and magnet settings, were stored in the CLAS on-line data base.

During this experiment the beam luminosity was of the order $10^{34}\,cm^{-2}s^{-1}$ and the Data Acquisition System limited the data recording frequency to around $2\,kHz$ with a live time of $\sim 95\%$.

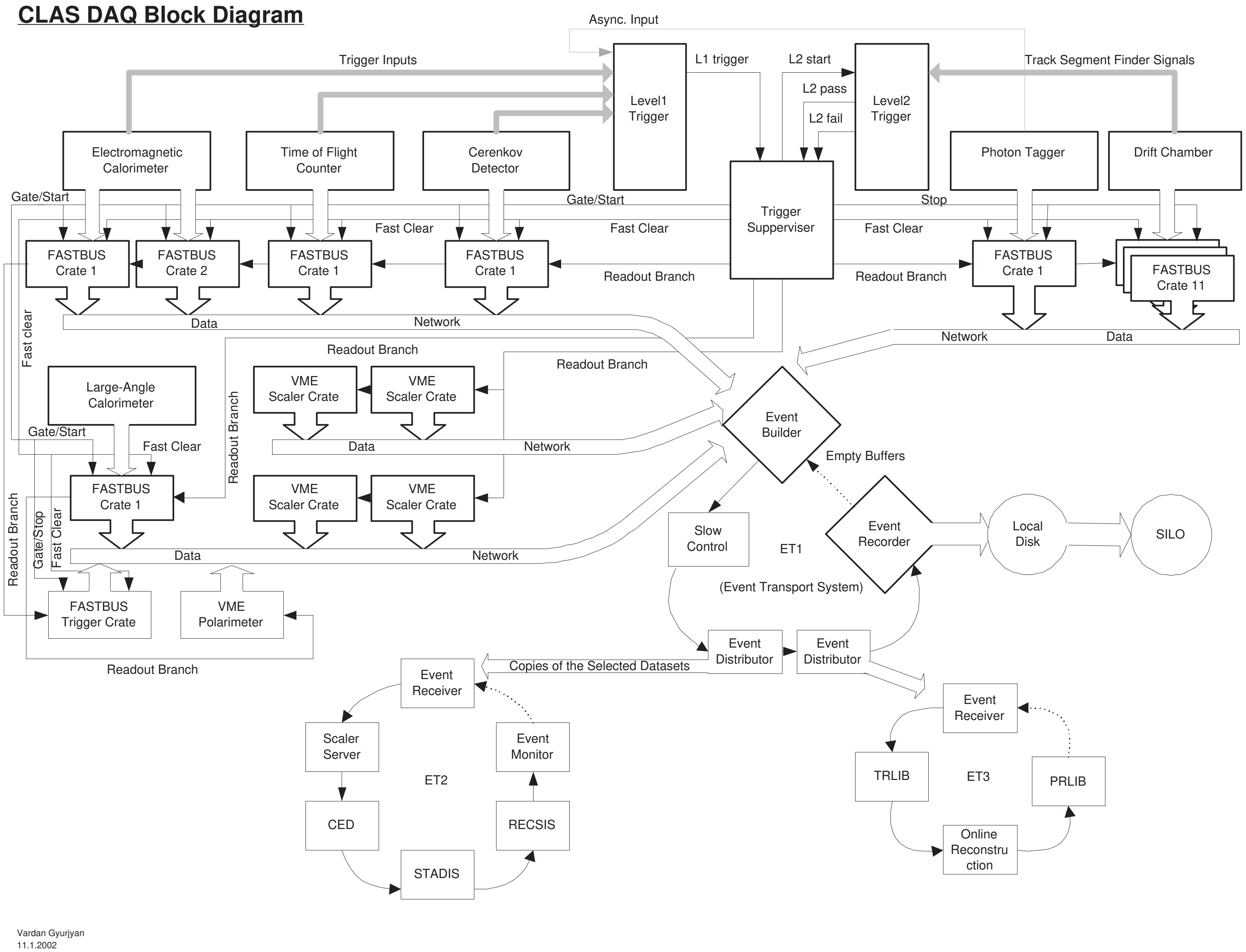

Figure 2.10: Block diagram of the data acquisition system in CLAS.

Height $[cm]$	2.5 ± 0.05
Width $[cm]$	2.5 ± 0.05
Thickness $[cm]$	0.1 ± 0.002
Density $[g/cm^3]$	1.786 ± 0.036
Position of centre $[cm]$	$(0, 0, 5.1)$

Table 2.2: Solid target specifications.

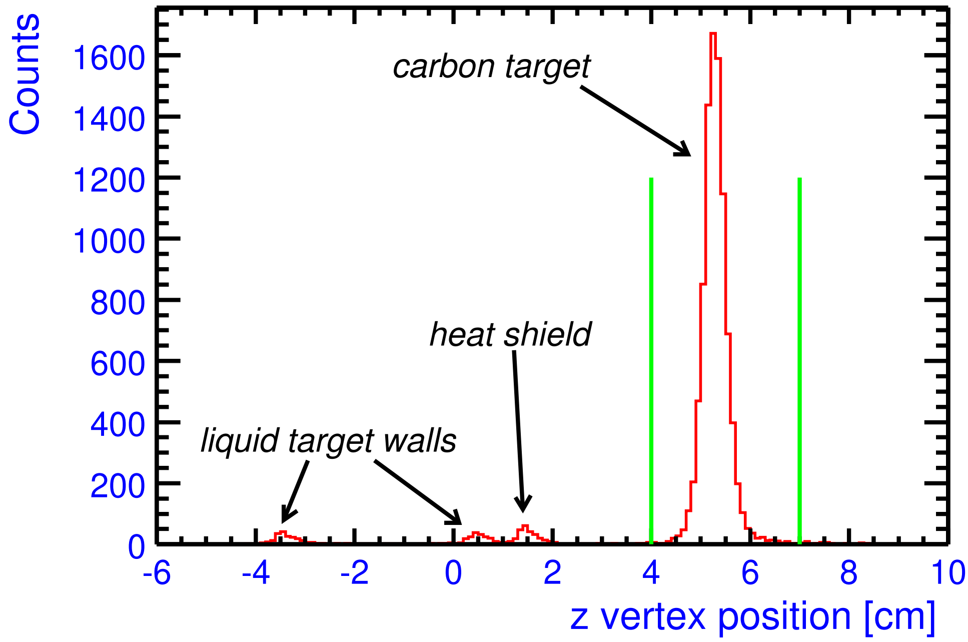

Figure 2.11: Example distribution of the z component of the event vertex (z is defined as the beam direction). The green vertical lines show the range accepted for analysis.

2.5 Carbon Target

A solid carbon target was used in this experiment. The specifications of the target are shown in table 2.2. A histogram of event z vertex (along the direction of the beam) is shown in figure 2.11 which clearly demonstrates that some events originated from places other than the carbon target. These events were produced in the walls of the empty liquid target and the heat shield that forms part of the liquid target. Only events lying in the range $4.0 \leq z \leq 7.0\,cm$ were accepted for analysis (shown by the green vertical lines in figure 2.11).

Chapter 3

Detector Calibration

When the experiment was completed the data existed in raw form only. The raw data consists of digitised charge and time measurements recorded by the detector electronics during the experiment. For this data to be useful, from an analysis point of view, it had to be converted into physics quantities such as momentum and particle type. The conversion process is called “cooking”.

The cooking requires calibration constants in order to complete this conversion (see section 3.2). A description of the calibration of CLAS, focused on the Electromagnetic Calorimeter, is given in section 3.2.

3.1 Cooking

The cooking process uses the calibration constants for the detector channels to turn the detector signals into particle information. This procedure is different for the different detectors so as an example consider the Electromagnetic Calorimeter.

When a particle enters the detector scintillation light is produced. The detector converts the scintillation light to charge and the data acquisition stores the value of charge in each layer for a given view (see section 2.2.5). The cooking software converts the value of charge collected into energy deposited in the layer of strips.

If the particle being studied was a trigger particle, further tests were carried out. The energy deposited in each view was combined to reconstruct the electromagnetic shower that was created. The properties of this shower were compared to the characteristic electron shower to verify the detection of an electron.

Information from each detector is combined in this process to accept or reject candidate tracks, particles and events.

3.2 Calibration

The energy deposited in the detectors was read out by analogue to digital convertors (ADCs) which output in channel numbers. Therefore a translation from ADC channel number to energy was required. Time signals from the detector were read out by time to digital convertors (TDCs) which also output in channel numbers requiring a conversion to time. These translations are the calibrations. The calibration of CLAS is an iterative procedure, based on the fact that the response of the detector elements drift over time. The whole CLAS detector needs to be calibrated for each run period. Therefore the detector was already calibrated up to the start of the experiment.

The calibration process is defined by the following steps:

1. Cook a small amount of the data using the calibrations from the previous run period (pass 0 cooking);

2. Calibrate. See below for a description of the calibration of each detector;

3. Cook all the data using the new calibration constants (pass 1 cooking).

Since CLAS is a combination of different detectors, the calibration procedure for each is different. The cooking and calibration sequences were repeated several times since the calibration of some detector subsystems required the previous calibration of others. All together this is a huge job and so was shared amongst the collaboration members. My work was focused on the energy calibration of the Electromagnetic Calorimeter (EC) and a description of this process is given below. An overview of the procedure for the Time of Flight (TOF) calibration [50] and the Drift Chambers (DC) [51] is also given while for the calibration of the Cherenkov counters, the reader is referred to [52, 53].

3.2.1 Electromagnetic Calorimeter

The design and geometry of the Electromagnetic Calorimeter is described in section 2.2.5. The energy calibration centres around the interaction of minimum ionising particles with the lead and scintillators of the detector. When a minimum ionising particle passes through the detector, only one scintillator, or "strip", in each view is involved in the detection. A comparison of a minimum ionising interaction with that of a showering interaction shown in figure 3.1. These events are used since they deposit a fixed amount of energy in the detector: $10\,MeV$ for the inner layer and $16\,MeV$ for the outer layer.

The detector had been calibrated for the previous run period so the first step in calibrating for the e2a run period was to check the existing calibration. Using the pass

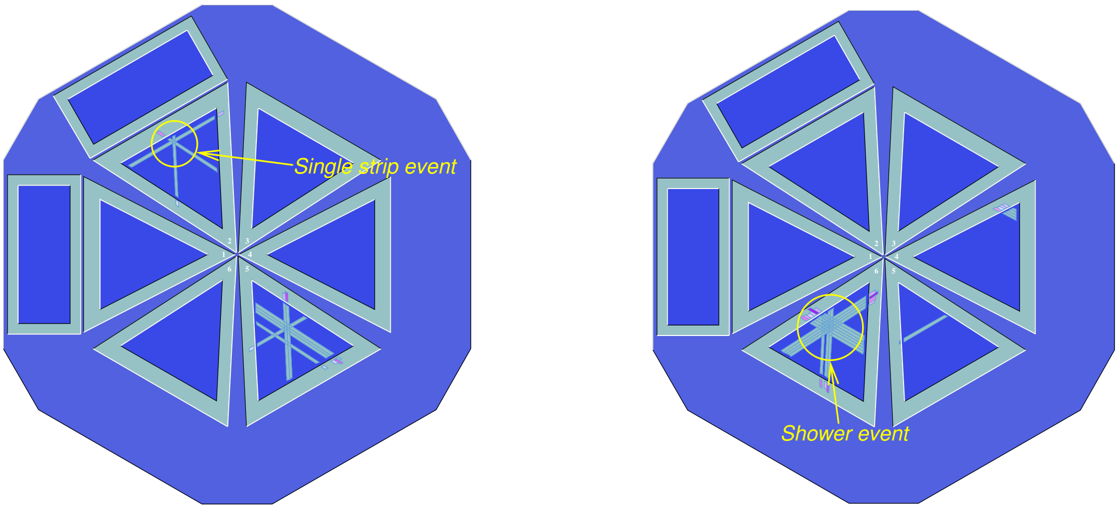

(a) Minimum ionising interaction: Only one strip in each view is involved in the detection.

(b) Showering interaction: Multiple strips in each view are involved.

Figure 3.1: Comparison of single strip to shower events in the Electromagnetic Calorimeter (viewed looking along the beam line in the direction of travel).

0 data, the energy deposited in each strip was plotted for minimum ionising events. A Gaussian was fitted to each of these plots in order to obtain the minimum ionising peak position. These were then plotted as a function of strip number and are shown for each of the three views and two layers in figure 3.2. The obtained peak positions showed good agreement with the expected values (the dashed lines in figure 3.2) particularly for the inner layer. Therefore, the calibration constants that were used for pass 0 cooking were deemed sufficient for the e2a run period.

The EC was used in the measurement presented here to detect the scattered electrons but it is also used to detect neutral particles (photons and neutrons). As a result, the EC time measurement is crucial for measurements that require neutral particle identification because neutrons can only be distinguished from photons by means of their velocities.

The electron time as measured by the TOF is used to calibrate the EC time measurements. An electron is identified by its straight track between the scintillation counters (SC) and the EC resulting from there being no magnetic field between these two sets of detectors. Therefore, if it is assumed that the SC time calibration is correct, the time measured by the EC can be predicted as:

$$t_{ec} = t_{sc} + \frac{d_{ecsc} \cos \alpha}{v} \tag{3.1}$$

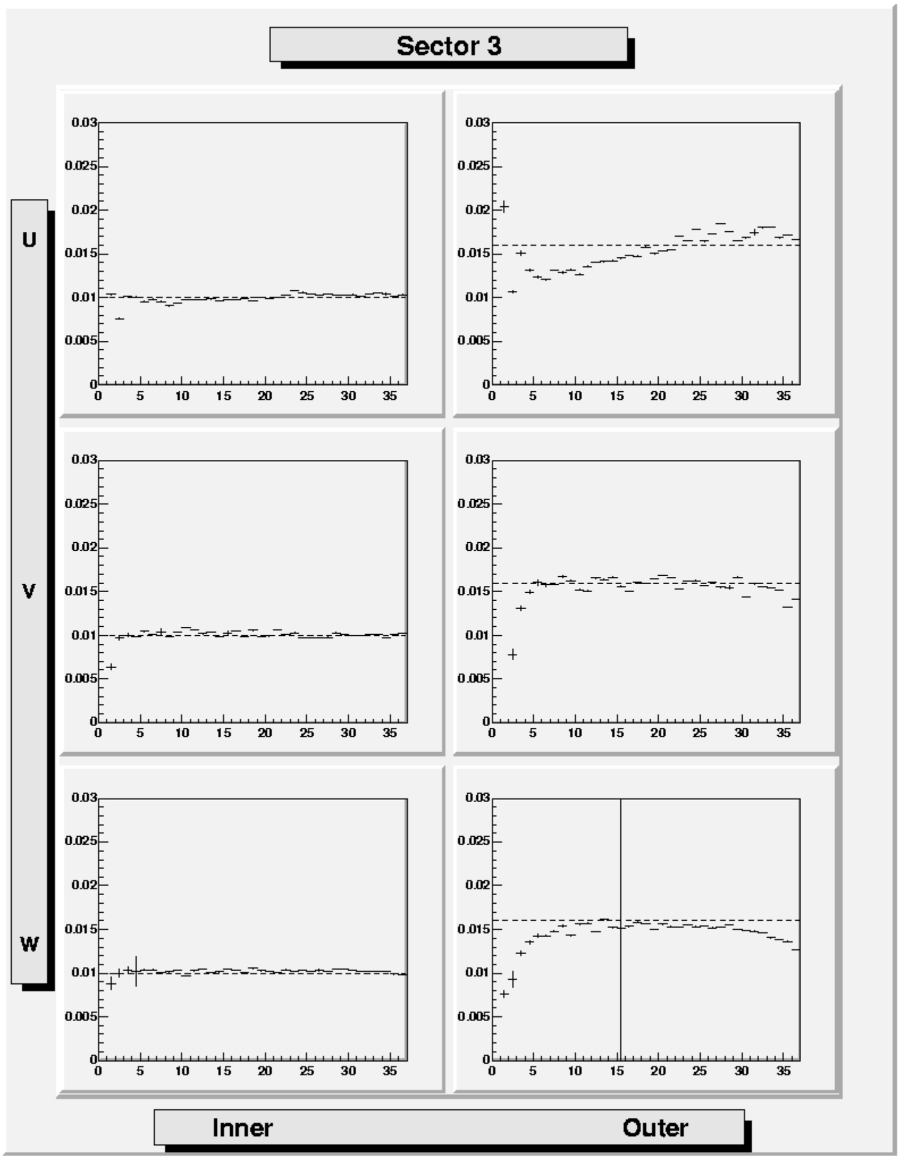

Figure 3.2: Minimum ionising peak position versus strip number for each of the three views (u, v, w) and two layers (inner and outer).

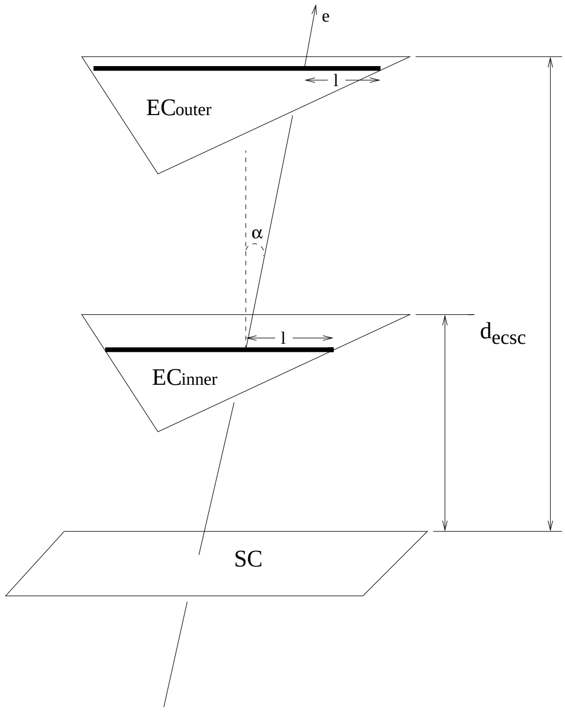

Figure 3.3: EC time extrapolation from SC time. d_{ecsc} is the distance between the EC layer (inner or outer) and the SC layer, α is the impact angle of the electron to the EC plane and l is the length from the hit point to readout edge along the scintillation bar. Only the scintillation bar with the largest ADC value in one view for each EC layer is shown.

where t_{sc} is the time from the SC, d_{ecsc} is the distance between the EC and SC layers, v is the electron velocity, and α is the impact angle to the EC plane (see figure 3.3).

The value t_{ec} is assigned to the EC scintillation bar with the largest ADC for each of the three views and the time dependence is fitted with the function

$$t_{ec} = p_0 + p_1 tdc + \frac{p_2}{\sqrt{adc}} + p_3 t^2 + p_4 t^3 - \frac{1}{v_{eff}} \tag{3.2}$$

where p_i are five fit parameters, tdc and adc are the TDC and ADC values respectively, l is the length from the hit point to the EC readout edge and v_{eff} is the speed of light in the scintillator material. The first two terms are the simple linear TDC response, the third term is the time-walk correction, the fourth and fifth terms are small corrections for the fact that signals arrive at the readout edge at slightly different times for scintillation bars connected to the same PMT, and the last term is inserted to compensate for the time taken for the scintillation light to travel from the hit position to the readout edge.

The best fit constants were saved in the calibration database. The difference between the reconstructed EC time and the TOF value defines the time resolution for electrons and this was found to be $200\,ps$. A more detailed discussion of the EC time calibration is found in [47].

3.2.2 Drift Chambers

The design and geometry of the Drift Chambers (DC) is described in section 2.2.2. The DC is used to measure the momentum of charged particles. This is determined by the particle's trajectory in the DC together with information about the magnetic field.

When a charged particle passes through the DC, ideally each of the 34 layers record a hit but due to inefficiencies, or holes in the chamber, it has been found that there are actually an average of only 30 hits per track [47, 50]. Each hit detected in the chambers is used to determine the particle's track using a least squares fit, where a minimisation of the sum of the squares of the closest distance from each hit wire to the track candidate is performed.

The drift chambers are calibrated by parameterising the drift velocity function for each superlayer in each sector [51, 54]. The drift velocity function is the relationship between the closest distance from the track to the sense wire and the time it takes the ions created by the particle to drift from the track to the same sense wire. The TDCs attached to each wire measured the drift time. The initial drift velocity function was parameterised using a trial function based on the calibration of earlier data. This was used to reconstruct the particle tracks using the least square fit method. The reconstructed tracks were then used to geometrically calculate the closest distances which were then fitted against the drift time to improve the trial function. The improved function was used to reconstruct the tracks again, and so on until after several iterations, the drift velocity function converged to the best parameterisation. This process resulted in a drift chamber resolution of $0.4\,mm$.

A more detailed discussion of the DC calibration can be found in [51, 54].

3.2.3 Time of Flight Detector

The system of Scintillation Counters (SC) is used to measure the Time of Flight (TOF) of particles and their design and geometry are discussed in section 2.2.4. The SC system is essential for identifying charged particles since their masses are obtained by combining the results of the TOF and momentum measurements. Also, a precise TOF measurement is a prerequisite for some other calibrations such as the DC and the EC time calibrations already described above. The calibration of the TOF systems involves not only the time measurements but also the energy deposited in the SC and therefore consists of several steps. These are: calibration of the individual TDC channels; left-right PMT alignment and/or energy loss; attenuation length calibrations; effective velocity calibration; then counter-to-counter delay adjustment and, when this is done, an overall RF (accelerator Radio Frequency) offset calibration.

TDC Calibration

The channel-to-time calibrations of all the CLAS TDCs, except those of the DC, were performed using a special pulser run for which the responses of each TDC for various delays between START and STOP were analysed. A quadratic equation was used to convert the TDC channel number, T, to actual time $t(ns)$:

$$t = c_0 + c_1 T + c_2 T^2 \tag{3.3}$$

The c_0 parameter was not relevant since a left-right calibration was done later on.

Time-Walk Correction

Time-walk is an instrumental shift in the time measured using a leading-edge discriminator that is due to different time-rise in the analogue pulse for different pulse heights. The time-walk correction was implemented in the software using the function

$$t_w = t - f_w\left(\frac{A_P}{\tau}\right) + f_w\left(\frac{600}{\tau}\right) \tag{3.4}$$

where A_P is the pedestal-corrected ADC channel number, τ is the channel corresponding to the leading-edge discriminator threshold of $20\,mV$ ($\approx$ 35 channels), and $f_w(x)$ is the time-walk correction function. The figure 600 corresponds to the minimum ionising particle (MIP) channel setting, where $t_w \to t$. The correction function $f_w(x)$ was obtained for each PMT separately using laser calibration data and is described in [50, 55].

Left-Right PMT Alignment

As described in section 2.2.4, each TOF scintillation counter has one PMT attached to each of the two ends. Each end measures the arrival time of the leading edge of the pulse generated by the PMT and the difference between the time measured at each end indicates the position along the length of the scintillation bar where the particle hits. Therefore, if the x coordinate is chosen such that 0 sits at the centre of the bar, the hit position x is

$$x = \frac{v\,(t_r - t_l)}{2} \tag{3.5}$$

where $t_{r(l)}$ is the time measured by the right (left) TDC and v is the velocity of light in the scintillator ($16\,cm/ns$).

If the particle hits the centre of the scintillator bar, the time measured by the left end and the right end should be the same. However, cable length delays and PMT delays for the left and right ends are different so an offset adjustment was required. A description of this adjustment is given in [47].

Detailed descriptions of the other steps involved in the calibration of the TOFs can be found in [50, 55].

Chapter 4

Data Analysis

This chapter describes the steps taken to calculate the inclusive, semi-inclusive and exclusive cross sections for ^{12}C and is summarised as follows:

Firstly, the particle identification in CLAS was checked to minimise contamination from misidentified particles. Electron momentum corrections were applied due to the ambiguity in the magnitude and shape of the CLAS magnetic field. Fiducial cuts were applied to all final state particles to reject particles that were incident near the edge of detectors.

To calculate the cross section, experimental yields were extracted from the data and charge normalisation was performed. The acceptance of the CLAS detector was calculated by simulating the response of the detector to correct for losses associated with the incomplete or imperfect detection of the final state. This allowed calculation of the cross section. Only a radiative correction still had to be applied before fitting the cross sections to extract the Δ peak centroids.

4.1 Particle Identification

The scattered electron identification is crucial to the analysis as every event requires its detection. During the experimental run, identification of the trigger particle must be made quickly based on the limited detector information available. At the cooking stage of the analysis, there is a specific set of criteria that the trigger particle must satisfy in order to be labelled an electron. The cooking software alone is not sufficient to distinguish between electron trigger particles and other non-electron triggers. The Electron Identification Correction used the fact that there is a linear relationship between the incident particle's momentum and the energy deposited in the Electromagnetic Calorimeter to define an "electron band". Trigger particles which lay inside the "electron band" were identified as electrons. This formed an extensive study and was written up for the members of the CLAS Collaboration. A full description of this

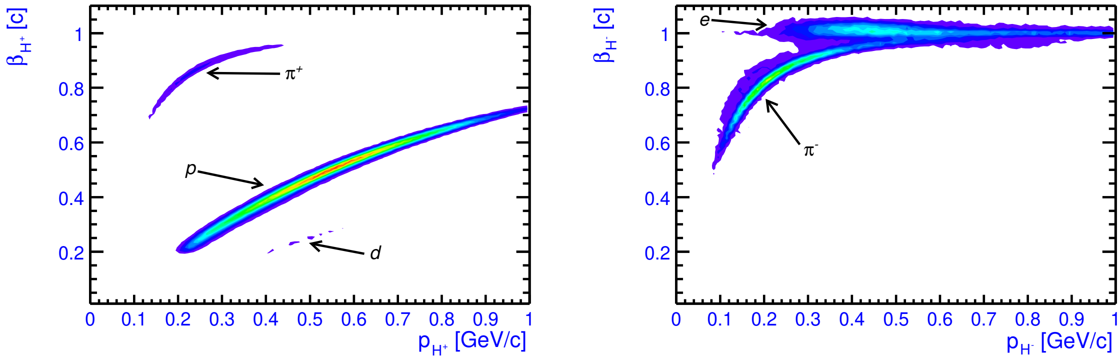

(a) Positive particles

(b) Negative particles

Figure 4.1: β_{tof} as a function of particle momentum.

study, and the results, are given in Appendix A.

Proton and pion identification was achieved by the time of flight and drift chamber detectors. The momentum of charged particles, p (GeV/c), and the path length from the event vertex to the time of flight detectors, R (m) were calculated using the curvature of the track through the drift chambers. The time taken for the particle to travel from the target to the time of flight detectors, t_{tof} (s), was also recorded. Thus, the velocity of the particle was calculated

$$\beta_{tof} = \frac{R}{ct_{tof}} \tag{4.1}$$

Figure 4.1 shows a plot of β_{tof} as a function of p for charged particles.

The particle velocity was also calculated using the momentum information from the drift chambers (given the particle mass, m (GeV/c^2))

$$\beta_{dc} = \frac{p}{\sqrt{p^2 + m^2}} \tag{4.2}$$

Particle identification was then the minimisation of

$$\Delta\beta = \beta_{tof} - \beta_{dc} \tag{4.3}$$

for the different particle masses (e.g.. proton, pion, kaon, etc.). There is a clear separation of the different particle bands shown in figure 4.1(a) but figure 4.1(b) clearly shows that further analysis is required to achieve separation of the electrons and π^-. This is described in Appendix A.

4.2 Other Corrections

Two further corrections had to be applied to the data before a full analysis could be carried out. The first of these was an electron momentum correction. This was applied because a slight ambiguity exists in the magnitude and shape of the magnetic field. This effect is only noticed in the electron measurement since the electron mass is small. The elastic scattering reaction with over determined kinematics was used to determine the electron momentum correction. In this case, the electron scattering angle was used to calculate the electron momentum. The comparison between calculated and measured momenta enabled the derivation of a correction function. The description of this correction was written for the Collaboration and is given in Appendix B.

The second correction applied was the fiducial cut. This cut rejected particles that were incident near the edges of the detectors and was necessary because the simulation is not totally reliable in these regions. Different cuts were derived for electrons, positive hadrons (protons) and negative hadrons (pions). The cuts for electrons are most important and were written up and submitted to the CLAS Collaboration. This forms Appendix C. The cuts for the hadrons are described below.

4.2.1 Hadron Fiducial Cuts

As is the case with the detection of electrons, the distribution of hadrons across the detection range in the azimuthal angle, ϕ_H, should be flat for fixed momentum, p_H, and polar angle, θ_H. A plot of ϕ_H is shown in figure 4.2 which clearly shows that the number of counts across ϕ_H drop off at the edges of the detection area. The fiducial cut discards events that lie at extreme ϕ_H leaving the flat region in the centre.

This cut should be derived in the same way that the fiducial cuts for electrons were derived (see Appendix C), but it was sufficient to employ a simplified version. Distributions of θ_H against ϕ_H were created for positive and negative hadrons. The function

$$\phi_H = \begin{cases} \frac{a(\theta_H - c)}{[\theta_H - c + (b/a)]} & \phi_H > 0, \text{ forward } \theta_H \text{ region} \\ \frac{a(c - \theta_H)}{[\theta_H - c + (b/a)]} & \phi_H < 0, \text{ forward } \theta_H \text{ region} \\ \frac{a(150 - (\theta_H + c))}{[(b/a) - (\theta_H + c) + 150]} & \phi_H > 0, \text{ backward } \theta_H \text{ region} \\ \frac{a((\theta_H + c) - 150)}{[(b/a) - (\theta_H + c) + 150]} & \phi_H < 0, \text{ backward } \theta_H \text{ region} \end{cases}$$

was superimposed on the data where a, b, and c are the fit parameters. Further details of these functions can be found in [56]. Figure 4.3 shows an example of the angular distributions with the function superimposed. The parameters were adjusted until each momentum bin showed flat acceptance over the region enclosed by the functions. The effect of the cut is shown in figure 4.4. Only protons were used to derive the positive hadron fiducial cut. Similarly, only π^- were used to construct the negative hadron

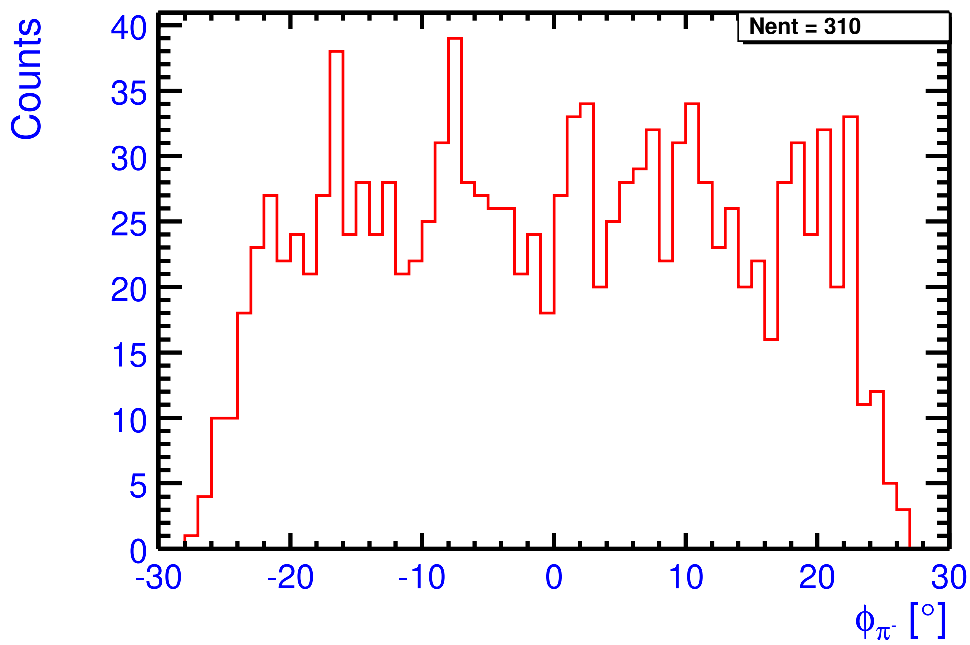

Figure 4.2: Distribution of ϕ_H for $p_H = 0.250 \pm 0.050\, GeV/c$ and $\theta_H = 67.5 \pm 2.5°$

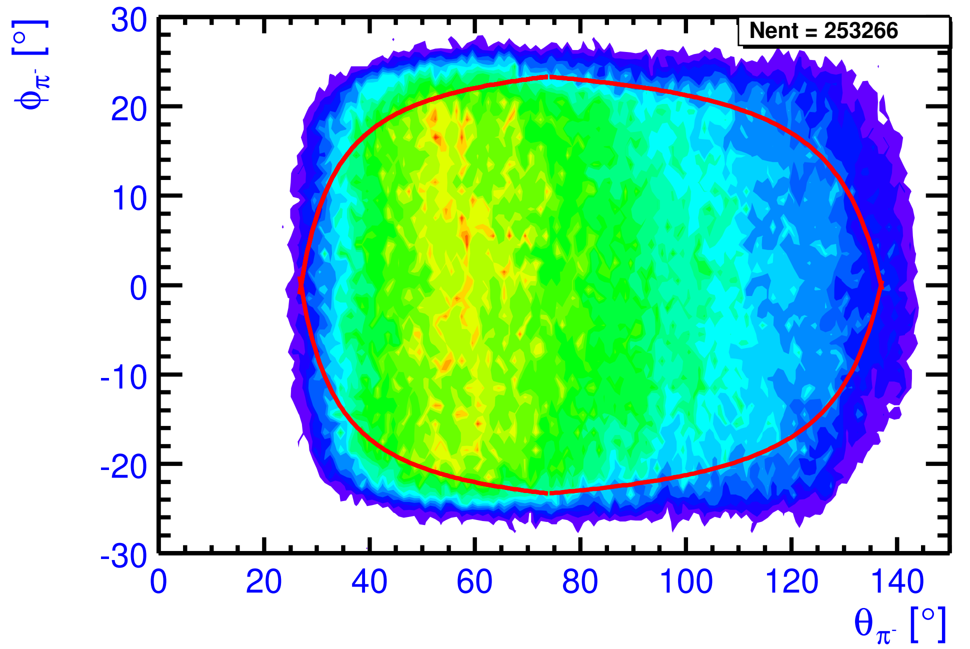

Figure 4.3: Hadron angular distribution showing the fiducial cut. Only hadrons that lie inside the area defined by the fiducial function (red) are accepted as detected.

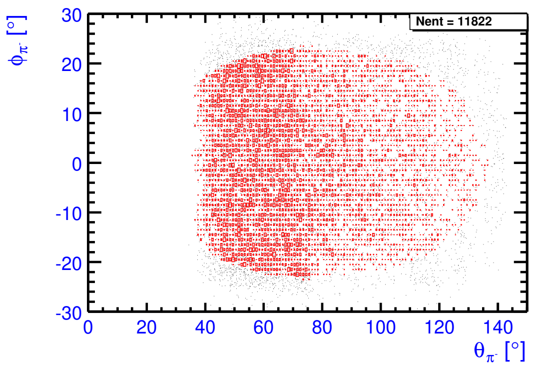

(a) Example angular distribution before and after the fiducial cut ($p_H = 0.250 \pm 0.050\, GeV/c$). The distribution after the cut is shown in red.

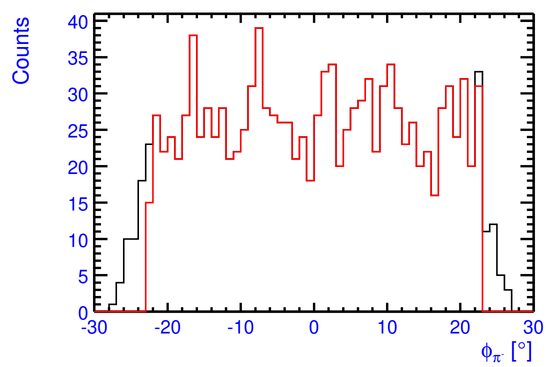

(b) Example trapezoid distribution before and after the fiducial cut ($p_H = 0.250 \pm 0.050\, GeV/c$, $\theta_H = 67.5 \pm 2.5\,°$). The distribution after the cut is shown in red.

Figure 4.4: Comparison of hadron angular and trapezoid distributions before and after the fiducial cut.

fiducial cut since these are the only particles of interest in the final state of the present measurement.

From this point it is assumed that all the corrections above were applied to the data.

4.3 Extraction of Yields

The total number of triggers recorded in the experiment was 29, 756, 849. Of this, 6, 133, 176 events were used for the following analysis. Before any cross sections could be calculated the experimental yields were obtained from the data. For the inclusive case this was quite straightforward. A histogram of Q^2 (invariant mass squared of the virtual photon) against W (mass of the recoiling hadronic system) was created using all the events. For the semi inclusive case, the same histogram was created using only events where a π^- was also detected. The exclusive case enabled a more thorough analysis to be carried out to obtain a more accurate measurement of the position of the Δ peak.

In the exclusive case the three particles (e', p and π^-) in the reaction ${}^{12}C\,(e, e'p\pi^-)\,X$ were detected. This allowed the construction of the four vector of the recoil, X. The distribution of the invariant mass of the recoil is shown in figure 4.5. This is defined as the missing mass and will be M_{11_C} in the case that the final state is fully detected. By cutting on this quantity, the exclusivity of the event is increased. To conserve charge the reaction must have taken place on a neutron. The peak position in figure 4.5 is

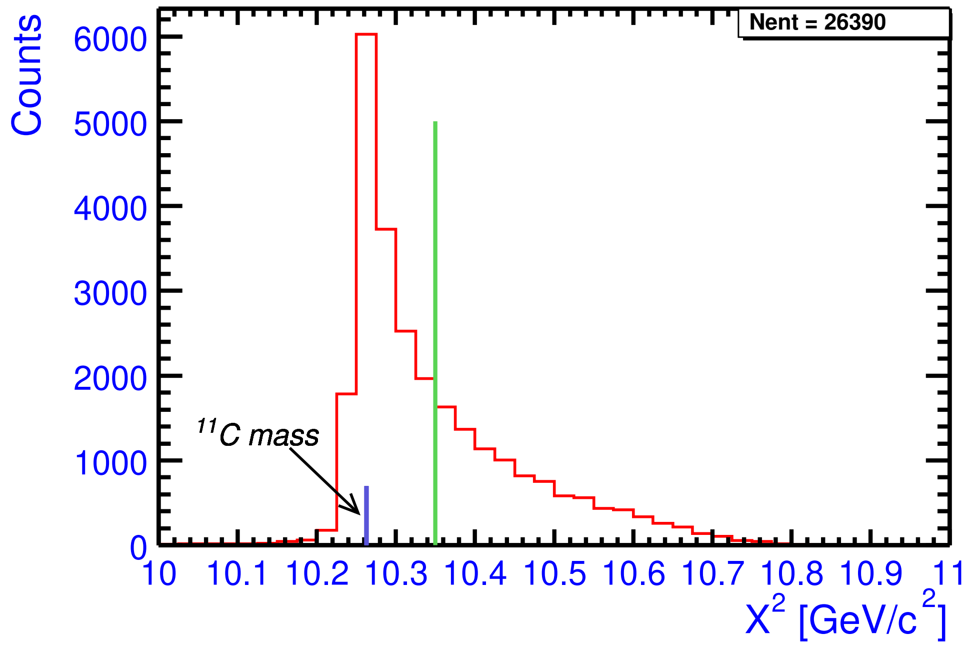

Figure 4.5: Invariant mass of the recoil, X^2, in the reaction $^{12}C\,(e, e'p\pi^-)\,X$. The ^{11}C mass is shown. The green line ($X^2 = 10.35\,GeV/c^2$) represents the upper limit of accepted events for analysis.

at $10.263\,GeV/c^2$ (the mass of ^{11}C). The tail to lower invariant mass is the effect of the detector resolution. Events where the mass of the recoil is significantly greater than the mass of ^{11}C include those where the recoil existed in an excited state and those where other particles were produced but not detected. It is also possible that the electron (the incident or the scattered one) radiated one or more photons. In this case the kinematics of the event are changed leading to an increase in the missing mass. To minimise this contamination, only events below $X^2 = 10.35\,GeV/c^2$ were accepted. This rejects events where an extra pion could have been produced. As with the inclusive and semi inclusive yields, a histogram of Q^2 against W was created for data matching the exclusive criteria. A histogram of Q^2 against $M_{p\pi^-}$ (the mass of the proton-π^- system) was also created.

One other yield was extracted from the data. This was the equivalent yield that Sealock *et al.* [3] measured to give a check of the normalisations involved when calculating the cross section for the experiment. In the experiment of Sealock *et al.* [3] a fixed angle spectrometer at a polar angle of 37.5° was employed. Different values of Q^2 at the Δ peak were obtained using four different beam energies. To make a comparison, values of ω (energy of the virtual photon) and $|\mathbf{q}|$ (momentum of the virtual photon) for each bin in W were calculated. Then, by selecting electrons from our experiment with

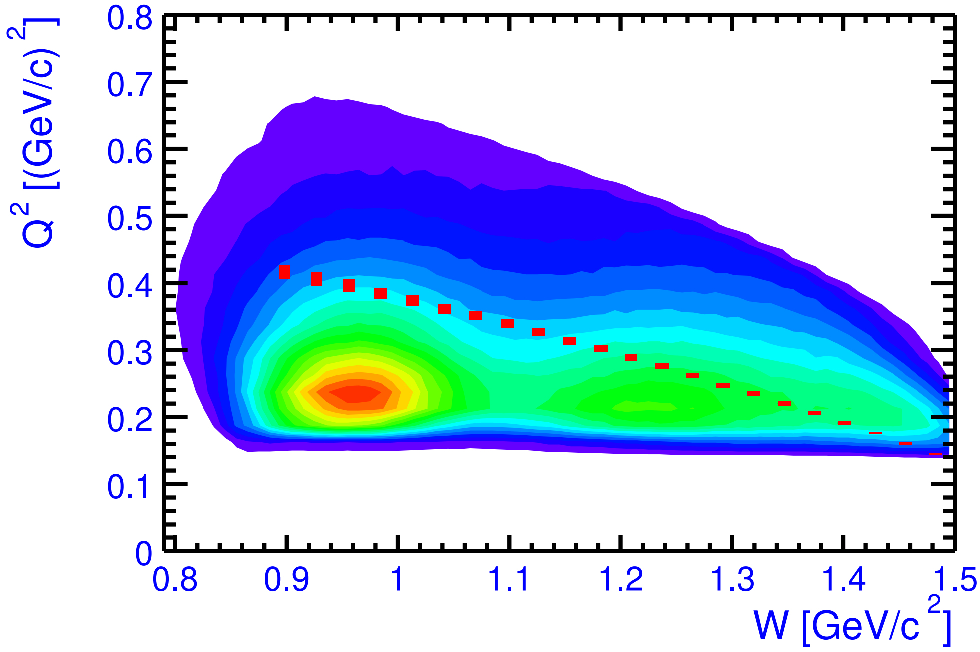

Figure 4.6: Kinematics of the data used for the normalisation check. The contoured histogram is all the experimental data. The red boxes show the bins used to calculate the cross section of Sealock *et al.* [3].

the same $\omega\,(\pm\Delta\omega)$ and $|\mathbf{q}|\,(\pm\Delta\,|\mathbf{q}|)$ as used by Sealock *et al.* [3], the same cross section was calculated. The bin widths were chosen to be 20 MeV and 20 MeV/c respectively. The data then spans the ranges shown in figure 4.6. The experimental yield in this case is shown in figure 4.7.

4.4 Charge Normalisation

The total charge incident on the target, Q_{tot}, was calculated using scaler information from the detector. Only a very small percentage of the incident electrons interacted in the target. Most passed straight through and were collected in a Faraday cup. The Faraday cup was reset at the start of each run. The value of accumulated charge was read out in the scaler data stream every ten seconds and at the end of the run the number of triggers, N_t, and the value of total charge, Q_{tot}, were entered in the run log. These numbers were used to construct figure 4.8. The ratio N_t/Q_{tot} should be constant throughout the data taking period (for a fixed magnetic field) but figure 4.8 shows that there were fluctuations in the beam current and detector dead time. Therefore a correction was applied to account for this.

Only data taken during stable beam and detector conditions were selected for anal-

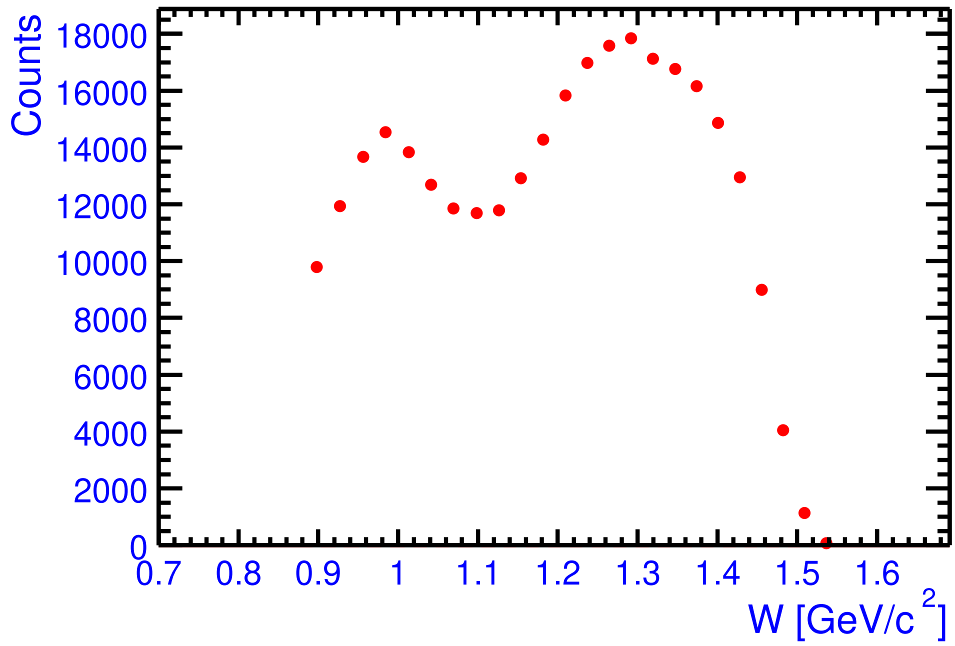

Figure 4.7: Experimental yield for the normalisation check

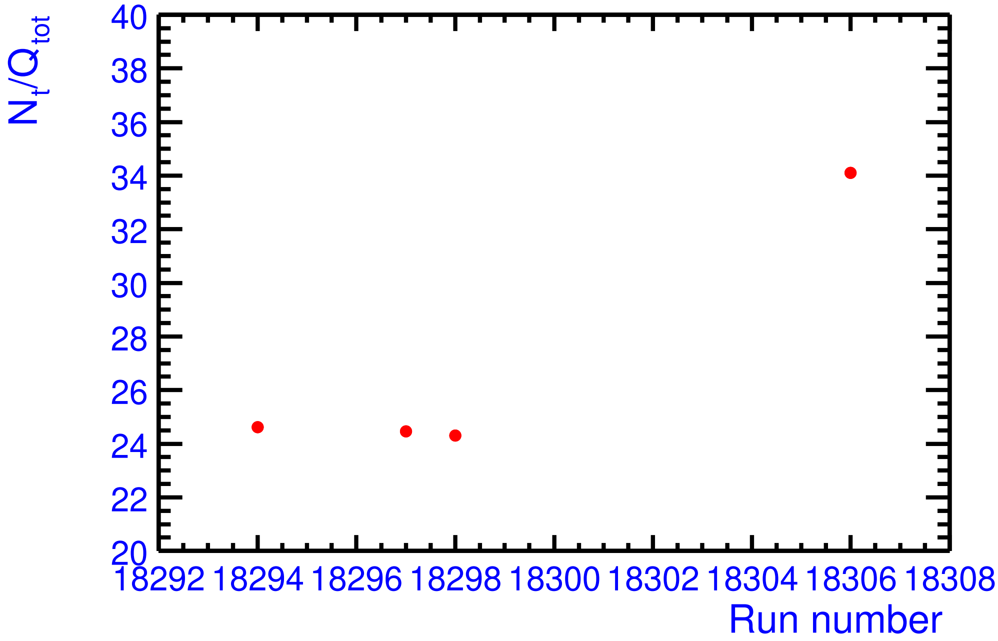

Figure 4.8: Run by run ratio of the number of triggers to the total beam charge.

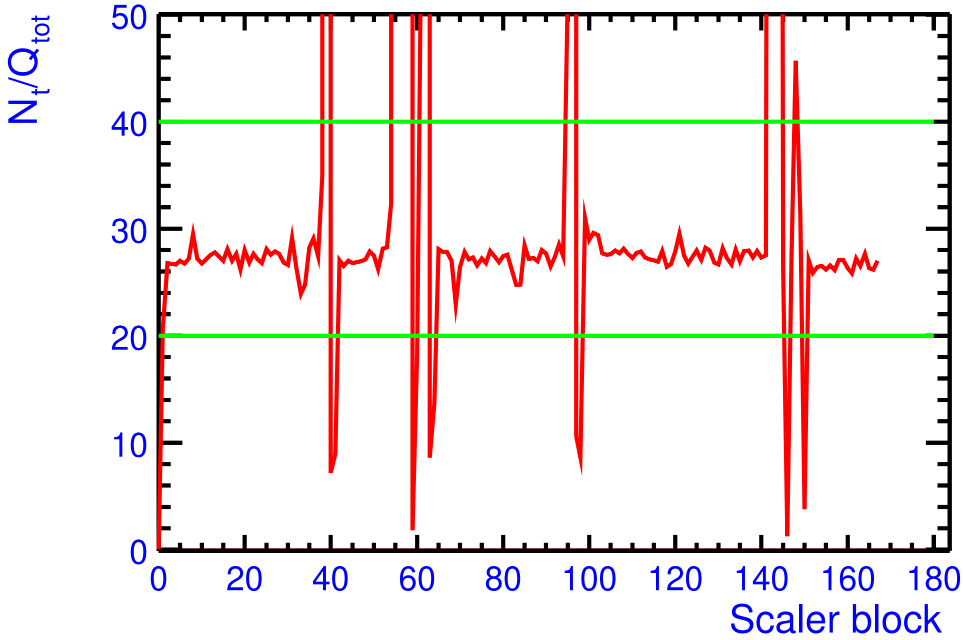

Figure 4.9: Ratio N_t/Q_{tot} for each scaler block in run 18294.

ysis. To select these events, instead of looking at conditions over the entire run, conditions between each scaler read out were examined. The time between scaler reads (ten seconds) was defined as a scaler block. The ratio N_t/Q_{tot} was calculated for each scaler block. The result of this shown in figure 4.9 for a selected run. Figure 4.9 shows that some scaler blocks contain data where the beam or detector did not work properly e.g. the beam was switched off for a short period of time. These events were discarded by placing cuts around the stable region (see figure 4.9). After applying the cut, the remaining events, N_{events}, and the charge, Q_{cut}, were used for the analysis. The cuts were slightly different for the different runs (of the same magnetic field) since there were different fluctuations in the beam current and detector dead time. Figure 4.10 shows the ratio N_{events}/Q_{cut} after these cuts were applied.

4.5 Acceptance Correction

The acceptance correction is the technique for correcting the experimental data for losses associated with the incomplete or imperfect measurement of the final state [57]. Not all of the interactions being studied result in a recordable and analysable reaction from the detector. In order to correctly measure the physics being studied, an acceptance correction was applied to the detected events. Many different factors influence whether the event was detected. The dominant one is the outgoing particle's momen-

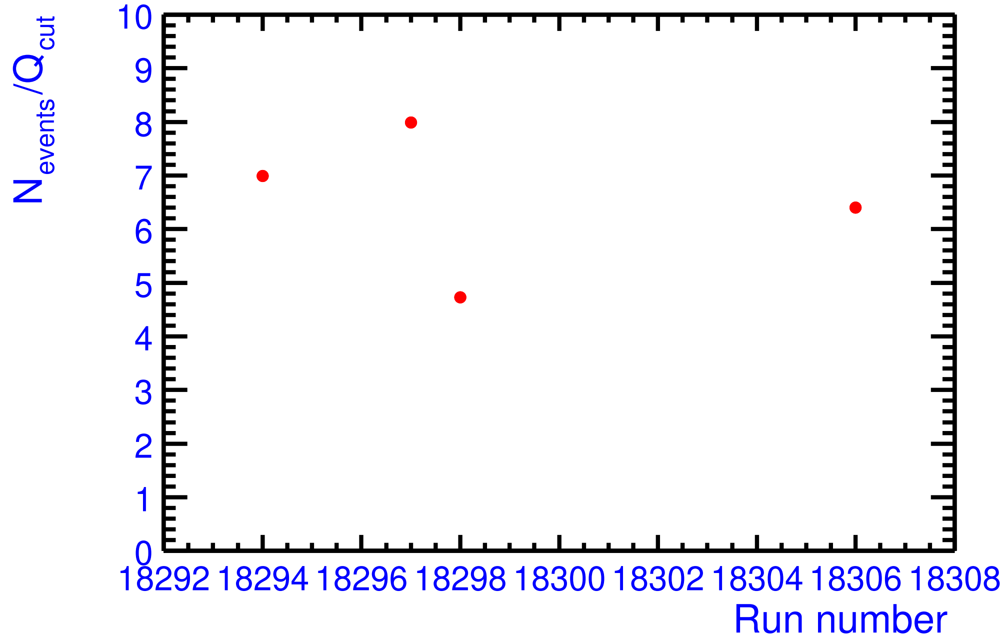

Figure 4.10: Run by run ratio of the number of events to the total beam charge.

tum due to the physical geometry of the detector. Other factors include differences of specific detector components, interactions of the outgoing particles, and inefficiencies in the reconstruction of the event due to the resolutions of the hardware etc.

To correct for these effects, events were generated and passed through a detailed detector response simulation. In this case the effect the detector has on the data is known, and can be corrected. To be consistent, exactly the same analysis was performed on the simulated data as was on the experimental data.

4.5.1 Event Generator

Two event generators were tried for the purpose of simulation before deciding to create a new one. The CLAS software contains computer programs to generate events for simulation. "CELEG", the CEBAF Large Acceptance Spectrometer Event Generator, generates events according to parameterised cross sections for most of the processes that can occur when an electron interacts with a nucleon. It was not possible to generate events across the desired range of W and Q^2 using CELEG. The second event generator provided is "psg", the Phase Space Generator. This specifically generates events with at least three particles in the final state and so was not applicable in the inclusive or semi inclusive analysis. Therefore a new event generator was created which incorporated the three channels of interest. The problem was simplified by considering events in all of phase space so that the kinematics of each event are the only consideration. The

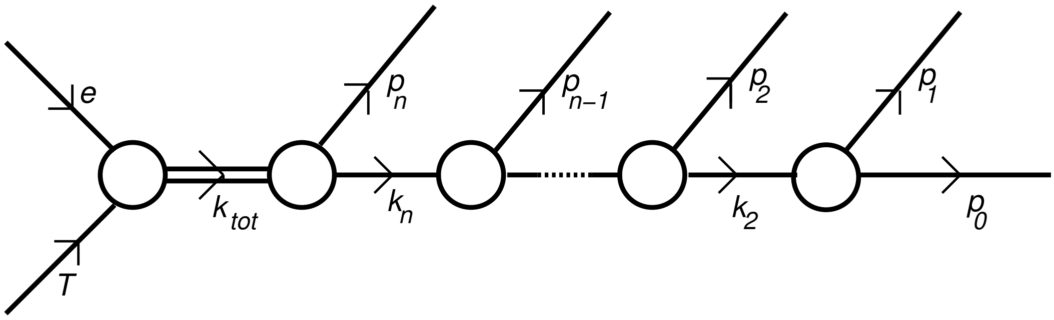

Figure 4.11: Schematic of the generation of an n particle final state.

kinematics detailed below are described in more detail in [58].

The production of a multi particle final state can be thought of as a sequence of two particle decays of the total energy of the system defined by the incident electron and target. Figure 4.11 shows this schematically for an n particle final state with residual p_0. Then

$$s^2 = (\mathrm{e} + \mathrm{T})^2 \tag{4.4}$$

is defined as the total energy.

In this system the numbers to be generated randomly are the angles of the product particles (in the centre of mass of the decaying particle) and the masses of the intermediate states. In all cases the angles are distributed uniformly in $(\cos\theta, \phi)$ space according to

$$\left.\begin{array}{rcl} \phi_i & = & 2\pi P_i \\ \cos\theta_i & = & 2Q_i - 1 \end{array}\right\} \qquad i = 0, 1, ..., n \tag{4.5}$$

where P_i and Q_i are random numbers between 0 and 1. The mass of the intermediate particle j is given by

$$M_j = \mu_j + R_j\left(M_{j+1} - \mu_{j+1}\right) \qquad j = 2, 3, ...n \tag{4.6}$$

where R_j is a random number between 0 and 1 and

$$\mu_j = M_{p_0} + M_{p_1} + ... + M_{p_{j-1}} \tag{4.7}$$

The kinematics for each individual case is described below.

Inclusive

The simplest case is the inclusive generation where only one decay is performed. Figure 4.11 reduces to figure 4.12. The four vectors e, T and therefore $\mathrm{k_{tot}}$ are fixed. Angles for the product particles were generated as described above. Only the mass of X, M_X,

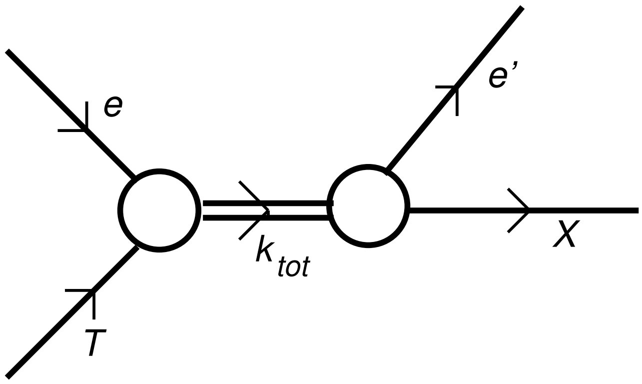

Figure 4.12: Schematic diagram representing the generation of inclusive events.

was left to be generated. Equation 4.6 becomes

$$M_X = M_{^{12}C} + R_1 \left[s - \left(M_{^{12}C} + M_{e'} \right) \right] \tag{4.8}$$

giving

$$M_{^{12}C} \leq M_X \leq s - M_{e'} \tag{4.9}$$

The electron mass is included for completeness. Figure 4.13 shows the resulting distribution of M_X.

The resulting electron four vector was recorded in the appropriate format to be simulated by GSIM.

Semi Inclusive

In the $^{12}C\,(e, e'\pi^-)\,X$ reaction figure 4.11 reduces to figure 4.14. Angles were generated as described by equation 4.5. The masses of the intermediate particles are given by

$$\begin{aligned} M_2 &= \left(M_{^{12}C} + M_{\pi^-} \right) + R_2 \left[s - \left(M_{^{12}C} + M_{\pi^-} + M_{e'} \right) \right] \\ M_X &= M_{^{12}C} + R_1 \left[M_2 - \left(M_{^{12}C} + M_{\pi^-} \right) \right] \end{aligned} \tag{4.10}$$

thus

$$\begin{aligned} M_{^{12}C} + M_{\pi^-} \leq M_2 \leq & \quad s - M_{e'} \\ M_{^{12}C} \leq M_X \leq & \quad M_2 - M_{\pi^-} \end{aligned} \tag{4.11}$$

Figure 4.15 shows the distributions of M_2 and M_X.

The four vectors of the electron and pion were stored, ready for simulation.

Exclusive

For this three particle final state, the reaction is shown in figure 4.16. Angles were again generated as defined by equations 4.5. The masses M_X, M_2 and M_3 are defined

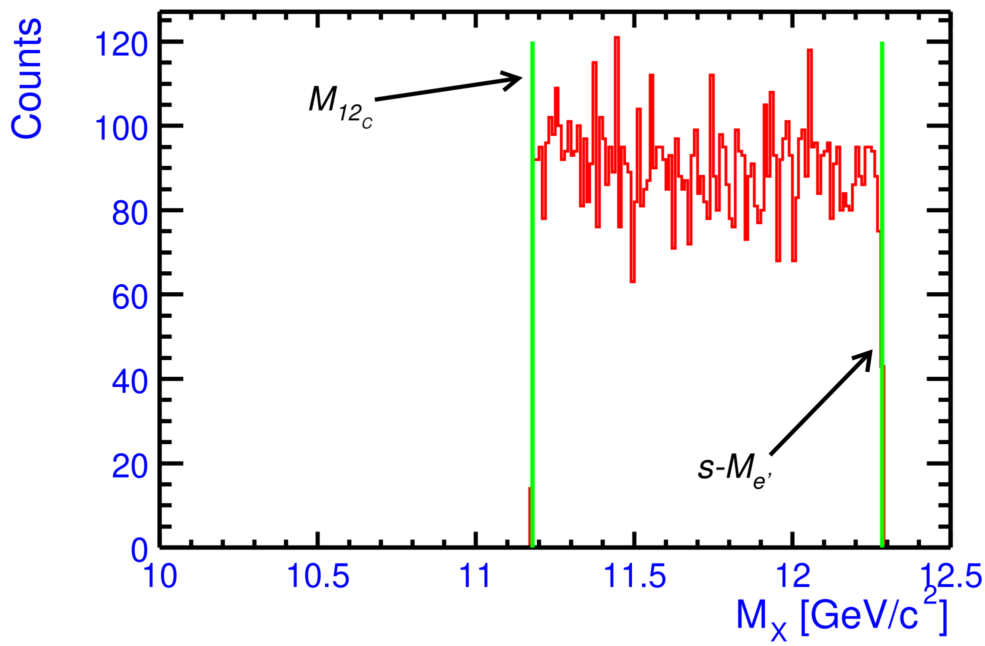

Figure 4.13: Mass of the recoil, M_X, for the inclusive event generation. The green lines correspond to the limits calculated in equation 4.9.

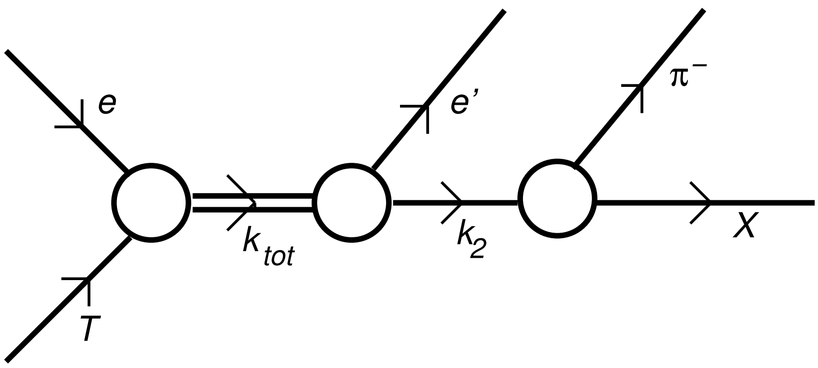

Figure 4.14: Schematic diagram representing the generation of semi inclusive events.

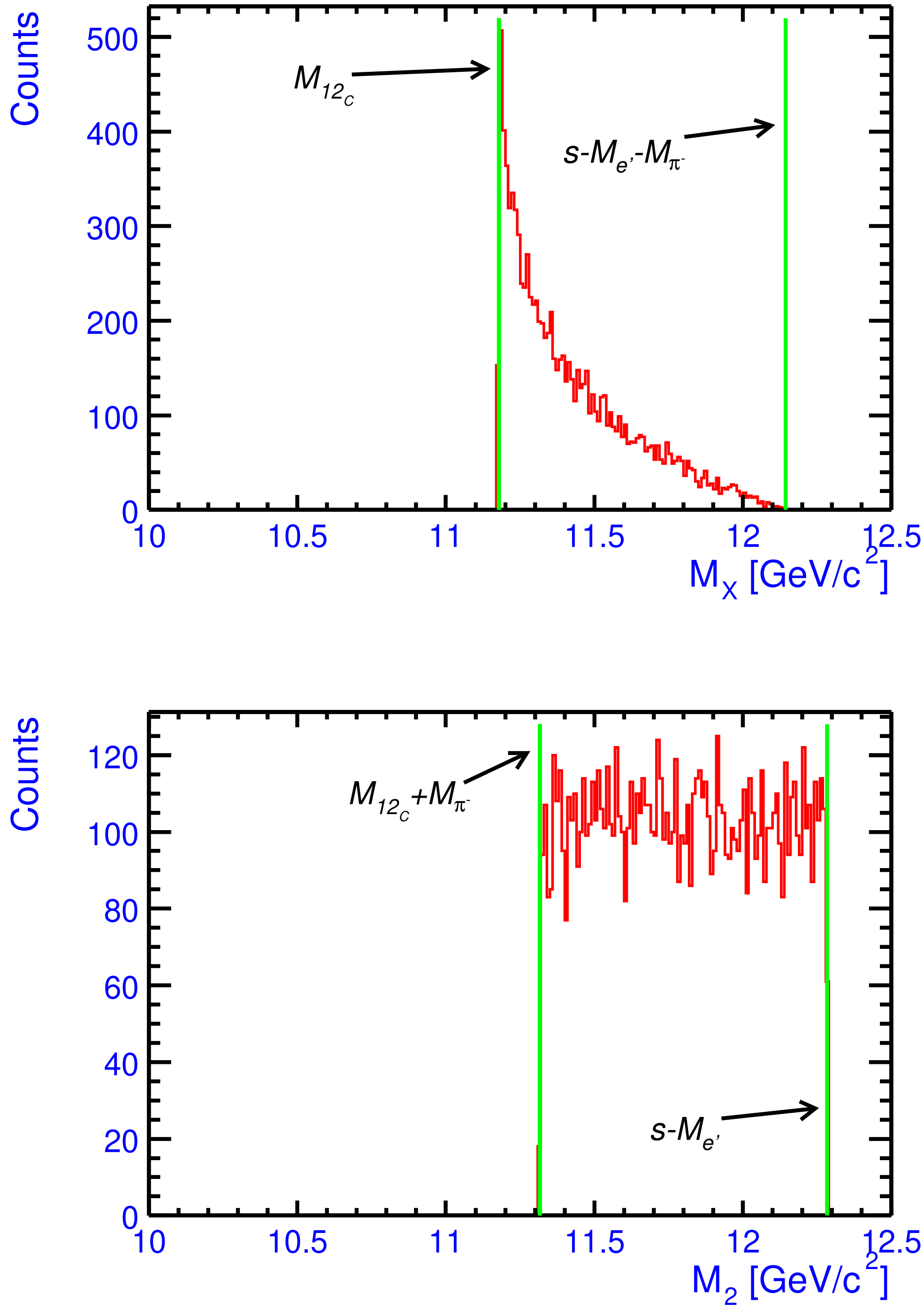

Figure 4.15: Mass of the recoil, M_X, and intermediate decay particle, M_2, for the semi inclusive generation. The green lines correspond to the limits calculated in equation 4.11.

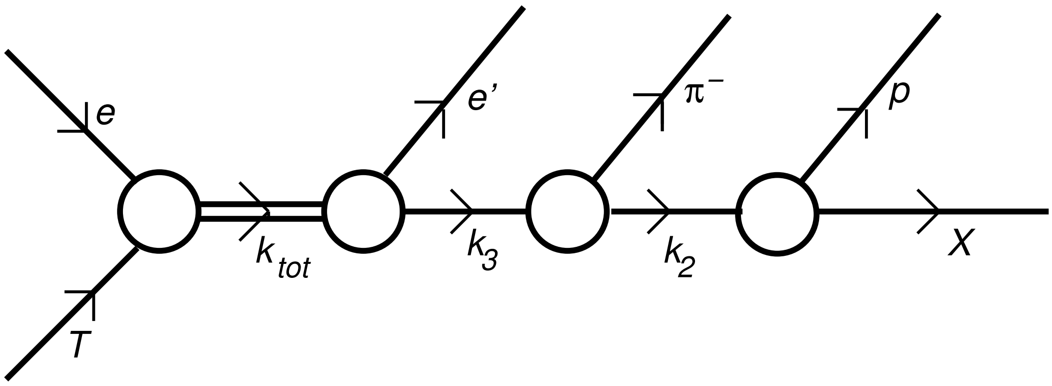

Figure 4.16: Schematic diagram representing the generation of exclusive events.

below. Note that the lowest possible recoil mass is the mass of ^{11}C (M_{11_C}).

$$\begin{aligned} M_3 &= (M_{11_C} + M_p + M_{\pi^-}) + R_3 \left[s - (M_{11_C} + M_p + M_{\pi^-} + M_{e'})\right] \\ M_2 &= (M_{11_C} + M_p) + R_2 \left[M_3 - (M_{11_C} + M_p + M_{\pi^-})\right] \\ M_X &= M_{11_C} + R_1 \left[M_2 - (M_{11_C} + M_p)\right] \end{aligned} \tag{4.12}$$

Therefore,

$$\begin{aligned} M_{11_C} + M_p + M_{\pi^-} \leq M_3 &\leq s - M_{e'} \\ M_{11_C} + M_p \leq M_2 &\leq M_3 - M_{\pi^-} \\ M_{11_C} \leq M_X &\leq M_2 - M_p \end{aligned} \tag{4.13}$$

Figure 4.17 shows the distributions of M_X, M_2 and M_3.

As for the inclusive and semi inclusive cases, the four vectors of the electron, pion and proton were stored as input for the simulation.

One additional condition was placed on the generation of all the events above. The scattered electron, once transformed to the lab frame, had to have a polar angle in the range $15.0 \leq \theta_{e'} \leq 60.0°$ because electrons below 15.0° are not detected and electrons with a scattering angle above 60.0° are generally not produced in the experiment - the cross section is so small at those large angles that they do not contribute. This was applied to reduce the computing time taken to simulate events.

4.5.2 Simulation

GSIM is the GEANT Simulation package that is distributed as part of the CLAS software packages. GEANT is a system of detector description and simulation tools that help physicists design and optimise detectors, develop and test reconstruction and analysis programs, and interpret experimental data. It was devised in CERN in 1974 when it was just a bare framework that initially emphasised tracking of a few particles

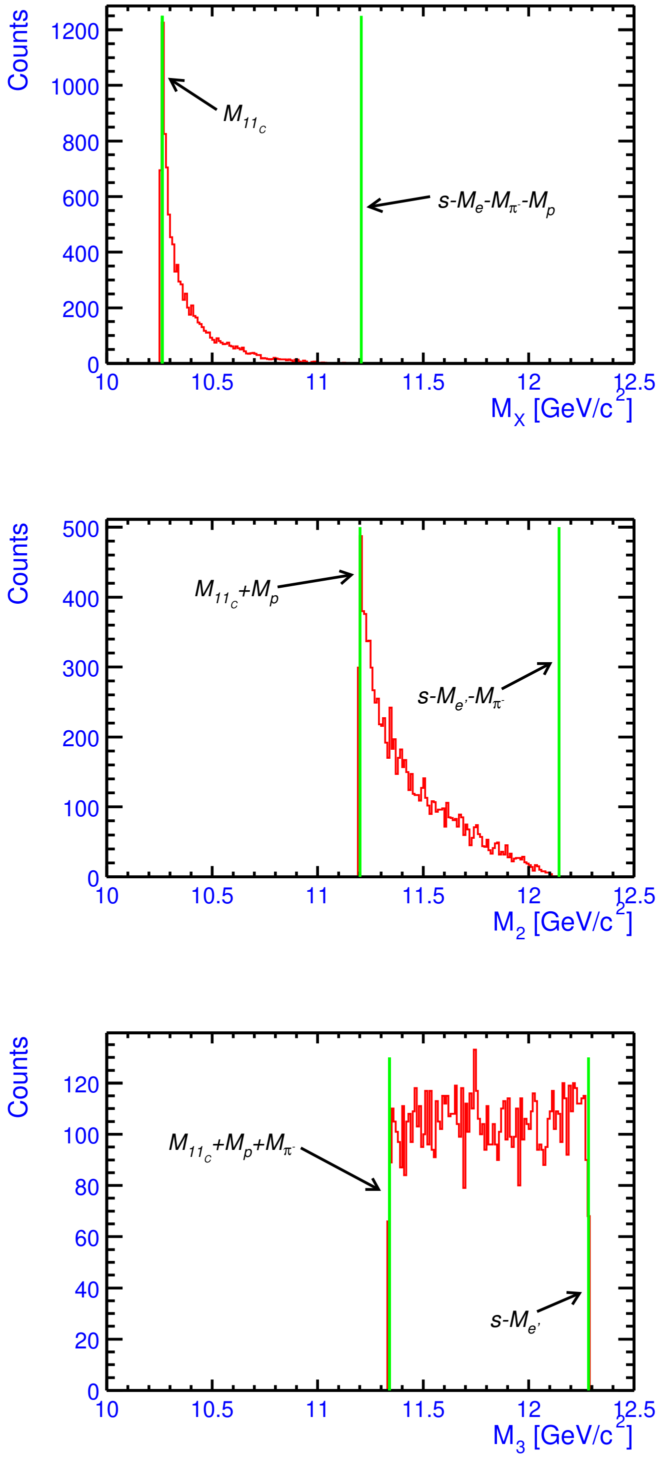

Figure 4.17: Mass of the recoil, M_X, and intermediate decay particles, M_2 and M_3, for the exclusive generation. The green lines correspond to the limits calculated in equation 4.13.

per event through relatively simple detectors. The system has been developed over the years and we are currently using version 3.21.

The GEANT program simulates the passage of elementary particles through matter. The principle applications of GEANT in High Energy Physics are:

1. the transport of particles through an experimental setup for the simulation of detector response;
2. the graphical representation of the setup and of the particle trajectories.

The GEANT system allows you to:

- Describe an experimental setup by a structure of geometrical volumes;
- Accept events simulated by Monte Carlo generators;
- Transport particles through the various regions of the setup, taking into account geometrical volume boundaries and physical effects according to the nature of the particles themselves, their interactions with matter and magnetic fields;
- Record particle trajectories and the response of the detectors;
- Visualise the detectors and the particle trajectories

GSIM is really GEANT containing all the CLAS specific elements required to fully simulate an experiment in CLAS. This has been developed over many years and is now an extremely complicated system of software [59]. Everything from scintillator bars to beam line components are included in the simulation. Routines exist to input and output the data in the format that is common to all CLAS experiments. This allows the simulated data to be treated in exactly the same way as the experimental data. The experiment specific details, such as the target [60], were added by collaboration members.

The generated events were input to GSIM with the condition that the events start in the target to ensure that effects like multiple scattering are properly accounted for. The only differences between the output of GSIM and the output from the experiment are:

- there are no resolution effects;
- there is no trigger;
- there is no accounting for dead detector channels.

These differences are incorporated by the GSIM Post Processor, GPP. GPP "smears" the time of flight and momentum quantities to produce a resolution that is comparable with that of the detector. The trigger conditions were also applied (see section 2.3) so that only events passing the trigger are accepted. Finally the dead detector channels in the experiment were removed so that the simulation matched the experimental conditions.

After the post processing the data is cooked (see section 3.1). This incorporates particle id etc. and provides output four vectors.

4.5.3 Acceptance

"Acceptance" is a vague term but here it is defined as a combination of the geometrical acceptance of the detector and the efficiency with which particles, or final states, are measured. For example, one of the generated electrons could scatter into a coil of the magnet and therefore would not be detected because there is no detector to detect it. However, in a different event, the electron could enter the electromagnetic calorimeter and not be detected as an electron. This contributes to an efficiency with which electrons are detected. This efficiency, in general, decreases as the number of final state particles increases. Both these effects are combined to define acceptance. The geometrical acceptance can be calculated by applying fiducial cuts to all the particles in the final state (see section 4.2.1 and appendix C). The detection efficiency can only be calculated by utilising the full simulation as described above.

In terms of this analysis, the acceptance is calculated for each (W, Q^2) and $(M_{p\pi^-}, Q^2)$ bin. To achieve this, the fiducial cut was applied to both the generated and accepted[1] data and then both data sets were passed through the analysis procedure so that all the appropriate cuts were applied. This is described in section 4.2 and is different for the different reaction channels being studied. The acceptance is then defined as

$$\epsilon_{i,j} = \frac{N_{i,j}^{accepted}}{N_{i,j}^{generated}} \qquad i = 1, 2, ..., N_W \text{ and } j = 1, 2, ...N_{Q^2}$$

The number of bins in W, N_W, is 90. The number of bins in Q^2 is 32 for the inclusive and semi inclusive measurements and 16 for the exclusive.

The $\epsilon' s$ were used when calculating the cross sections discussed in section 4.6.

[1]Generated data is the output of the event generator. Accepted data is the output of cooking

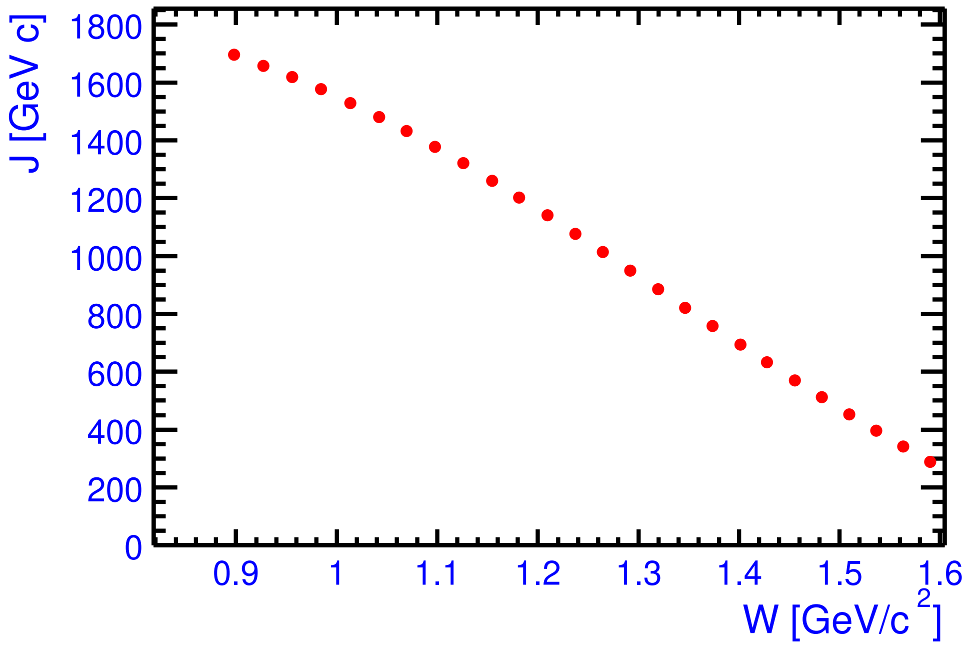

Figure 4.18: Jacobian factor, J, as a function of W.

4.6 Determination of Cross Sections

Two cross sections were measured in this analysis: the equivalent cross section to that of Sealock *et al.* [3] and the cross section that forms the results of this analysis.

Sealock *et al.* measured the cross section $d^2\sigma/d\Omega dE'$ where Ω $[str]$, is the solid angle of the detector and E' $[MeV]$ is the scattered electron energy. In extracting the yield, bins in ω and q were used (see section 4.3). For comparison, the most straightforward approach was to calculate $d^3\sigma/d\omega dq d\phi$:

$$\frac{d^3\sigma}{d\omega dq d\phi} = N_e \cdot \left(\frac{Q_e}{Q_{tot}}\right) \cdot \left(\frac{1}{\epsilon}\right) \cdot \frac{A}{(\rho_t l_t N_A)} \cdot \frac{1}{\Delta\omega\Delta q\Delta\phi} \tag{4.14}$$

This was then converted to $d^2\sigma/d\Omega dE'$ using equations 4.15 and 4.16.

$$\frac{d^2\sigma}{d\Omega dE'} = \left| J\left(\frac{\cos\theta, E'}{\omega, q}\right)\right| \frac{d^3\sigma}{d\omega dq d\phi} \tag{4.15}$$

$$J\left(\frac{\cos\theta, E'}{\omega, q}\right) = \begin{vmatrix} \frac{\partial(\cos\theta)}{\partial\omega} & \frac{\partial(\cos\theta)}{\partial q} \\ \frac{\partial E'}{\partial\omega} & \frac{\partial E'}{\partial q} \end{vmatrix} = 1000 \times \frac{E_e E_{e'}}{q} \tag{4.16}$$

The variation of the Jacobian factor across the range of ω is shown in figure 4.18.

The cross section for electron scattering can be written as shown in equation 1.5.

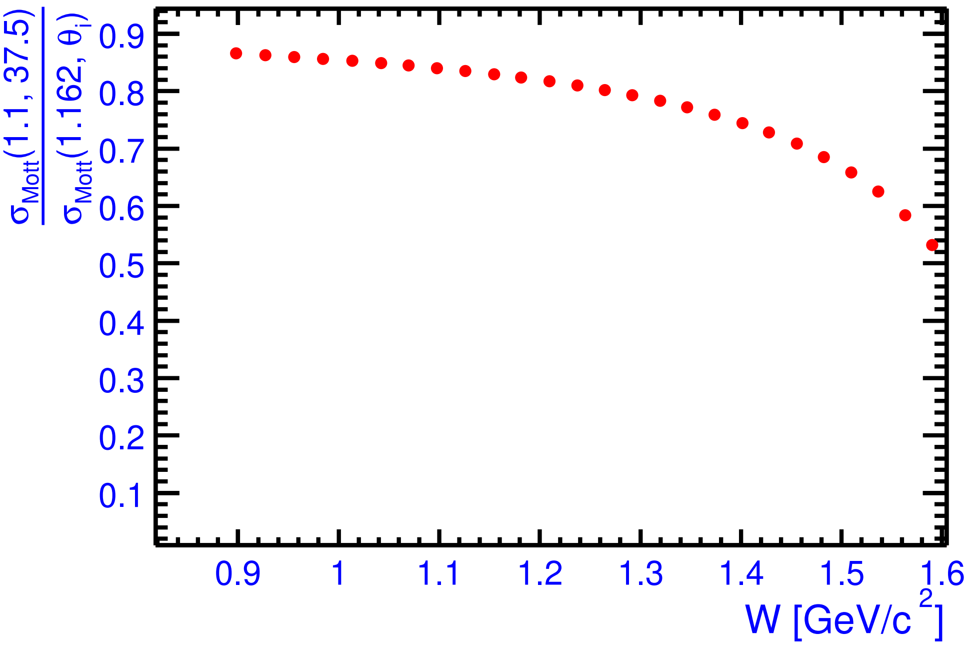

Figure 4.19: Ratio of Mott cross sections as a function of W.

Since the cross section of Sealock *et al.* [3] and that of the present measurement were obtained at different beam energies a correction had to be applied to allow a comparison to be made. In equation 1.5, the term σ_{Mott} was replaced by multiplying by the factor $\sigma_{Mott}|_{1.1,\,37.5} \,/\, \sigma_{Mott}|_{1.162,\,\theta_i}$, effectively removing the kinematic dependency of the present measurement whilst leaving the physics unchanged. This ratio is shown in figure 4.19.

A different cross section was calculated to search for the Q^2 variation reported in [3]. As a Q^2 variation of the Δ mass was being investigated, the cross section $d^2\sigma/dQ^2dW$ was measured. Experimentally this is given by

$$\frac{d^2\sigma}{dQ^2dW} = N_e \cdot \left(\frac{Q_e}{Q_{tot}}\right) \cdot \left(\frac{1}{\epsilon}\right) \cdot \frac{A}{(\rho_t l_t N_A)} \cdot \frac{1}{\Delta Q^2 \Delta W} \tag{4.17}$$

where

$$\begin{aligned}
N_e &= \text{Number of electrons in the } Q^2, W \text{ bin} \\
Q_e &= \text{Electronic charge } (1.602 \times 10^{-19}) \;\; [C] \\
Q_{tot} &= \text{Total charge incident on the target } [C] \\
\epsilon &= \text{Acceptance factor for the } Q^2, W \text{ bin} \\
A &= \text{Mass number of the target } [g/mol] \\
\rho_t &= \text{Target density } (1.786 \pm 0.034) \;\; [g/cm^3] \\
l_t &= \text{Target length } (0.1 \pm 0.002)\, [cm] \\
N_A &= \text{Avogadro's Number } (6.022 \times 10^{23}) \;\; [1/mol]
\end{aligned}$$

The values of ρ_t and l_t were obtained from [61].

4.7 Radiative Correction

There is a non-negligible probability that an electron will emit a photon in the field of an atom or nucleus. Experimentally this means that the electron that interacted with the nucleus had less energy than the beam energy or the scattered electron had more energy than was detected. In either case the virtual photon transferred did not have the energy calculated using the detected electron. The effect of this was studied using the "qfs" computer code [62] used by Sealock *et al.* to correct that data. One of the outputs from [62] is the ratio of radiative corrected to uncorrected cross sections for specified kinematics. This was used to produce a radiative correction to the data and an example of this correction is shown in figure 4.20. This was applied to the inclusive and semi inclusive cross sections. For the exclusive cross sections a different approach was adopted. As discussed in section 4.3, the invariant mass of the recoil (X^2) was calculated for this reaction channel. The effect of an electron radiating a photon is to move the event to higher invariant mass. To assess whether this contributes, the cross section was calculated for two different regions of invariant mass. The regions were $X^2 < 10.275\, GeV/c^2$ and $10.275 \leq X^2 \leq 10.35\, GeV/c^2$. A comparison of the resulting cross sections is shown in figure 4.21 which shows that the radiative effect is not measurable and therefore no action was taken.

4.8 Fitting Procedure

The fitting procedure for each reaction channel will be discussed separately. Generally, resonances were fitted with a Breit Wigner function while backgrounds were fitted with polynomials. These functions were chosen based on the qfs computer program [62] that was used by Sealock *et al.* [3].

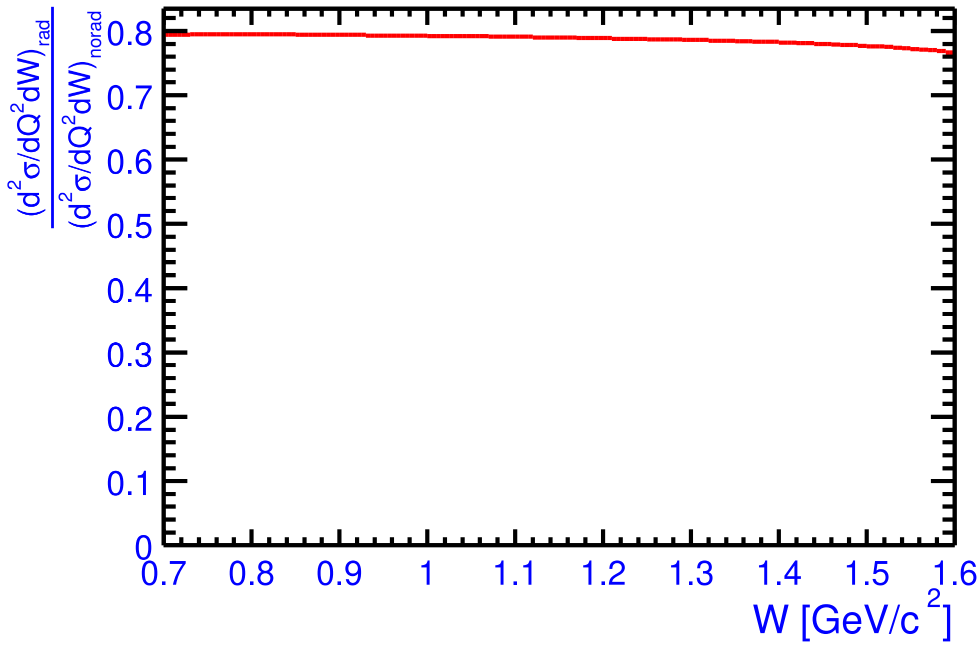

Figure 4.20: Radiative correction for $Q^2 = 0.3125 \pm 0.0125\ (GeV/c)^2$.

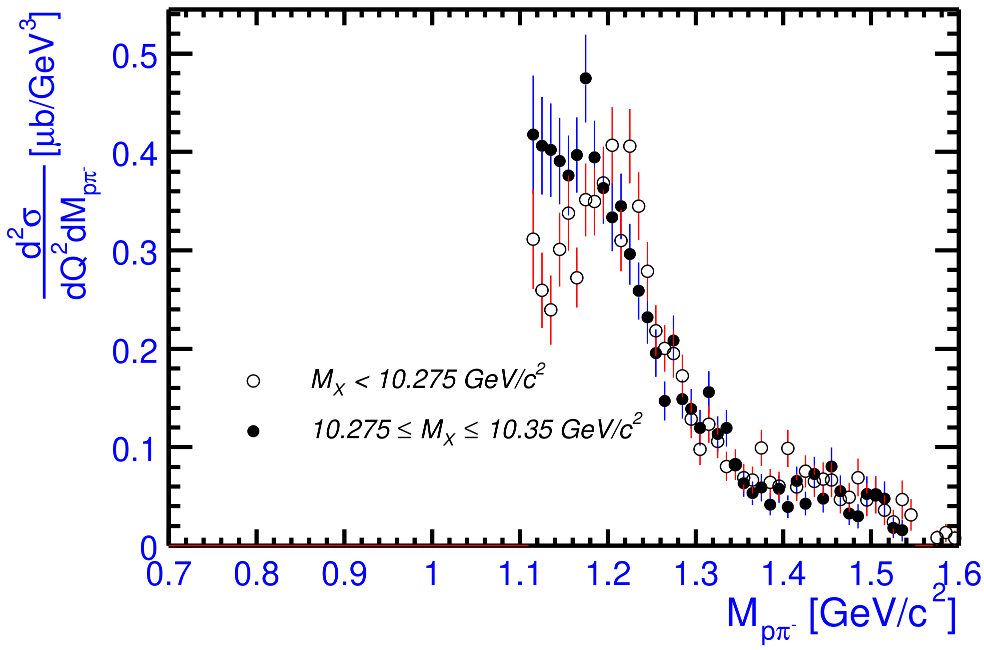

Figure 4.21: Comparison of exclusive cross sections for different missing mass

4.8.1 Exclusive Channel $^{12}C\left(e,e'p\pi^-\right)^{11}C$

Two methods were used to fit the cross sections as a decreasing contribution from the $N^*(1440)$ resonance was noted (see section 5.3). These are summarised below.

Method 1 Two Breit Wigner functions were fitted: the first parameterised the Δ peak and the second parameterised the $N^*(1440)$ resonance.
This was fitted in the range $0.175 \leq Q^2 \leq 0.275\ (GeV/c)^2$.

Method 2 One Breit Wigner function was fitted that parameterised the Δ resonance. The $M_{p\pi^-}$ spectra were fitted in the range $0.325 \leq Q^2 \leq 0.525\ (GeV/c)^2$. In the case of the W spectra, the range of Q^2 fitted was $0.325 \leq Q^2 \leq 0.425\ (GeV/c)^2$.

4.8.2 Semi Inclusive Channel $^{12}C\left(e,e'\pi^-\right)X$

Again, two methods were used to fit the cross sections and are summarised below.

Method 1 Two Breit Wigner functions and a quadratic background were fitted. The first Breit Wigner parameterised the Δ resonance and the second parameterised the $N^*(1440)$ resonance. Several functions were tried to estimate the background contribution. The “qfs” code [62] predicts that tails from higher resonances contribute to the cross section around the Δ peak. Initially, two Breit Wigner functions and a quadratic function were used to estimate the contribution of higher resonances and non-resonant pion production. This was unsuccessful since there was no data to constrain the fit in the higher resonance regions (see figures 5.5 and 5.6). A simpler approach was adopted by approximating these contributions by a quadratic function only.
This function was fitted in the range $0.1875 \leq Q^2 \leq 0.2625\ (GeV/c)^2$.

Method 2 One Breit Wigner function and a quadratic background were fitted. The Breit Wigner parameterised the Δ resonance and the quadratic parameterised the background contribution (as discussed above).
This method was used to fit the range $0.2875 \leq Q^2 \leq 0.3625\ (GeV/c)^2$.

4.8.3 Inclusive Channel $^{12}C\left(e,e'\right)X$

In this case only one fitting technique was employed. A Gaussian, two Breit Wigner and two background functions were fitted. The Gaussian parameterised the quasi elastic scattering contribution. The first Breit Wigner, in conjunction with the first background function (a quadratic), parameterised the Δ resonance and the second, combined with the other background function (linear), parameterised the two nucleon knockout portion of the inclusive cross section.

This fit was used in the range $0.1875 \leq Q^2 \leq 0.3875\ (GeV/c)^2$.

Chapter 5

Results and Discussion

As discussed in section 1.4, most previous electroexcitation measurements used inclusive scattering to probe the properties of the nuclear constituents. The near 4π acceptance detector CLAS at the Thomas Jefferson National Accelerator Facility enables the full detection of multi particle final states. This allowed inclusive, semi inclusive and exclusive measurements to be made allowing comparison with, and extension of, the results of [3].

Figure 5.1 shows how this type of experiment can be used to build a picture of the contributing reaction mechanisms to the inclusive scattering cross section. By requiring different final states, specific reaction processes are extracted from the inclusive cross section allowing their properties to be studied in the nuclear medium. In figure 5.1, the red plot is the measured inclusive cross section. The blue plot is the semi inclusive cross section where the detection of a π^- is also required. The exclusive cross section is shown in green.

5.1 Inclusive $d^2\sigma/dQ^2dW$ Results

The cross sections $d^2\sigma/dQ^2dW$ as a function of W for the inclusive process, calculated as described in section 4.6, are shown in figures 5.2 and 5.3. The data points are the results of this measurement and the error bars shown are statistical. On these plots the fits described in section 4.8.3 are also shown. The fit used in this case models the quasi elastic peak (red), the Δ peak (green), two nucleon interactions (+ background) (blue) and the sum of tails from higher resonances and non resonant pion production (magenta).

The two main features of an inclusive measurement are reproduced. The quasi elastic peak is most prominent with a peak position between 0.9 and 1.0 GeV/c^2 and the Δ peak is observed at higher W. The magnitude of the cross section decreases from $39.504 \pm 4.465\,\mu b/GeV^3$ at $Q^2 = 0.1875\ (GeV/c)^2$ to $19.632 \pm 0.953\,\mu b/GeV^3$ at

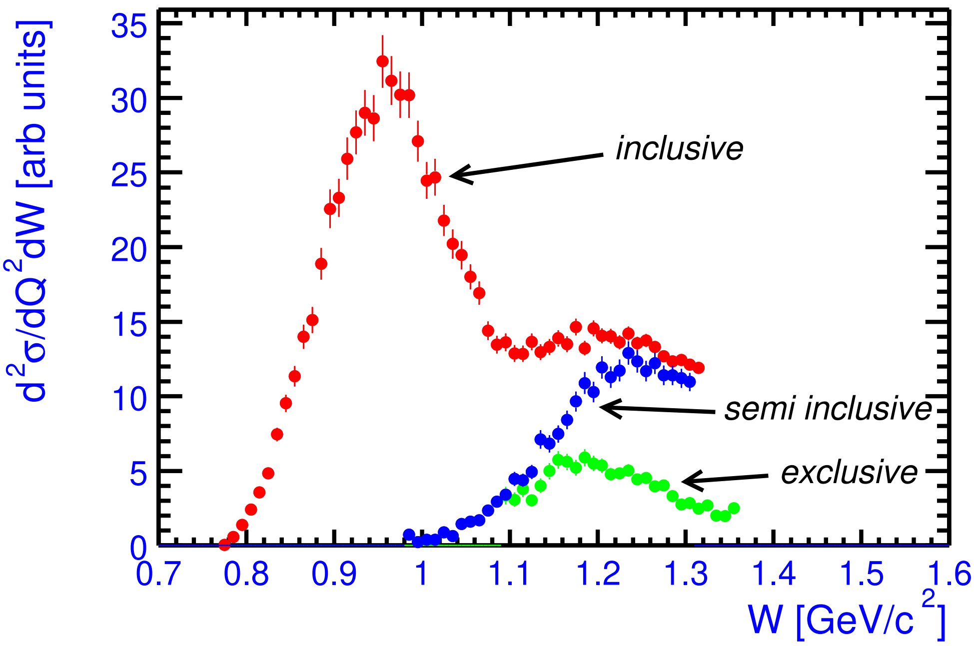

Figure 5.1: The full detection of multi particle final states allows inclusive, semi inclusive, and exclusive measurements to be performed which can then be used to build a picture of the competing reaction mechanisms that comprise the inclusive scattering cross section. The red plot is the inclusive scattering cross section, the blue is the semi inclusive, and the green is the exclusive cross section. These particular cross sections were measured at $Q^2 = 0.2875\ (GeV/c)^2$. The semi inclusive and exclusive cross sections were scaled in order to be displayed on the same axes.

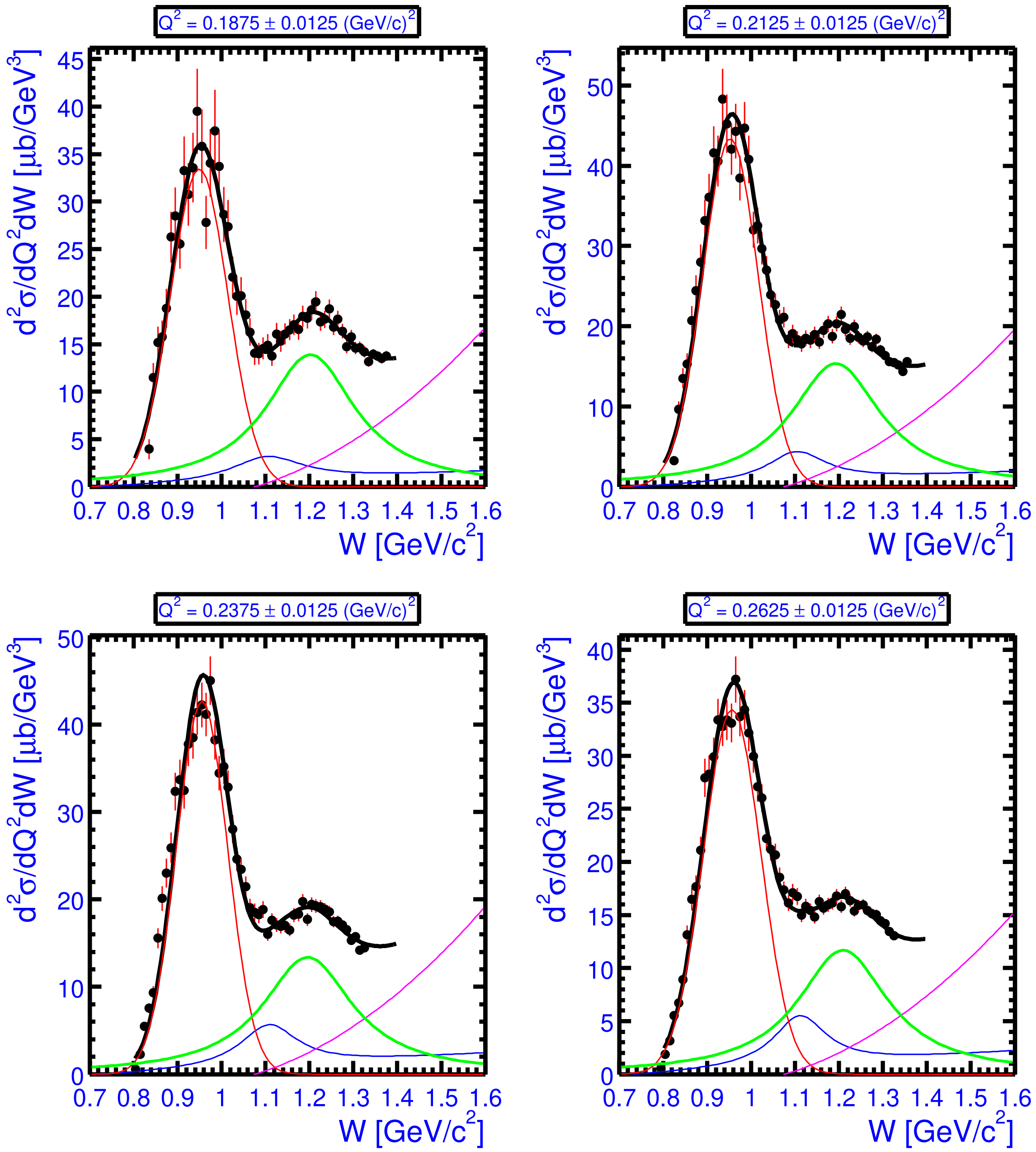

Figure 5.2: Inclusive cross sections $d^2\sigma/dQ^2dW$ for $0.1875 \leq Q^2 \leq 0.2625$ $(GeV/c)^2$. Data points are the results of this measurement. The error bars shown are statistical. The black line is the sum of the modelled reaction mechanisms. The coloured lines are the estimated contributions to the cross sections from each modelled channel: green - Δ production; magenta - sum of background processes (higher resonance tails and non resonant pion production); red - quasi elastic; blue - two body processes (+ background).

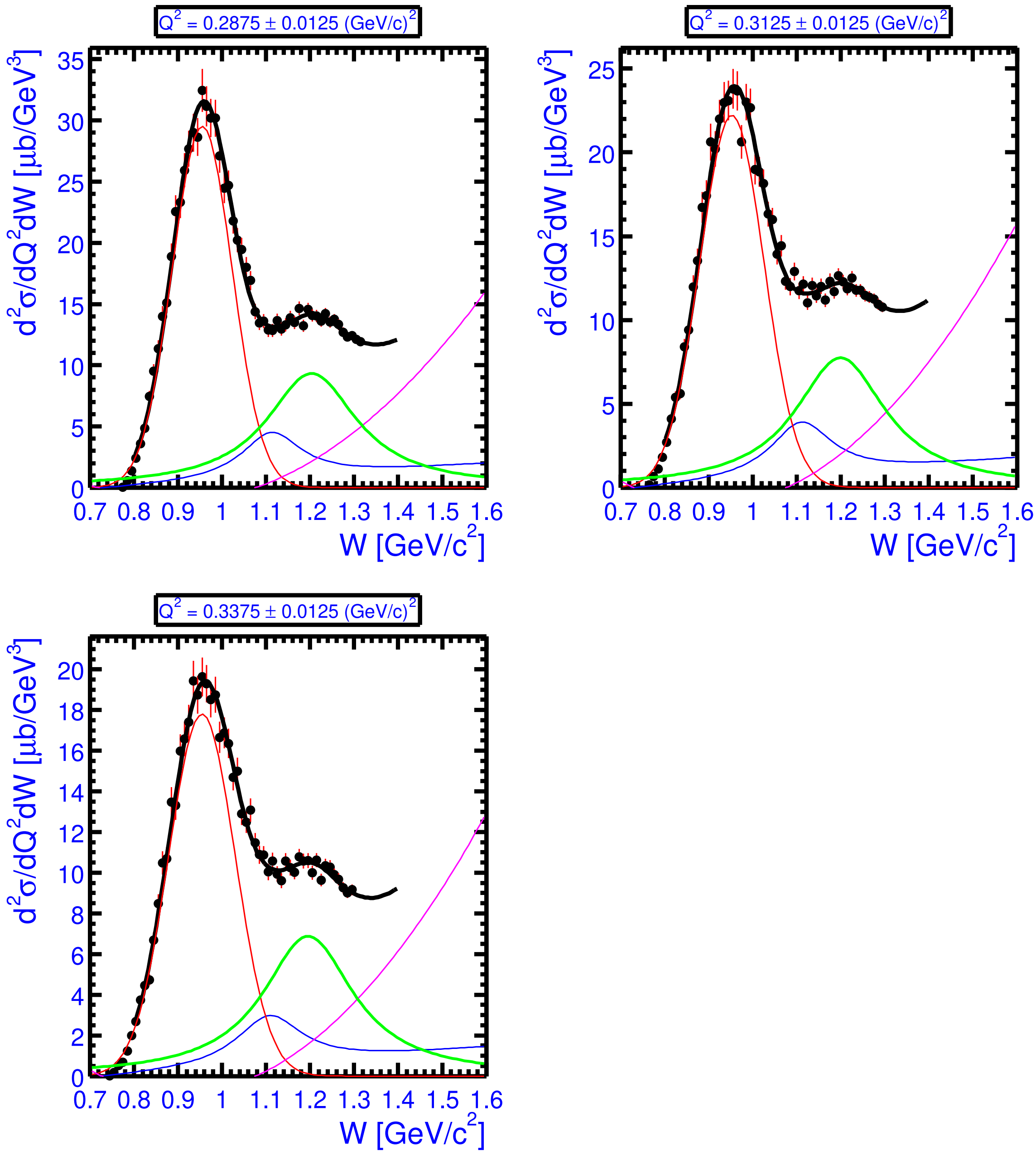

Figure 5.3: Inclusive cross sections $d^2\sigma/dQ^2dW$ for $0.2875 \leq Q^2 \leq 0.3375$ $(GeV/c)^2$. Data points are the results of this measurement. The error bars shown are statistical. The black line is the sum of the modelled reaction mechanisms. The coloured lines are the estimated contributions to the cross sections from each modelled channel: green - Δ production; magenta - sum of background processes (higher resonance tails and non resonant pion production); red - quasi elastic; blue - two body processes (+ background).

Q^2 $[GeV/c^2]$	Δ Peak Centroid $[GeV/c^2]$	Quasi Elastic Peak Centroid $[GeV/c^2]$	χ^2/N
0.1875 ± 0.0125	1.202 ± 0.003	0.949 ± 0.002	$48.635/41\,(= 1.186)$
0.2125 ± 0.0125	1.193 ± 0.001	0.953 ± 0.001	$92.729/40\,(= 2.318)$
0.2375 ± 0.0125	1.196 ± 0.001	0.956 ± 0.001	$248.048/39\,(= 6.360)$
0.2625 ± 0.0125	1.209 ± 0.001	0.957 ± 0.001	$83.808/39\,(= 2.149)$
0.2875 ± 0.0125	1.204 ± 0.001	0.955 ± 0.001	$45.743/38\,(= 1.204)$
0.3125 ± 0.0125	1.200 ± 0.004	0.953 ± 0.001	$52.491/36\,(= 1.458)$
0.3375 ± 0.0125	1.196 ± 0.002	0.955 ± 0.001	$47.363/36\,(= 1.316)$

Table 5.1: Peak positions and fit statistics for the fit to the cross section $d^2\sigma/dQ^2dW$ for inclusive events. The errors in the peak positions are from the fit.

$Q^2 = 0.3375\ (GeV/c)^2$ at the quasi elastic peak and from $16.046 \pm 1.177\,\mu b/GeV^3$ at $Q^2 = 0.1875\ (GeV/c)^2$ to $10.574 \pm 0.414\,\mu b/GeV^3$ at $Q^2 = 0.3375\ (GeV/c)^2$ at the Δ peak. This shows both that the size of the cross section decreases as Q^2 increases and that the contribution of the Δ and higher energy resonances to the inclusive cross section increases with respect to the quasi elastic reaction as Q^2 increases. A Gaussian gives a good fit to the quasi elastic peak at all Q^2. The quasi elastic peak positions do not show any Q^2 dependence but vary around a mean position of $W = 0.954\,GeV/c^2$. The decrease in contribution of the two body channel (blue) with increasing Q^2 as reported in [34–36] is not reproduced. The starting parameters for this fit are taken from the qfs computer program [62] (see section 4.8) and this introduces a dependency on the model which could account for the difference. Above $Q^2 = 0.3375\ (GeV/c)^2$, the contribution of background processes to the Δ peak is more than 50% and therefore no further peak extraction was performed.

Table 5.1 summarises the results of the fitting procedure. The resulting Δ peak positions are shown in figure 5.4. The results of Sealock *et al.* [3] are also shown for comparison. In both measurements, the qfs code was used to obtain an estimation of the background contributions to the Δ signal which affect the measured Δ peak position (see section 4.8). The measured Δ masses from the present measurement are between 30 and $60\,MeV$ lower than those from [3] and the clear Q^2 dependence is not reproduced. The present measurement covered a smaller range of W than that of Sealock *et al.* (up to $100\,MeV/c^2$ less) so it was harder to constrain the higher resonance tails which affected the measured Δ peak position and may account for the difference.

No simple Q^2 dependence of the Δ mass is observed in the present inclusive measurement. The blue line in figure 5.4 is the result of fitting a constant to the peak positions, i.e. no Q^2 dependence, and the magenta line is the result of fitting a linear function. Neither fit gives a satisfactory representation of the data.

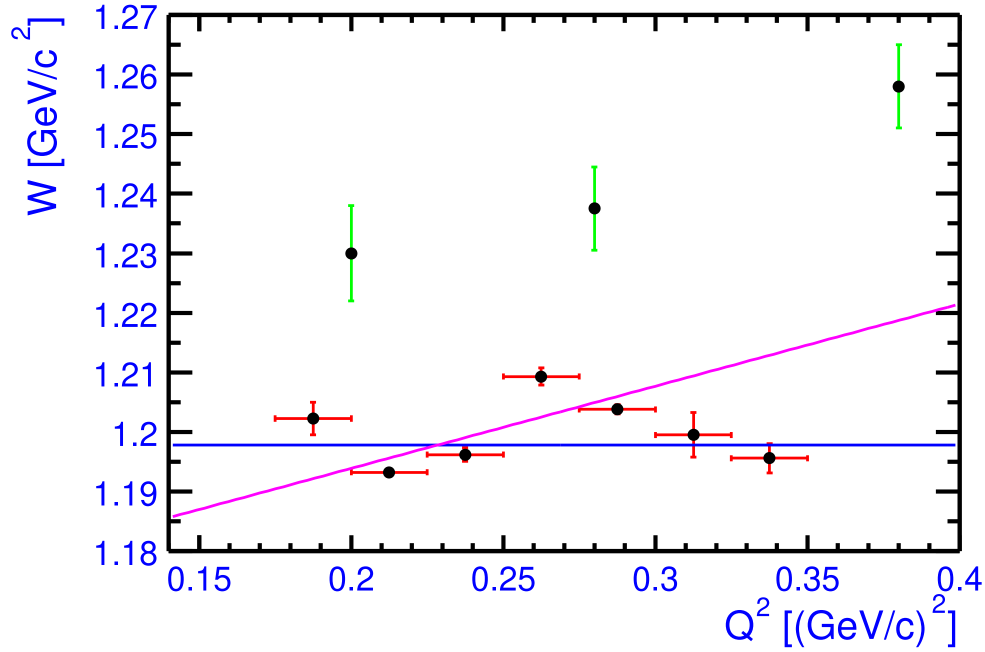

Figure 5.4: Δ peak positions extracted from the inclusive analysis as a function of Q^2 (red). The errors in W are the errors returned by the fit. The blue line is the result of fitting a constant to the peak positions. The magenta line is the result of fitting a linear function to the peak positions. The results from [3] are shown for comparison (green).

Q^2 $[GeV/c^2]$	Δ Peak Centroid $[GeV/c^2]$	χ^2/N
0.1875 ± 0.0125	1.250 ± 0.003	$220.469/25\,(= 8.819)$
0.2125 ± 0.0125	1.241 ± 0.003	$225.980/23\,(= 9.825)$
0.2375 ± 0.0125	1.247 ± 0.003	$234.857/25\,(= 9.394)$
0.2625 ± 0.0125	1.243 ± 0.002	$164.511/25\,(= 6.580)$
0.2875 ± 0.0125	1.234 ± 0.002	$142.245/25\,(= 5.690)$
0.3125 ± 0.0125	1.240 ± 0.003	$108.442/26\,(= 4.171)$

Table 5.2: Peak positions and fit statistics for the fit to the cross section $d^2\sigma/dQ^2dW$ filtered on semi inclusive events. The errors in the peak positions are from the fit.

5.2 Semi Inclusive $d^2\sigma/dQ^2dW$ Results

The cross sections $d^2\sigma/dQ^2dW$ as a function of W for the semi inclusive analysis, as described in sections 4.3 and 4.6, are shown in figures 5.5 and 5.6. The data points are the results of this measurement and the error bars shown are statistical. On these plots the fits described in section 4.8.2 are also shown. The fit used in this case models the Δ peak (green) and contributions from non resonant and higher resonant production (red). Two body processes are considered up to $Q^2 = 0.2625\ (GeV/c)^2$.

The required detection of a π^- removes the quasi elastic peak from the excitation spectrum. The magnitude of the cross section decreases from $1.707 \pm 0.135\,\mu b/GeV^3$ at $Q^2 = 0.1875\ (GeV/c)^2$ to $1.056 \pm 0.062\,\mu b/GeV^3$ at $Q^2 = 0.3125\ (GeV/c)^2$ at the Δ peak. This decrease is not as large as that observed in the inclusive case. There is a peak at around $W = 1.285\,GeV/c^2$ but it does not show a resonant structure since there is still contamination from background reactions.

The results of the fitting procedure are listed in table 5.2. The result of the non-resonant structure and choice of fit function is that the cross section is not well fitted: the values of χ^2/N for the fits range from 4.171 to 9.825. The background function does not correctly estimate the contribution of other processes.

There is a notable shift in the mass of the Δ to higher W from around $1.2\,GeV/c^2$ in the inclusive measurement to around $1.24\,GeV/c^2$ in the semi inclusive. It is impossible to determine whether this is an effect of the physics or of the fitting procedure since the fits are not reliable in the semi inclusive measurement. The resulting Δ peak positions are shown in figure 5.7 where the blue line is the result of fitting a constant to the peak positions, i.e. no Q^2 dependence, and the magenta line is the result of fitting a linear function. The linear fit appears to give a good representation of the data but again, it is impossible to determine whether this is a true physics effect or as a result of the unreliable fitting procedure as discussed above.

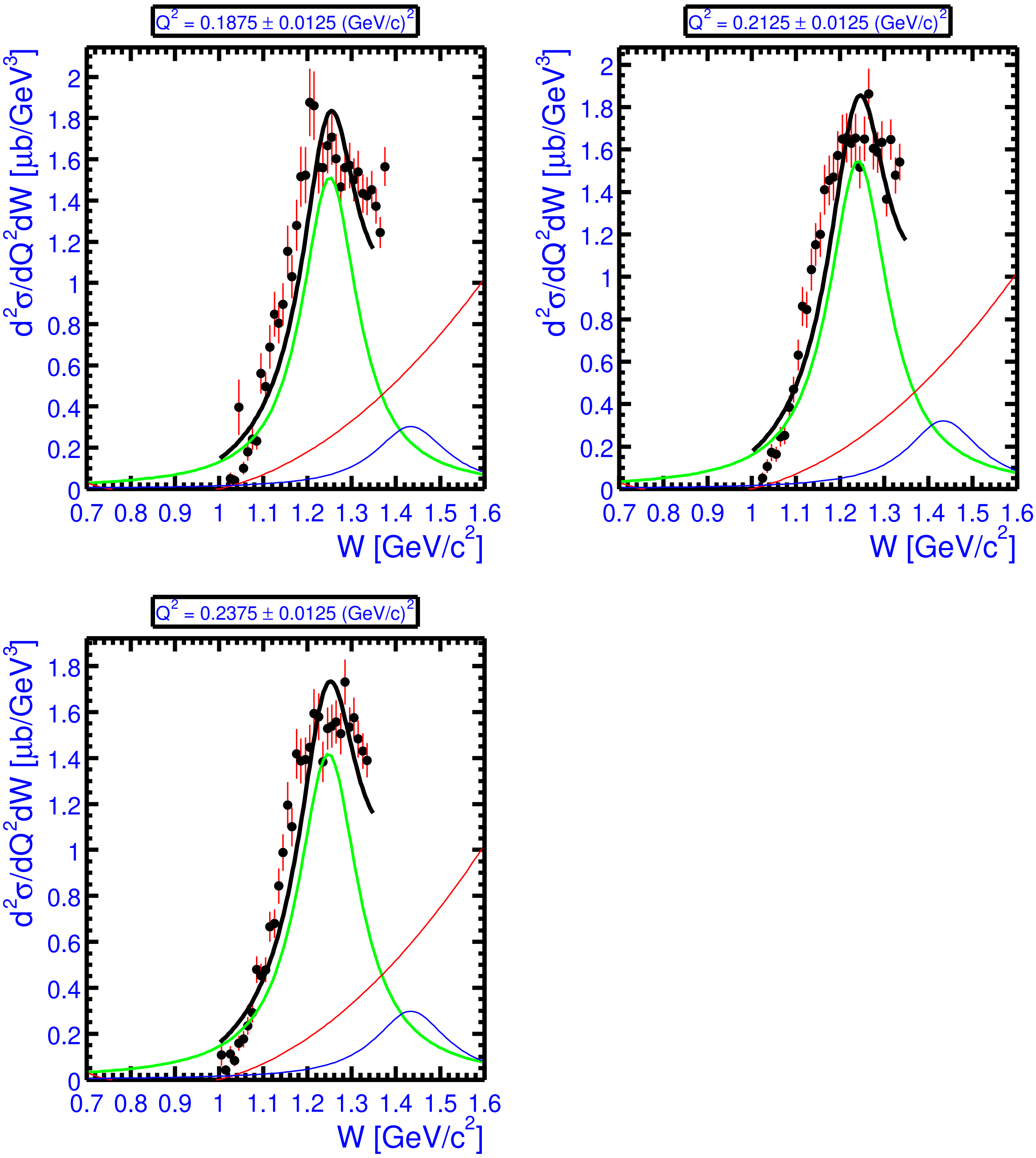

Figure 5.5: Semi inclusive cross sections $d^2\sigma/dQ^2dW$ for $0.1875 \leq Q^2 \leq 0.2375\ (GeV/c)^2$. Data points are the results of this measurement. The error bars shown are statistical. The black line is the sum of the modelled reaction mechanisms. The coloured lines are the estimated contributions to the cross sections from each modelled channel: green - Δ production; blue - two body processes; red - background.

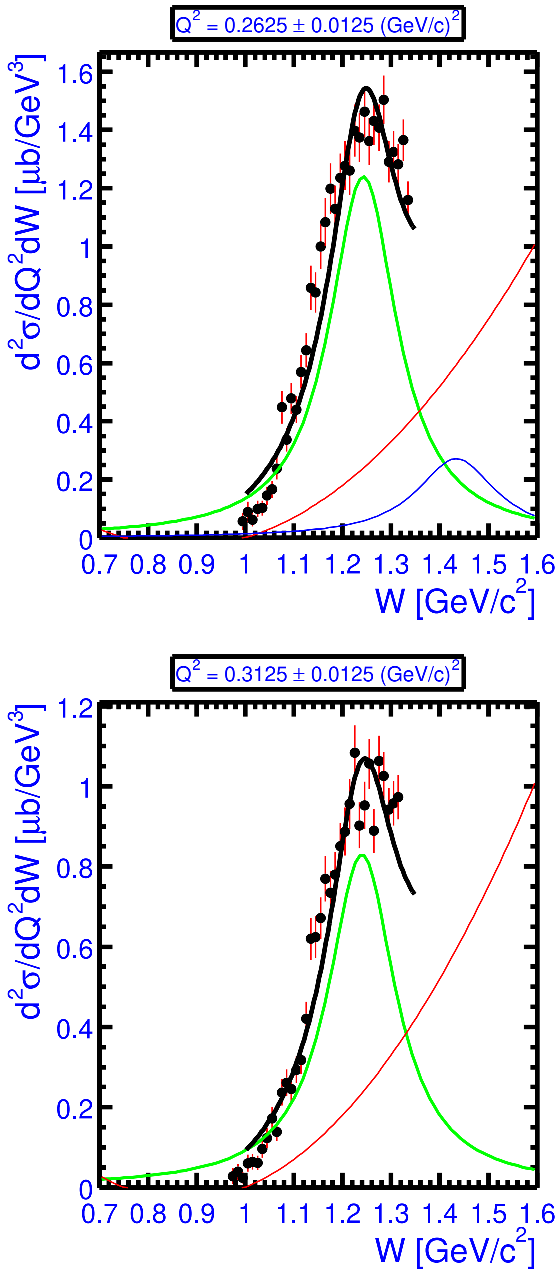

Figure 5.6: Semi inclusive cross sections $d^2\sigma/dQ^2dW$ for $0.2625 \leq Q^2 \leq 0.3125\ (GeV/c)^2$. Data points are the results of this measurement. The error bars shown are statistical. The black line is the sum of the modelled reaction mechanisms. The coloured lines are the estimated contributions to the cross sections from each modelled channel: green - Δ production; blue - two body processes; red - background. (The two body processes were only fitted up to $Q^2 = 0.2625\ (GeV/c)^2$)

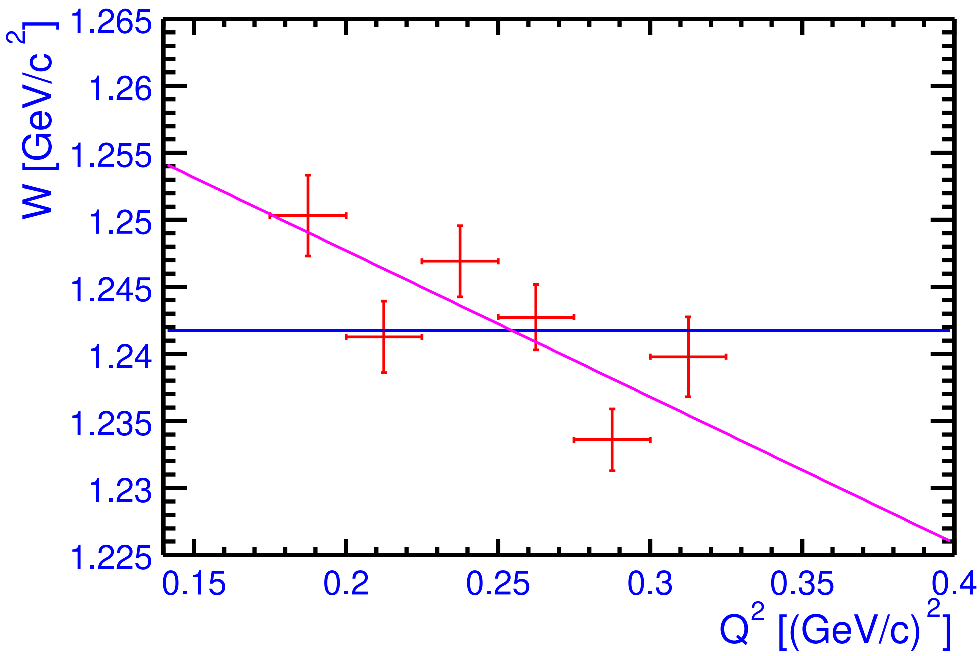

Figure 5.7: Δ peak positions extracted from the semi inclusive analysis as a function of Q^2. The errors in W are the errors returned by the fit. The blue line is the result of fitting a constant to the peak positions. The magenta line is the result of fitting a linear function to the peak positions.

Q^2 $[GeV/c^2]$	Δ Peak Centroid $[GeV/c^2]$	χ^2/N
0.225 ± 0.025	1.187 ± 0.005	$23.847/22\,(= 1.084)$
0.275 ± 0.025	1.193 ± 0.003	$22.705/21\,(= 1.081)$
0.325 ± 0.025	1.200 ± 0.004	$25.879/23\,(= 1.125)$
0.375 ± 0.025	1.199 ± 0.005	$36.835/21\,(= 1.754)$
0.425 ± 0.025	1.197 ± 0.004	$18.889/23\,(= 0.821)$

Table 5.3: Peak positions and fit statistics for the fit to the cross section $d^2\sigma/dQ^2dW$ filtered on exclusive events. The errors in the peak positions are from the fit.

5.3 Exclusive Results

The exclusive analysis was divided into two cases (see sections 4.3 and 4.6). Firstly, the results of the analysis using only the scattered electron are discussed followed by the discussion of the exclusive analysis using all three final state particles.

5.3.1 Exclusive $d^2\sigma/dQ^2dW$ Results

The cross sections $d^2\sigma/dQ^2dW$, described in sections 4.3 and 4.6, as a function of W are shown in figures 5.8 and 5.9. The data points are the results of this measurement and the error bars are statistical. On these plots the fits described in section 4.8.1 are also shown. The fit used in this case models the Δ peak (green) and at low Q^2 $(0.225 \leq Q^2 \leq 0.275\,GeV/c^2)$ adds a contribution from the $N^*\,(1440)$ resonance (blue).

Restricting the reaction to ${}^{12}C\,(e, e'p\pi^-)^{11}\,C$ results in the cross section showing the classical resonance shape. This suggests that a background contribution affected the Δ signal in the semi inclusive results. The cross sections are approximately half the size of the semi inclusive cross sections. The magnitude of the cross section decreases from $0.803 \pm 0.081\,\mu b/GeV^3$ at $Q^2 = 0.225\,(GeV/c)^2$ to $0.158 \pm 0.021\,\mu b/GeV^3$ at $Q^2 = 0.425\,(GeV/c)^2$ at the Δ peak - faster than was noted for the semi inclusive case. This is attributed to the fact that as Q^2 increases higher resonances are more likely to be excited and these contaminate the semi inclusive cross section. These processes are discarded by detecting the complete final state.

As shown in table 5.3, the fits to these cross sections are much better than the fits for the inclusive and, particularly, the semi inclusive cross sections. The values of χ^2/N for these fits range from 0.821 to 1.754. The Δ peak positions are shown in figure 5.10 where the blue line is the result of fitting a constant to the peak positions, i.e. no Q^2 dependence, and the magenta line is the result of fitting a linear function. The linear fit gives the better representation of the data indicating a Q^2 dependence of the Δ mass in the nucleus. The results presented here probably do reflect the physics involved in the reaction since the fits used to obtain the Δ mass are relatively simple

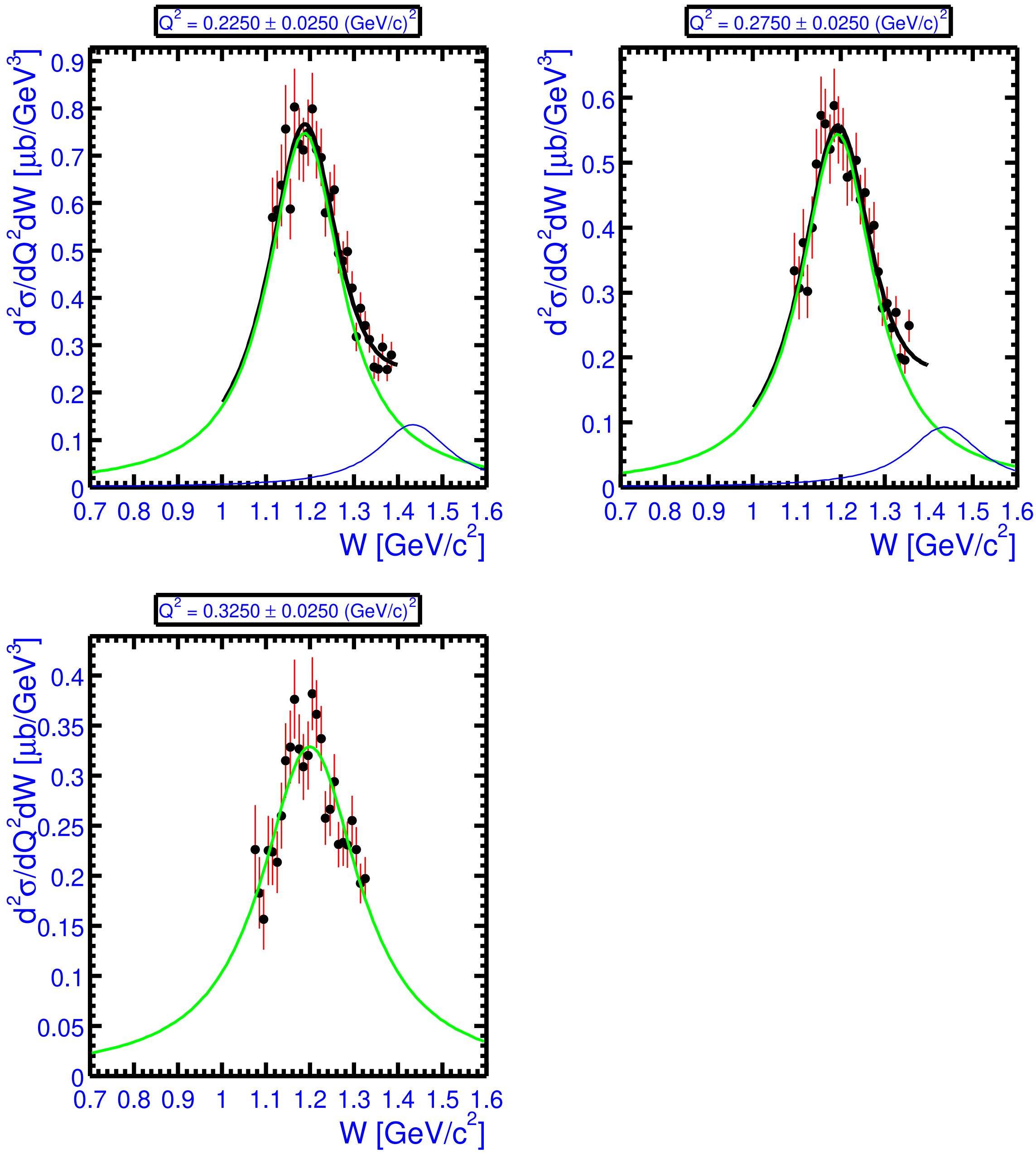

Figure 5.8: Exclusive cross sections $d^2\sigma/dQ^2dW$ for $0.225 \leq Q^2 \leq 0.325\ (GeV/c)^2$. Data points are the results of this measurement. The error bars shown are statistical. The black line (where shown) is the sum of the modelled reaction mechanisms. The coloured lines are the estimated contributions to the cross sections from each modelled channel: green - Δ production; blue - two body processes. (The two body processes were only fitted up to $Q^2 = 0.275\ (GeV/c)^2$)

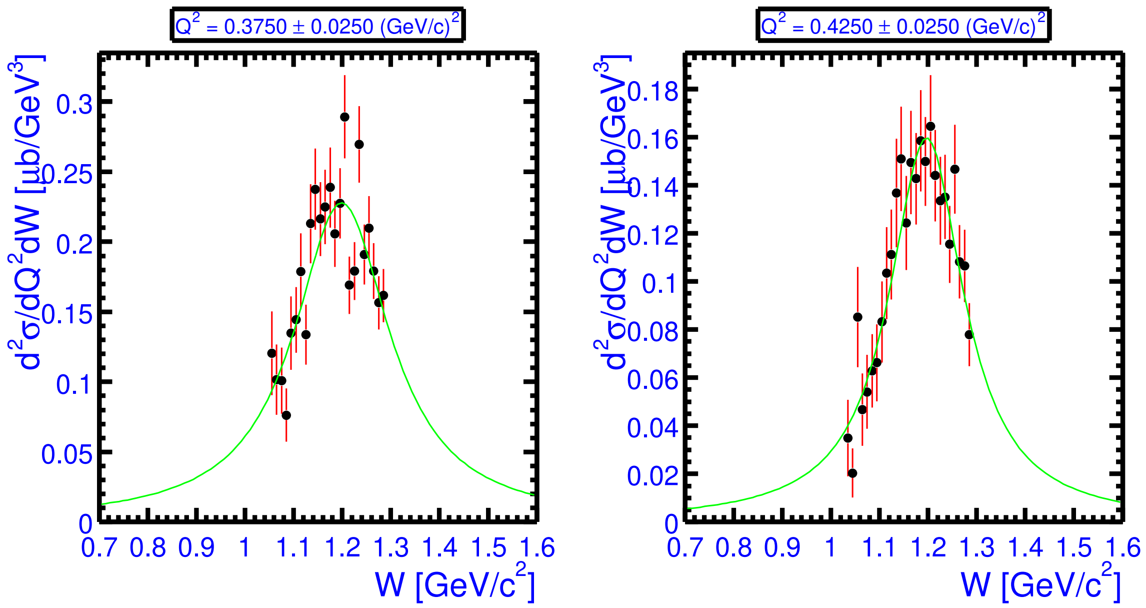

Figure 5.9: Exclusive cross sections $d^2\sigma/dQ^2dW$ for $0.375 \leq Q^2 \leq 0.425\ (GeV/c)^2$. Data points are the results of this measurement. The error bars shown are statistical. The coloured line (green) is the estimated Δ production contribution.

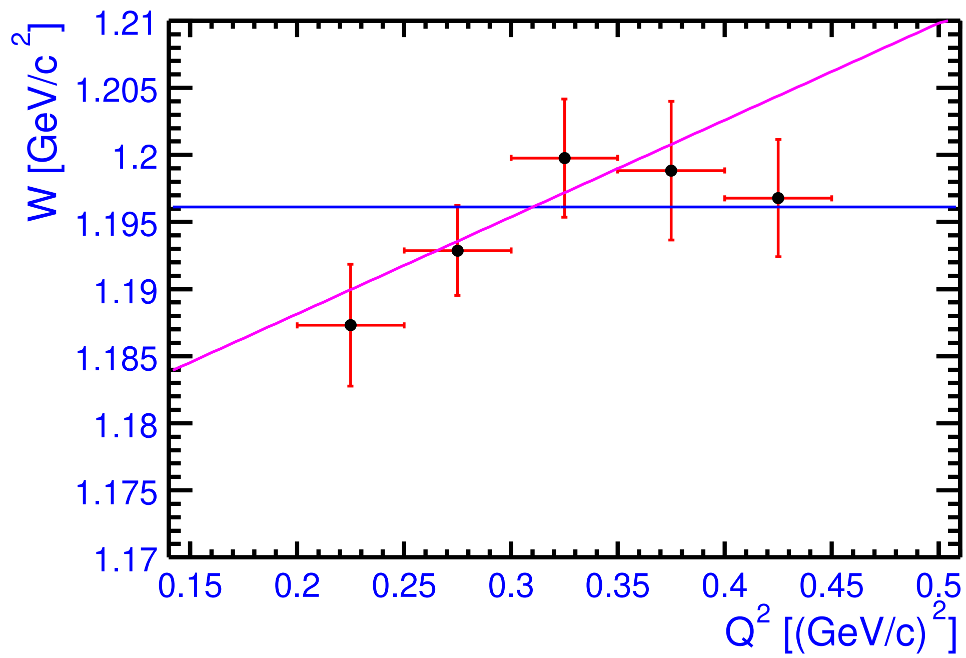

Figure 5.10: Δ peak positions extracted from the exclusive analysis as a function of Q^2. Only the scattered electron was used for this analysis. The errors in W are the errors returned by the fit. The blue line is the result of fitting a constant to the peak positions. The magenta line is the result of fitting a linear function to the peak positions.

Q^2 $[GeV/c^2]$	Δ Peak Centroid $[GeV/c^2]$	χ^2/N
0.175 ± 0.025	1.186 ± 0.004	$40.751/35\,(= 1.164)$
0.225 ± 0.025	1.181 ± 0.005	$48.188/35\,(= 1.377)$
0.275 ± 0.025	1.184 ± 0.004	$31.965/35\,(= 0.913)$
0.325 ± 0.025	1.178 ± 0.005	$39.289/19\,(= 2.068)$
0.375 ± 0.025	1.180 ± 0.005	$18.070/19\,(= 0.951)$
0.425 ± 0.025	1.188 ± 0.004	$18.032/19\,(= 0.949)$
0.475 ± 0.025	1.187 ± 0.005	$22.057/19\,(= 1.161)$

Table 5.4: Peak positions and fit statistics for the fit to the cross section $d^2\sigma/dQ^2dM_{p\pi^-}$ filtered on exclusive events. The errors in the peak positions are from the fit.

and all return χ^2/N around 1 as discussed above.

5.3.2 Exclusive $d^2\sigma/dQ^2dM_{p\pi^-}$ Results

The cross sections $d^2\sigma/dQ^2dM_{p\pi^-}$, described in sections 4.3 and 4.6, as a function of $M_{p\pi^-}$ are shown in figures 5.11 and 5.12. The data points are the results of this measurement and the error bars are statistical. On these plots the fits described in section 4.8.1 are also shown. The fit used in this case models the Δ peak (green) and at low Q^2 ($0.175 \leq Q^2 \leq 0.275\,GeV/c^2$) adds a contribution from the $N^*\,(1440)$ resonance (blue).

The shape of the cross section exhibits a resonant structure indicating that most of the background contamination has been removed. The magnitude of the cross section decreases from $0.633{\pm}0.070\,\mu b/GeV^3$ at $Q^2 = 0.175\ (GeV/c)^2$ to $0.162{\pm}0.023\,\mu b/GeV^3$ at $Q^2 = 0.475\ (GeV/c)^2$ at the Δ peak.

Table 5.4 shows that the fitted functions provide a good fit to the cross section as the values of χ^2/N for the fits range from 0.913 to 2.068. The resulting peak positions as a function of Q^2 are shown in figure 5.13 where the blue line is the result of fitting a constant to the peak positions, i.e. no Q^2 dependence, and the magenta line is the result of fitting a linear function. As for the exclusive cross section $d^2\sigma/dQ^2dW$, the linear fit gives the better representation of the data indicating a Q^2 dependence of the Δ mass in the nucleus. However, the gradient of the linear function is a factor of three smaller which indicates that the dependence is not as strong as that inferred from $d^2\sigma/dQ^2dW$. This is probably a more accurate reflection of the physics since obtaining the $d^2\sigma/dQ^2dM_{p\pi^-}$ cross section uses the decay particles of the Δ resonance and therefore has less contamination from background reactions. This is clearly demonstrated by comparing figure 5.12 with figure 5.8. The width of the Δ peak is significantly smaller in figure 5.12 and data is accepted to values of $M_{p\pi^-}$ up to $1.6\,GeV/c^2$ allowing background contributions to be constrained.

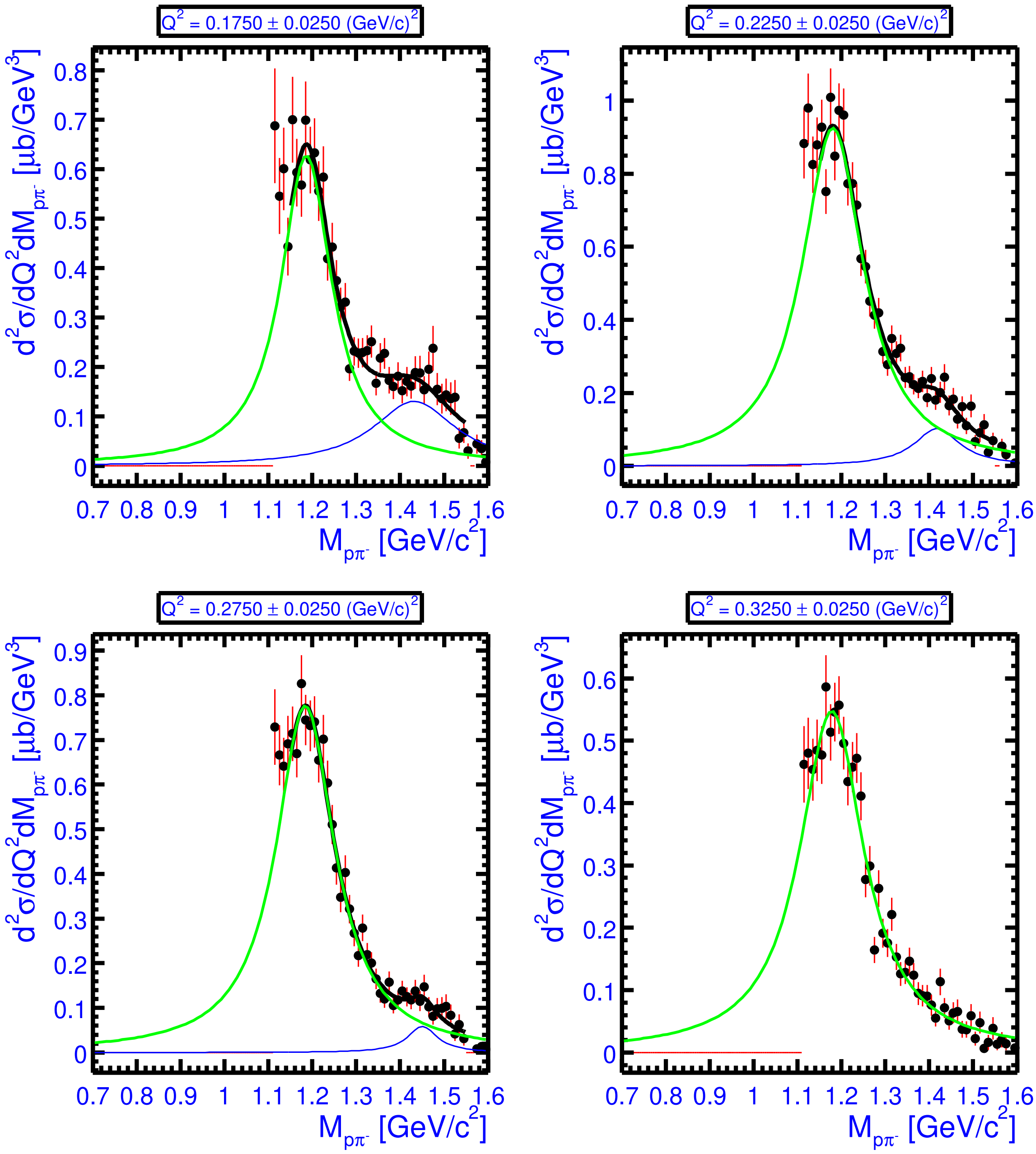

Figure 5.11: Exclusive cross sections $d^2\sigma/dQ^2dM_{p\pi^-}$ for $0.175 \leq Q^2 \leq 0.325$ $(GeV/c)^2$. Data points are the results of this measurement. The error bars shown are statistical. The black line (where shown) is the sum of the modelled reaction mechanisms. The coloured lines are the estimated contributions to the cross sections from each modelled channel: green - Δ production; blue - two body processes. (The two body processes were only fitted up to $Q^2 = 0.275$ $(GeV/c)^2$)

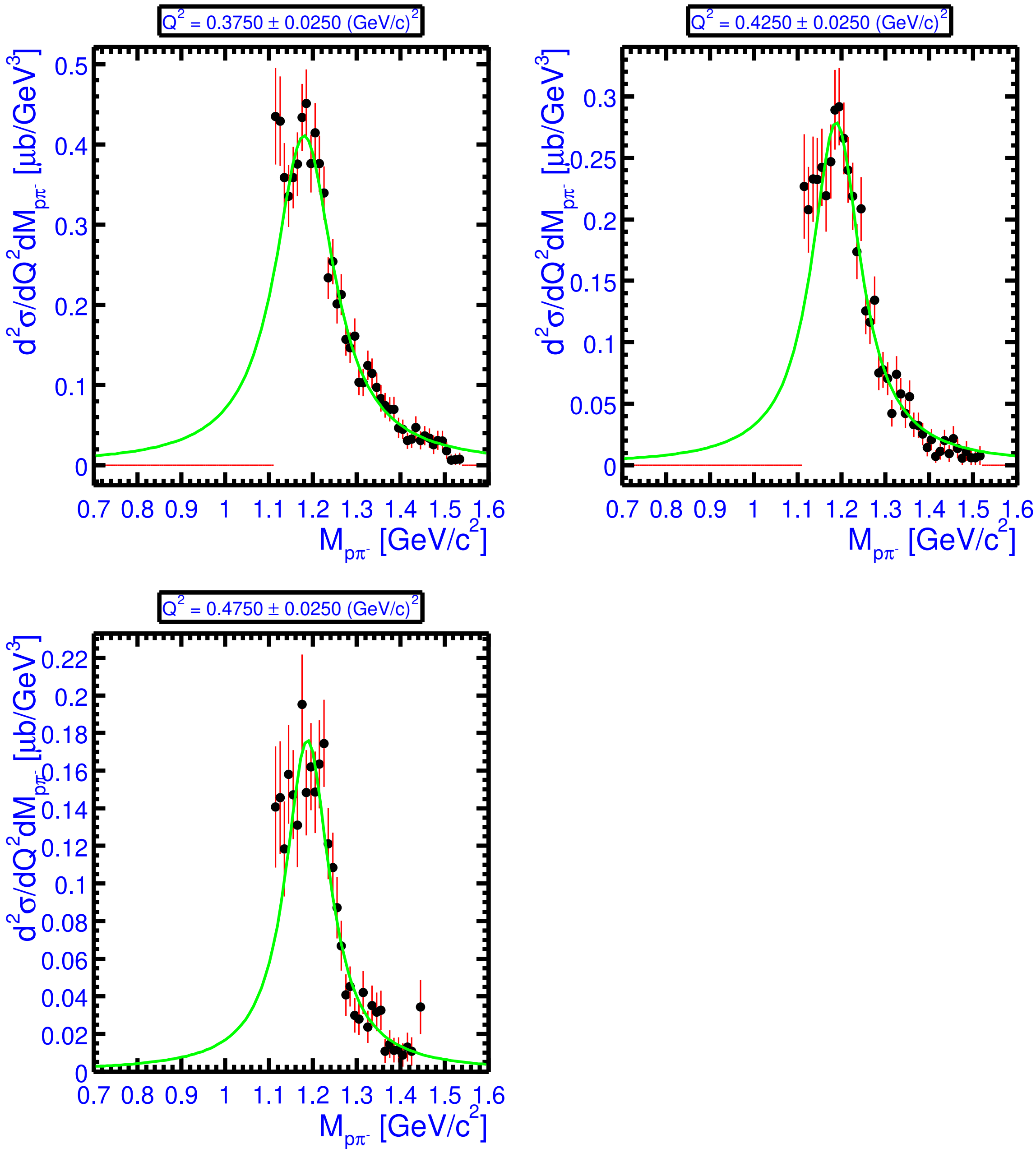

Figure 5.12: Exclusive cross sections $d^2\sigma/dQ^2dM_{p\pi^-}$ for $0.375 \leq Q^2 \leq 0.475$ $(GeV/c)^2$. Data points are the results of this measurement. The error bars shown are statistical. The coloured line (green) is the estimated Δ production contribution.

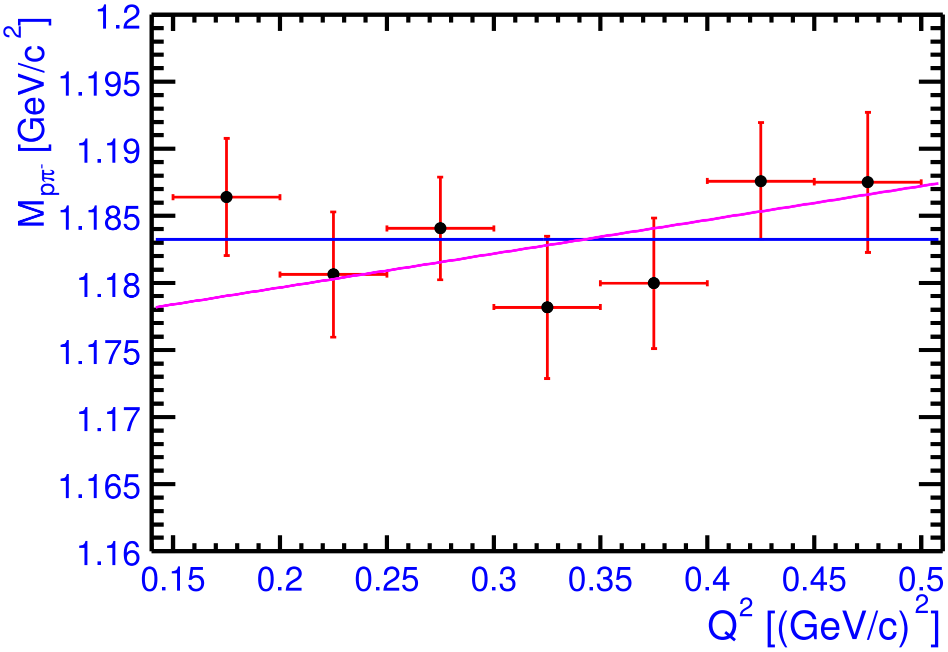

Figure 5.13: Δ peak positions extracted from the exclusive analysis as a function of Q^2. All final state particles were used for this analysis. The errors in W are the errors returned by the fit. The blue line is the result of fitting a constant to the peak positions. The magenta line is the result of fitting a linear function to the peak positions.

Chapter 6

Conclusion

The mass of the $\Delta\,(1232)$ resonance was studied by means of electron scattering on ^{12}C because a variation with momentum had been reported by Sealock *et al.* [3]. This implies that the potential the Δ experiences in the nucleus is dependent on its momentum, a property that is not observed for protons and neutrons in the nuclear medium [4]. Knowledge of the Δ-nucleus potential is vital to produce a complete theoretical description of the nucleus.

Most previous electroexcitation measurements in the Δ region, including those of Sealock *et al.* [3], were made using inclusive scattering due to the limitations of the available detector systems. Such measurements suffer from contamination from background contributions whose elimination depends on successfully modelling them. The near 4π acceptance detector CLAS at the Thomas Jefferson National Accelerator Facility enables the detection of the full reaction final state. Exclusive measurements were made allowing the isolation of the Δ production cross section using the reaction kinematics. However, as the experimental trigger for detecting an event was set to require that only an electron was detected, inclusive and semi inclusive measurements were also made allowing comparison with, and extension of, the results of [3].

The inclusive cross sections demonstrate the expected features: a prominent quasi elastic peak and a smaller Δ resonance peak. The magnitude of the cross section was observed to decrease with increasing Q^2 while the contribution of the Δ and other higher resonances with respect to the quasi elastic reaction was observed to increase.

The semi inclusive cross sections obtained for events where the scattered electron and a π^- were detected, contained no quasi elastic or two body interaction contributions as expected (see section 1.3.3). However, the non-resonant shape of the cross sections resulted in a failure to fit them satisfactorily. It is concluded that the model of the background processes was incorrect making extraction of the Δ peak unreliable.

Two types of exclusive analysis were performed, one using only the scattered electron and the other using all three final state particles. Both sets of cross sections demonstrated the classical resonance shape indicating that background contributions affected the Δ signal in the semi inclusive measurements.

The Q^2 dependence of the Δ mass reported by Sealock *et al.* [3] was not reproduced in the inclusive electron scattering measurements presented in this thesis. This was attributed to the present measurement covering a smaller range of W than that of Sealock *et al.* (up to 100 MeV/c^2 less) so it was harder to constrain the higher resonance tails which affect the measured Δ peak position. A dependence was not seen in the semi inclusive measurement either but was observed in the exclusive measurements due to the successful removal of background contributions.

Therefore, it is concluded that the Δ-nucleus potential does depend on the momentum of the Δ but this property was only observed when exclusive measurements were made and thus background contributions were removed. However, even for the $d^2\sigma/dQ^2dM_{p\pi^-}$ cross section that used the decay particles of the Δ resonance, background contributions were not completely removed. It is possible that a more accurate extraction of the Δ resonance yield will be obtained by examining the π^- centre of mass emission angle.

A more accurate measurement of the acceptance of the CLAS detector may be obtained by applying an unfolding technique based on Bayes theorem [63] currently under development in the Nuclear Physics Experimental Group [64].

No theoretical predictions of the reaction processes were available for comparison with the present measurements other than the basic qfs computer program. An obvious extension to this work is the inclusion of theoretical calculations.

Appendix A

Electron Identification Correction for e2a at 1.1GeV

A.1 Introduction

In electron scattering experiments accurate identification of the scattered electron is crucial. In CLAS events are recorded if a particle - the trigger particle - satisfies certain criteria that should define it as an electron. The trigger can be restricted further, for example instead of requiring just an electron, requiring a positive track also, but for the e2a run period the trigger was defined as simply an electron candidate. At run time these decisions are made quickly based on the limited detector information available.

The "cooking" stage of the analysis is where the detector information is turned into useful quantities like momentum, vertex position and particle id. At this stage there is a specific set of criteria that the trigger particle has to satisfy to be labelled an electron. If the particle passes these cuts then it is given an id of 11, otherwise it is given an id of 0. The difference between the id 0 and id 11 trigger particle events was studied and it was found that many of the "bad" events are perfectly good physics events and should not be discarded.

Figure A.1 shows the energy deposited in the electromagnetic calorimeter as a function of momentum for the two classes of trigger particle. There is a linear relationship between these two quantities and anything off this straight line should be discarded. It is noted that there is very little difference in these plots and that good events could be recovered.

A.2 Correction Method

The first stage in determining criteria that defined the trigger particle as an electron was to cut on the electron band discussed (see figure A.1). This was done by projecting

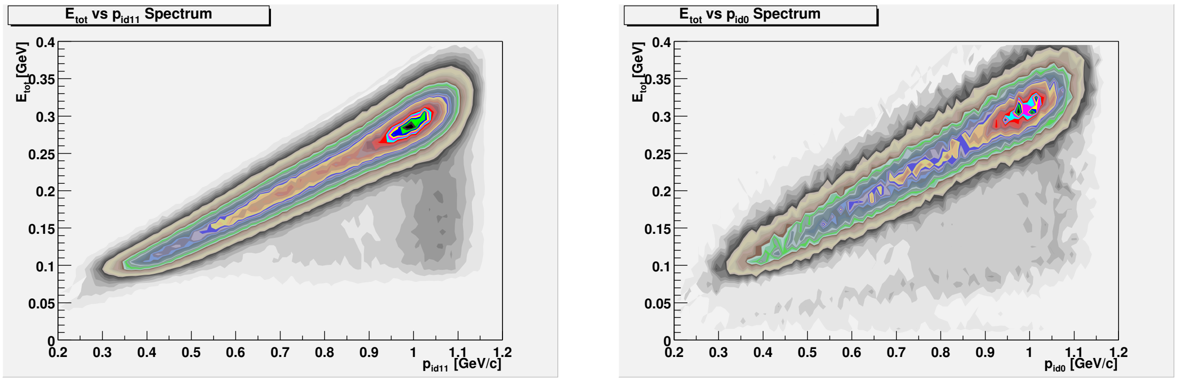

(a) Id 11 trigger particles

(b) Id 0 trigger particles

Figure A.1: Comparison of id 11 and id 0 trigger particles - energy deposited as a function of momentum

four bins in deposited energy, E_{tot}, onto the momentum axis and fitting a Gaussian to each (see figure A.2 for an example). The peak positions were fitted as a function of E_{tot} as were the peak widths. These fits are shown in figure A.3.

This enabled the definition of two lines that define the good electron band (see figure A.4). The form of the two straight lines defining the good electron band was changed so that E_{tot} was calculated as a function of $p_{e'}$ to conform to the method of application used in the e2a analysis code. However, more detector information could be used to clarify the identification of the trigger particle.

It was possible that π^-s could have been detected as electrons but the Cerenkov detector works well at this low energy at rejecting these contaminants.

The way in which the trigger particle deposited its energy in the calorimeter was also studied. The calorimeter is split into two separate detection systems - an inner and an outer layer. Electrons deposit more energy than pions in the inner layer (see figure A.5) so a cut was placed on the energy deposited in the inner layer specifying that electrons have to deposit more than $0.05\,GeV$.

A.3 Discussion

At low beam energies the electron detection efficiency is very good although this correction had to applied for completeness.

Figure A.6 shows a comparison of the edges of the electron band for the three beam energies used in e2a. These three should overlap if the detector responds identically over the whole momentum range and very good agreement is shown.

The results here verify that although the cooking software is very good, a little

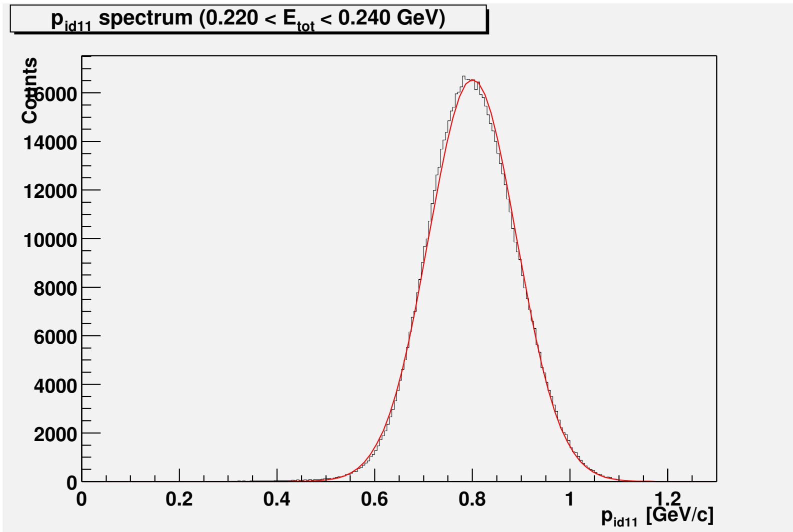

Figure A.2: Example of projection and fit of the main electron band

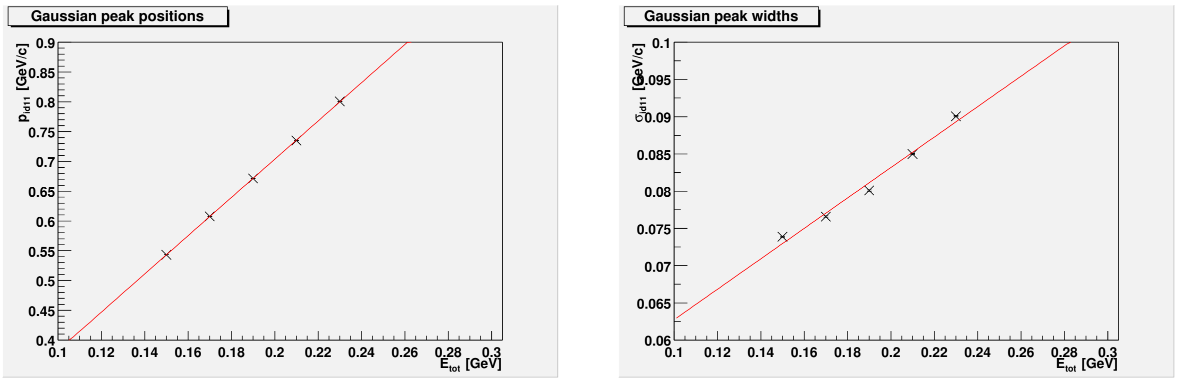

(a) Momentum peak position as a function of deposited energy

(b) Momentum peak width as a function of deposited energy

Figure A.3: Fits of peak positions and widths to define the main electron band

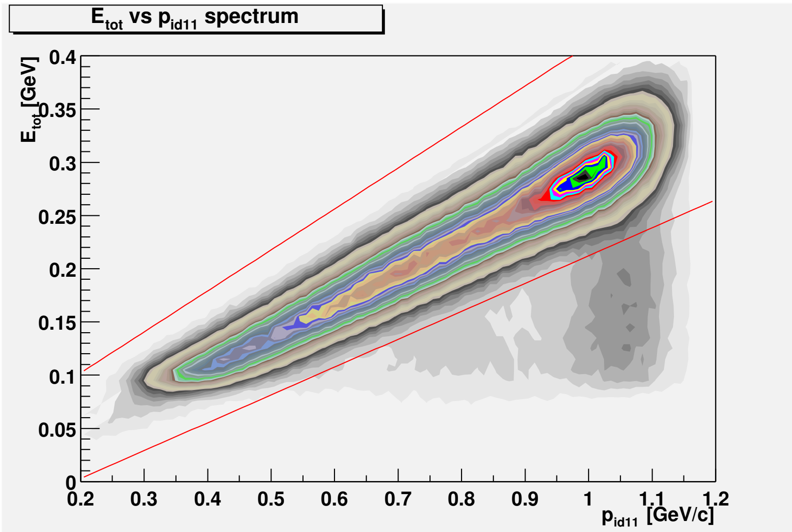

Figure A.4: Main electron band showing the cuts to be applied

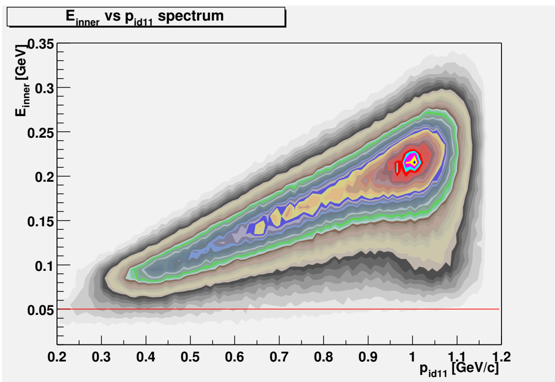

(a) Inner energy deposition as a function of momentum for electrons

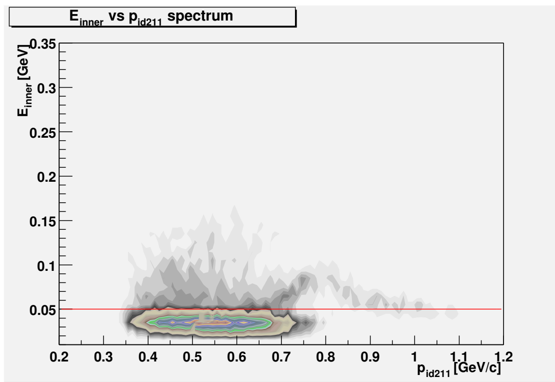

(b) Inner energy deposition as a function of momentum for π^+s

Figure A.5: Comparison of energy deposited in the inner calorimeter layer by electrons and π^+s. The applied cut is shown in red.

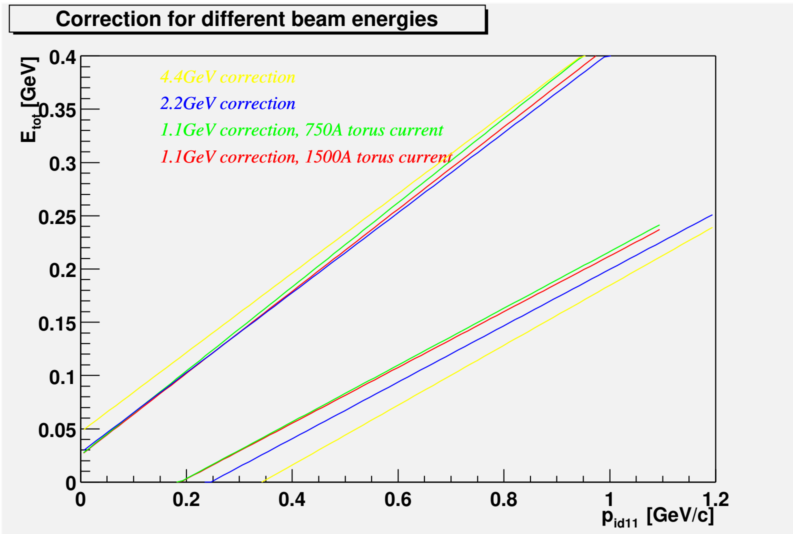

Figure A.6: Comparison of the definitions of the main electron band for the 1.1, 2.2 and 4.4 GeV beam energies

extra work is required for a complete analysis of the data.

A.4 Notes

The parameters and correction function have been checked into the CLAS CVS system and are available from the "`e2run`" section. The ROOT (C++) version was incorporated into E2AnaTool which was written for the analysis of e2 rootDSTs. This can be checked out from "`e2run/root`".

All the plots and fits that were performed are available at `http://www.jlab.org/Hall-B/secure/e2/stevenmc/ElectronId/eid1.html`.

The electron identification correction was derived for the 1.1GeV beam energy runs for e2a. Most of the plots shown here are for the 1500A torus current runs. The method described here is identical to that for the 750A torus current and all the plots are available at the secure web site as described above.

Appendix B

Electron Momentum Corrections for e2a at 1.1GeV

B.1 Introduction

In CLAS, as with other magnetic spectrometers, the momentum of charged particles is measured via the curvature of the path it takes through a set of tracking detectors. For an accurate measurement of the momentum of a particle, an accurate knowledge of the applied magnetic field is required. The hadronic mass W (see equation B.1) is calculated by the detection of a scattered electron. An indication of the quality of the electron detection can be obtained if the hadronic mass is known i.e. scattering electrons from protons.

$$W^2 = m_p^2 + 2m_p\omega - Q^2 \tag{B.1}$$

where

$$\begin{aligned}
Q^2 &= 4E_eE_{e'}\sin^2\left(\tfrac{\theta_{e'}}{2}\right), \\
m_p &= \text{proton mass } [GeV/c^2], \\
\omega &= \text{energy transferred } [GeV], \\
E_e &= \text{incident electron energy } [GeV], \\
E_{e'} &= \text{scattered electron energy } [GeV] \text{ and} \\
\theta_{e'} &= \text{scattered electron polar angle } [^\circ].
\end{aligned}$$

The measured W distribution in CLAS shows that the magnetic field is not precisely known (see figure B.1) since $m_p = 938 MeV/c^2$.

Before any corrections, the elastic peak position was at $0.925\,GeV/c^2$ and the width of the peak was $14.83\,MeV/c^2$. To improve the scattered electron momentum a correction function was introduced to modify the measured electron momentum based

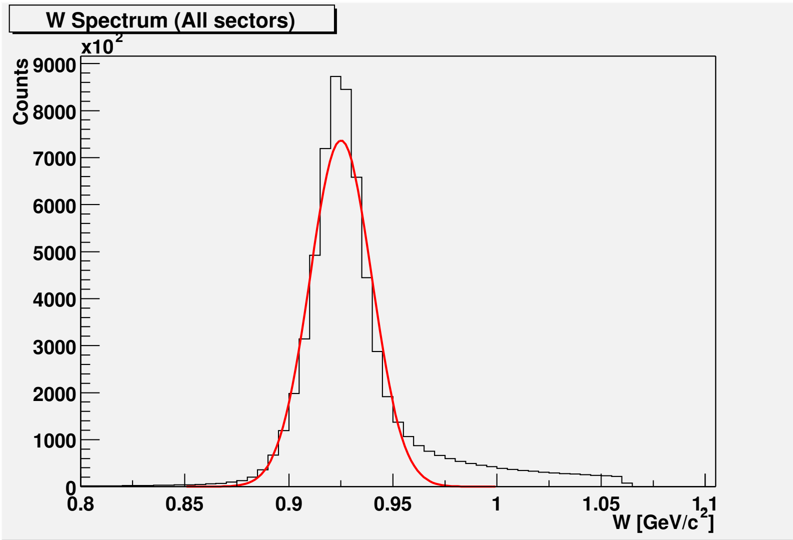

Figure B.1: W spectrum before any corrections (all sectors are summed).

Runs using 750A torus current	Runs using 1500A torus current
16152	16195
16155	16197
16158	16204
16160	16217
16163	16227
16165	16259

Table B.1: Runs used to do the momentum correction

on a known reaction. The reaction used to derive the correction function was elastic scattering and the data used, from the e1b run period, is listed in table B.1.

Events containing only an electron and proton in the final state were preselected for this purpose. This minimised contamination from other processes.

B.2 Correction Method

The correction function has the form

$$\overrightarrow{p_c} = C\left(\left|\overrightarrow{p_m}\right|, \theta_{e'}, \phi_{e'}, s\right) \tag{B.2}$$

where

$$\begin{aligned}
\overrightarrow{p_c} &= \text{corrected scattered electron momentum } [GeV/c], \\
\overrightarrow{p_m} &= \text{measured scattered electron momentum } [GeV/c], \\
\theta_{e'} &= \text{scattered electron polar angle } [^\circ], \\
\phi_{e'} &= \text{scattered electron azimuthal angle } [^\circ] \text{ and} \\
s &= \text{sector number.}
\end{aligned}$$

To simplify the correction, we assume that the scattering angles are measured accurately and that we will correct the magnitude of the scattered momentum. Therefore equation B.2 becomes

$$p_c = p_m \cdot f\left(\theta_{e'}, \phi_{e'}, s\right) \tag{B.3}$$

In elastic scattering the scattered electron momentum can be calculated as follows:

$$p_{calc} = \frac{E_{beam}}{1 + \left[E_{beam}\left(1 - \cos\theta_{e'}\right)\right]/m_p} \tag{B.4}$$

The beam energy was $1.513GeV$ and the scattering angle was assumed accurate (m_p is the proton mass).

The function $f\left(\theta_{e'}, \phi_{e'}, s\right)$ was divided into six independent functions $f_i\left(\theta_{e'}, \phi_{e'}\right)$ where i denotes the sector number. Each sector was then corrected independently and $f_i\left(\theta_{e'}, \phi_{e'}\right)$ was of the form

$$f_i\left(\theta_{e'}, \phi_{e'}\right) = a_{i0}\left(\theta_{e'}\right) + a_{i1}\left(\theta_{e'}\right)\phi_{e'} + ... + a_{i5}\left(\theta_{e'}\right)\phi_{e'}^5 \tag{B.5}$$

To determine the parameters, each sector was divided into 120 $\theta_{e'}$ bins from 0° to 60° and 30 $\phi_{e'}$ bins from −30° to 30°. Each event was assigned a $\left(\theta_{e'}, \phi_{e'}\right)$ bin and the ratio p_{calc}/p_m was calculated for that bin. Thus each bin contained a mean correction factor (and statistical error). Plots of mean correction factor as a function of $\phi_{e'}$ were fitted for 0.5° bins in $\theta_{e'}$ (see figure B.2 for examples). This resulted in 720 functions $g_{ij}\left(\phi_{e'}\right) = b_{i0j} + b_{i1j}\phi_{e'} + ... + b_{i5j}\phi_{e'}^5 \quad (1 \leq j \leq 120)$. Finally, each of the parameters $b_{i0}, ..., b_{i5}$ were fitted as functions of θ with a $3rd$ degree polynomial to give equation B.5 (see figure B.3 for examples). Hence the final correction function contains $6 \times 4 \times 6 = 144$ parameters.

Thus, on an event by event basis, the correction can be applied by first calculating $a_{ik}\left(\theta_{e'}\right) \quad (0 \leq k \leq 5)$ and using these values as parameters to calculate the function $f_i\left(\theta_{e'}, \phi_{e'}\right)$ (equation B.5). The angles $\theta_{e'}$ and $\phi_{e'}$ are preserved and the magnitude of $\overrightarrow{p_m}$ is corrected.

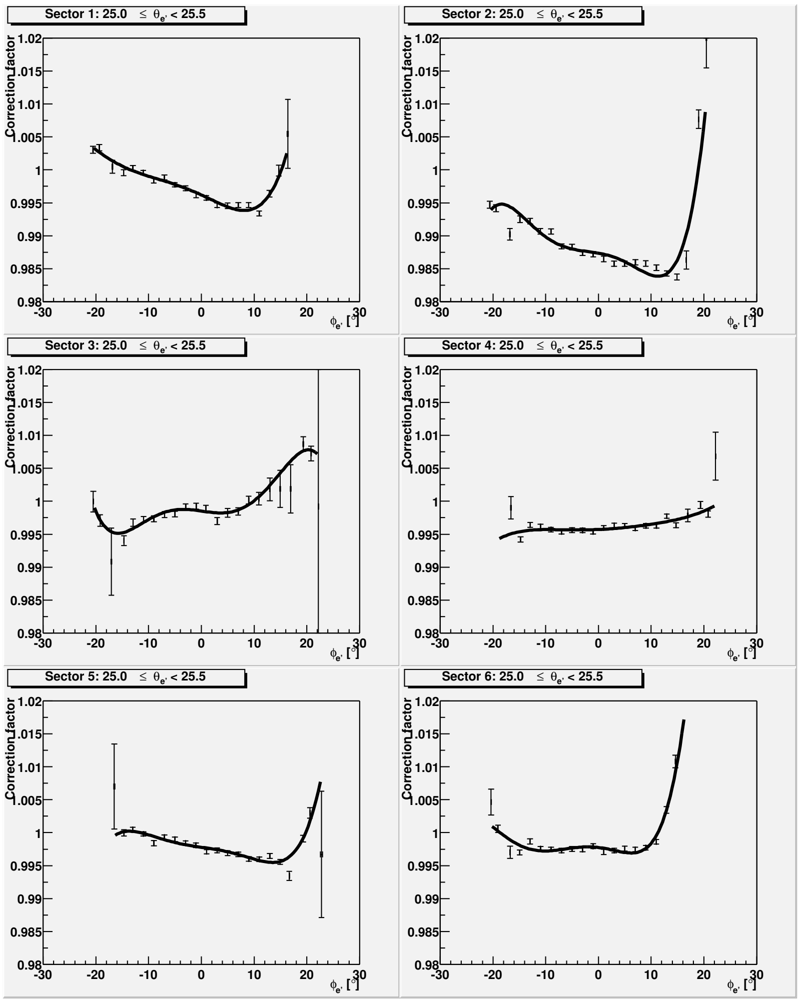

Figure B.2: Examples of the correction factor fits.

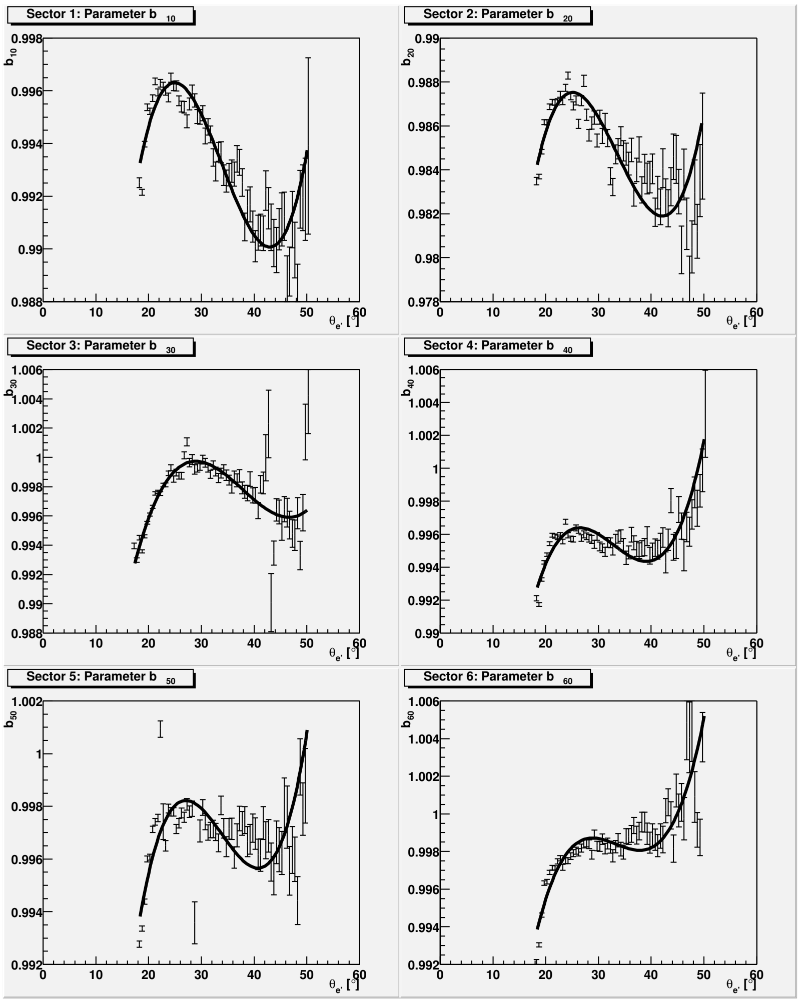

Figure B.3: Examples of the correction factor fit parameter fits.

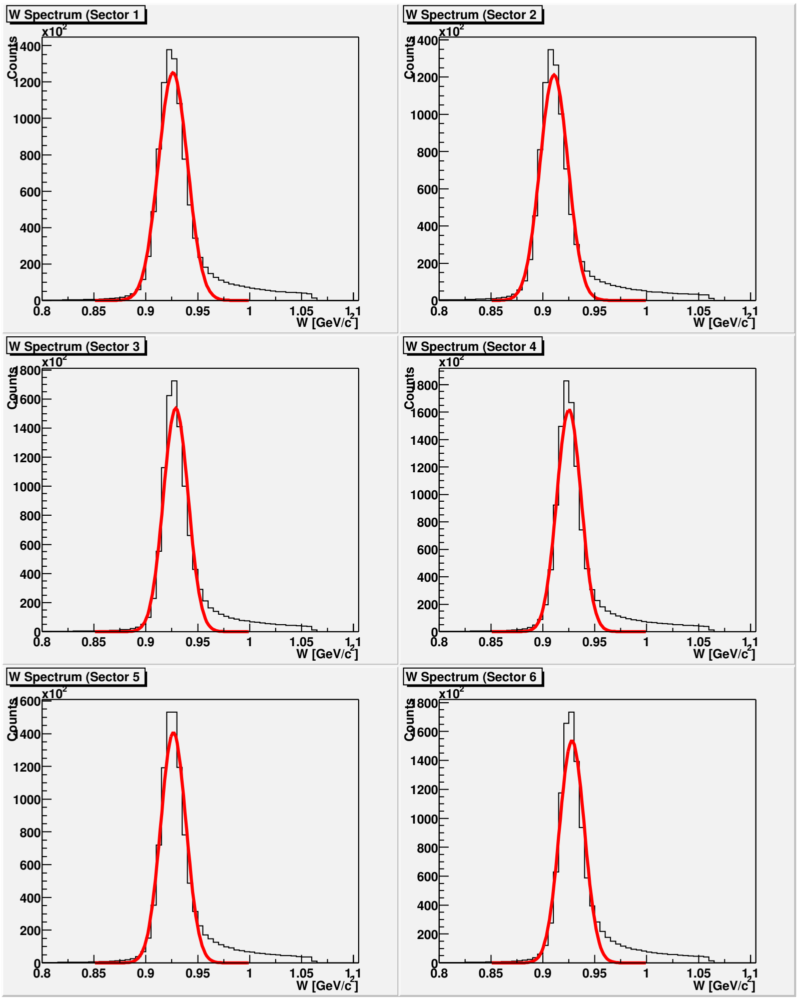

Figure B.4: Uncorrected W spectra for each sector.

B.3 Discussion

A comparison of W spectra before and after the correction is shown in figures B.4 and B.5. The peak positions and widths of the the elastic peaks before and after the correction are shown in figure B.6 and listed in table B.2.

The correction shifts the position of the elastic peak nearer to the proton mass in each sector. When data from all sectors are combined the mean value is 932.2 MeV/c^2 and the width is 10.91 MeV/c^2, as shown in figure B.7.

The fits that were performed to obtain the parameters of the correction are not supposed to match the intricate details of the spectra. They correct the general trend and this is shown to be successful.

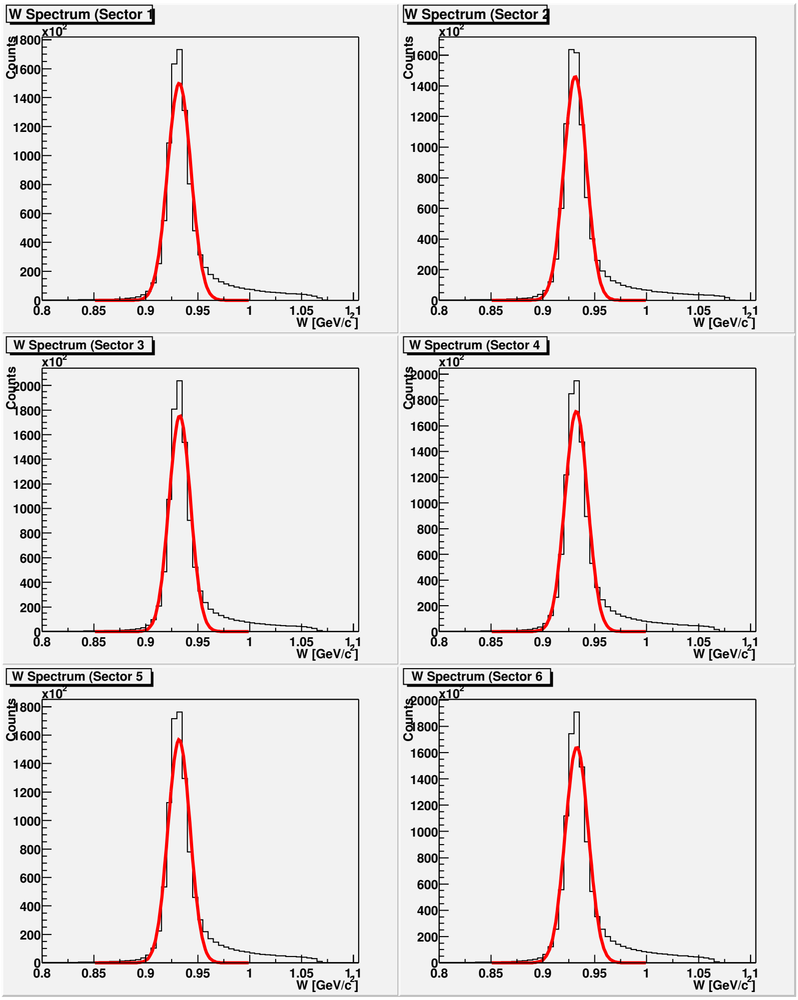

Figure B.5: Corrected W spectra for each sector.

	Uncorrected		Corrected	
Sector Number	**Peak Position** $[GeV/c^2]$	**Peak Width** $[MeV/c^2]$	**Peak Position** $[GeV/c^2]$	**Peak Width** $[MeV/c^2]$
1	0.926	14.0	0.932	11.3
2	0.911	13.5	0.931	10.9
3	0.923	11.8	0.933	10.3
4	0.925	11.7	0.932	11.0
5	0.927	12.2	0.932	10.7
6	0.928	12.0	0.933	11.2
All	0.925	14.8	0.932	10.9

Table B.2: Comparison of elastic peak positions and widths before and after the correction is applied.

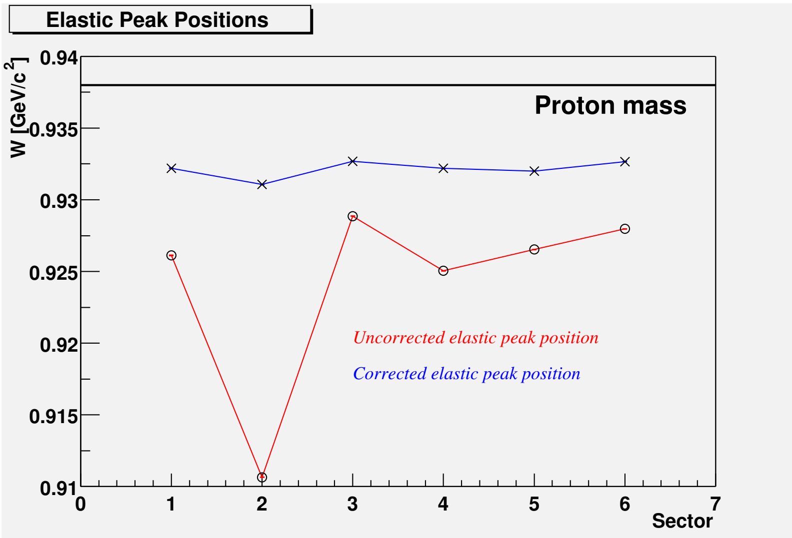

(a) Elastic peak position, before and after correction, for each sector.

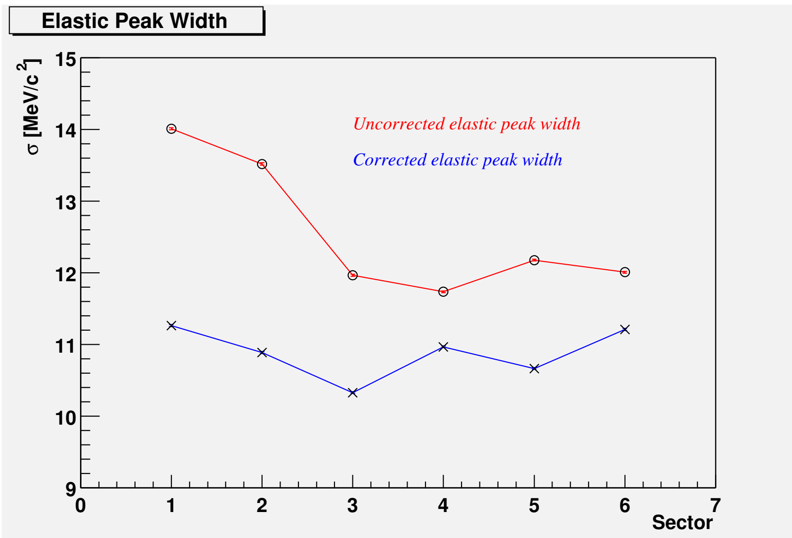

(b) Width of the elastic peak, before and after the correction, for each sector.

Figure B.6: Comparison of the elastic peak positions and widths before and after the correction is applied.

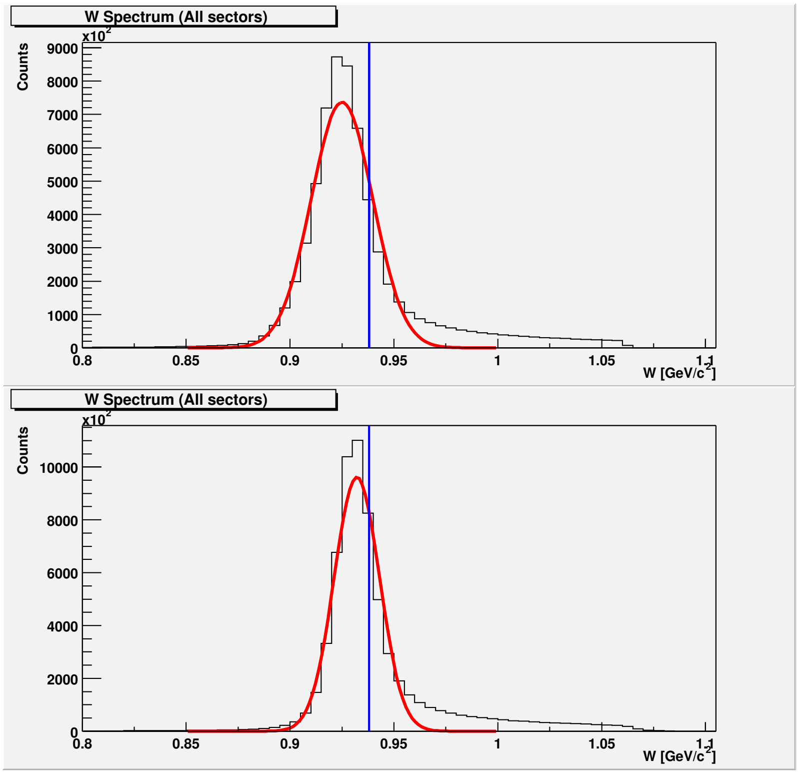

Figure B.7: Comparison of W spectra before (top plot) and after (bottom plot) the correction (all sectors combined)

B.4 Notes

The parameters and correction function have been checked into the CLAS CVS system and are available from the "`e2run`" section. The ROOT (C++) version was incorporated into E2AnaTool which was written for the analysis of e2 rootDSTs. This can be checked out from "`e2run/root`". The PAW (FORTRAN) version is available under "`e2run/packages/nt_functions`" and is called "`EMC_FC_1gev.f`".

All the plots and fits that were performed are available at `http://www.jlab.org/Hall-B/secure/e2/stevenmc/MomentumCorrections/emc1.html`.

The momentum correction was derived for the 1.1GeV beam energy runs for e2a. The plots shown here are for the 1500A torus current runs. The method described here is identical to that for the 750A torus current and all the plots are available at the secure web site as described above.

Appendix C

Electron Fiducial Cuts for e2a at 1.1GeV

C.1 Introduction

The CLAS detector consists of six super conducting coils that generate a toroidal magnetic field with the particle detection system (composed of tracking detectors, particle identification detectors, time of flight detectors and electron detectors) positioned between them. The magnetic field exists in the tracking section and bends charged particles toward or away from the beam line depending on their electric charge and the direction of the current through the coils. The particle detection system is well understood in regions far from the coils and electron detection efficiency is reproducible in these regions using the CLAS GEANT simulation package GSIM. However, close to the coils detection efficiencies are not so well understood. For this reason these regions are discarded and only electrons in the fiducial region are accepted.

The fiducial cut is a set of six functions (one for each sector) that calculate the limits of the good acceptance region. The functions calculate the minimum possible polar scattering angle, $\theta_{e'}$, accepted given the scattered electron momentum, $p_{e'}$, and azimuthal angle $\phi_{e'}$. This can then be compared to the scattered electron's polar angle to determine whether the electron, and event, should be accepted or rejected.

C.2 Deriving The Fiducial Cut Functions

The derivation of the functions that perform the cut was split into three parts. Firstly, a geometric cut was used to eliminate the electrons that are incident near the edges of the detector. After this the good acceptance regions were found. The final step involved parameterising the good acceptance regions to make the cut easily applicable on an event by event basis.

C.2.1 Geometric Cut

The electromagnetic calorimeter is triangular in shape and consists of alternate layers of scintillators and lead. The scintillator bars are arranged in three "views", labelled u, v, and w, orientated at 120° to each other. Small values of u correspond to small values of scattering angle and large values of v and w correspond to large values of $\phi_{e'}$. This gives a natural set of coordinates to make the cut. The ratio $E_{tot}/p_{e'}$, where E_{tot} is the total energy deposited in the calorimeter by the electron and $p_{e'}$ is the momentum of the electron (measured by the drift chambers), is called the sampling fraction. The design of the detector fixes this value to around $0.3c$. Near the edges of the detector this value can decrease as the energy the electron deposits is not all collected due to shower leakage so these regions were discarded.

Figure C.1 shows how the sampling fraction varies with u, v and w. It is clear that at the edges of the detector the ratio $E_{tot}/p_{e'}$ drops dramatically. The cuts

$$u > 20cm,\ v < 368cm,\ w < 403cm,\ E_{tot}/p > 0.2c \tag{C.1}$$

were made and only electrons that lie within this enveloped region were accepted for the next stage. Figure C.2 shows the effect of the geometric cut on example angular distributions and figure C.7 shows the momentum distributions of scattered electrons before and after the cut.

C.2.2 Locating The Good Acceptance Regions

At this stage the distribution of electrons in the detector was examined in more detail. The electrons remaining after the geometric cut were separated into sectors and binned in 22 $50MeV/c$ momentum bins from 0 to $1.1GeV/c$. According to the electron scattering cross section the number of electrons at a fixed momentum and polar scattering angle should be constant across the azimuth. A plot of $\theta_{e'}$ against $\phi_{e'}$ was produced for each momentum bin. The number of electrons falls off at large $\phi_{e'}$ (see figure C.2(b)). The aim was to find the values of $\phi_{e'}$ at the edges of the flat region for each degree in $\theta_{e'}$ in each momentum bin.

To achieve this, each degree in $\theta_{e'}$ in every $\theta_{e'}\ vs\ \phi_{e'}$ plot was projected onto the $\phi_{e'}$ axis and fitted with a trapezoid function

$$y = \begin{cases} 0 & if \quad x \leq p_0 \\ p_4(x-p_0)/(p_1-p_0) & if \quad p_0 < x \leq p_1 \\ p_4 & if \quad p_1 < x \leq p_2 \\ p_4(x-p_3)/(p_2-p_3) & if \quad p_2 < x \leq p_3 \\ 0 & if \quad x > p_3 \end{cases} \tag{C.2}$$

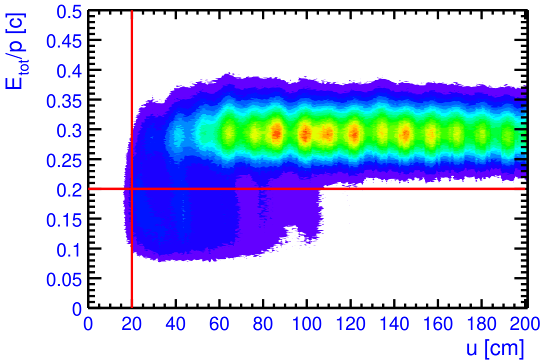

(a) Sampling fraction as a function of u.

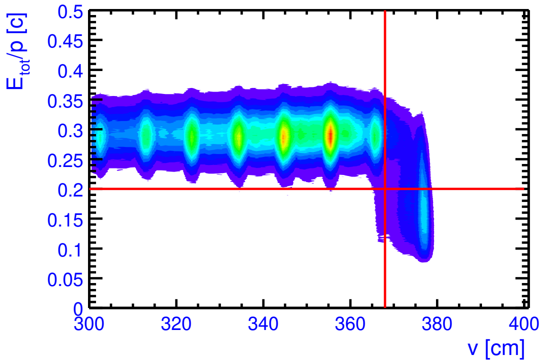

(b) Sampling fraction as a function of v.

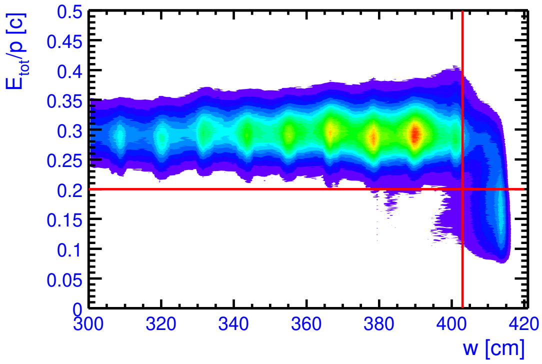

(c) Sampling fraction as a function of w.

Figure C.1: Sampling fraction as a function of u, v and w. Red lines show where the cuts were applied.

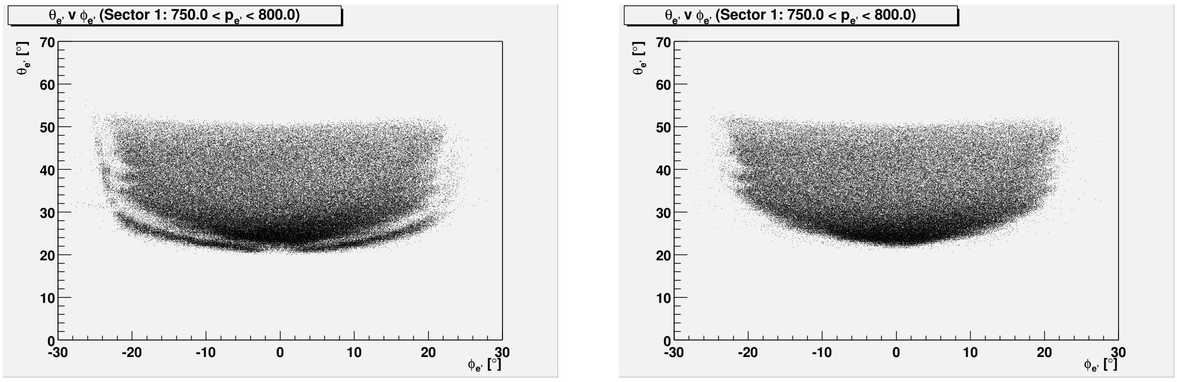

(a) Example angular distribution before the geometric cut.

(b) Example angular distribution after the geometric cut.

Figure C.2: Example angular distributions before and after the geometric cut.

(see figure C.3). The values of $\phi_{e'}$ at the top edges (the upper and lower cut off values, p_1 and p_2) of the functions were recorded. This resulted in $2 \times 60 \times 22 \times 6 = 15840$ parameters that had to be fitted to produce the fiducial functions.

C.2.3 Finding The Fiducial Functions

The cut could be applied by comparing an electron's $\phi_{e'}$ with the upper and lower cut off values for the momentum and $\theta_{e'}$ bin containing the electron. However this would require that all 15840 parameters are stored and the binning structure would be apparent in the final distributions. To make the cut bin independent and more easily applicable the parameters were fitted, firstly with respect to $\theta_{e'}$ and then $p_{e'}$.

The values of p_1 and p_2 were plotted against $\theta_{e'}$ for each momentum bin. The functions

$$\theta_{e'} = \begin{cases} \{\phi\left[\theta_0 - (a_0/b_0)\right] + b_0\theta_0\} / (\phi + b_0) & if \quad \phi \leq 0 \\ \{\phi\left[\theta_0 - (a_1/b_1)\right] - b_1\theta_0\} / (\phi - b_1) & if \quad \phi > 0 \end{cases} \tag{C.3}$$

were then fitted to these plots. Two different functions were fitted so that the upper and lower edges of each sector could be different. The only condition imposed on the two functions was that they met at $\phi_{e'} = 0$. An example of these fits is shown in figure C.4. There were now 6×22 functions (6 sectors, 22 momentum bins) that defined the edges of the good acceptance regions.

The final stage involved introducing a momentum dependence into the fiducial function. This was achieved by fitting the parameters θ_0, a_0, b_0, a_1 and b_1 with a fifth degree polynomial with respect to momentum. Some examples of these fits are shown in figure C.5. This resulted in six functions (one per sector) that define the edges of the good acceptance region:

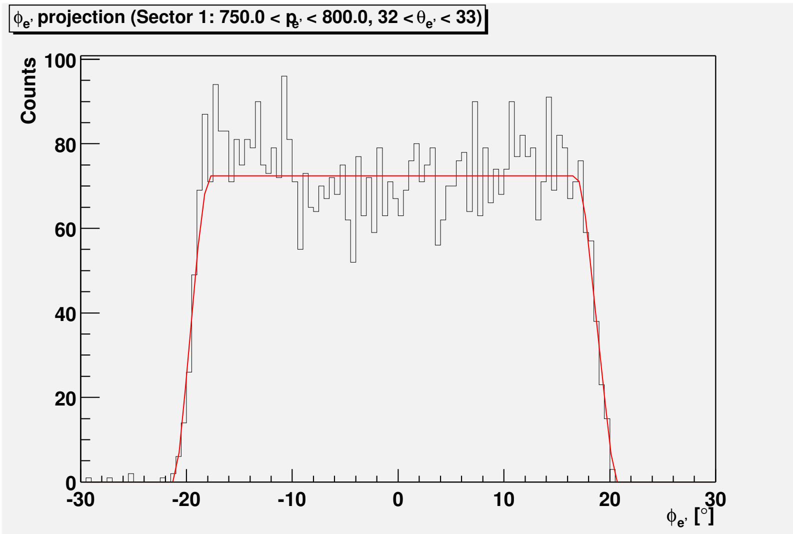

Figure C.3: Example trapezoid fit.

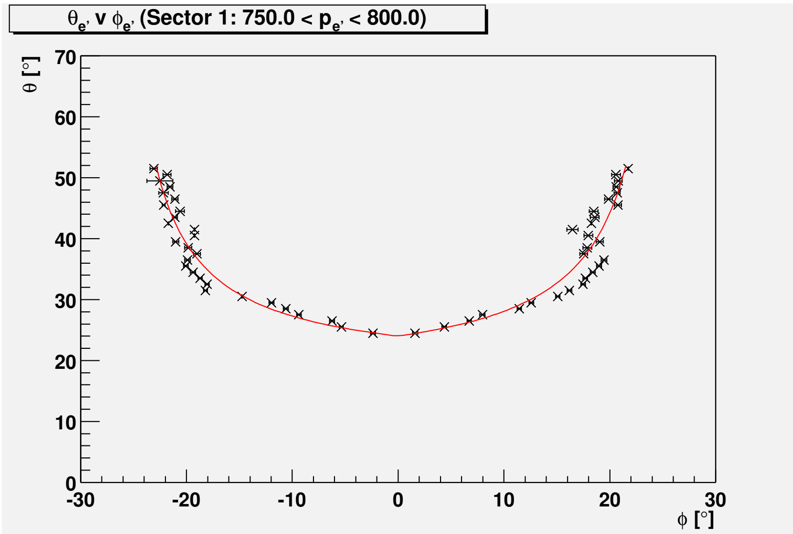

Figure C.4: Example $\theta_{e'}$ parameterisation.

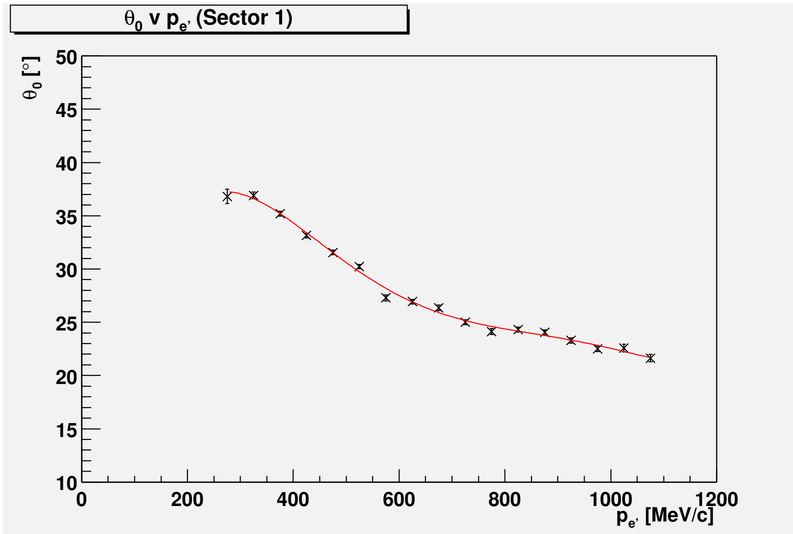

Figure C.5: Example $p_{e'}$ parameterisation.

$$\theta_{e'} = \begin{cases} \{\phi\left[\theta_0 - (a_0(p_{e'})/b_0(p_{e'}))\right] + b_0(p_{e'})\,\theta_0\}/(\phi + b_0(p_{e'})) & if \quad \phi \leq 0 \\ \{\phi\left[\theta_0 - (a_1(p_{e'})/b_1(p_{e'}))\right] - b_1(p_{e'})\,\theta_0\}/(\phi - b_1(p_{e'})) & if \quad \phi > 0 \end{cases} \tag{C.4}$$

At this stage there were 30 fit parameters per sector.

C.3 Discussion

Figure C.6 shows the improvement that the cut makes on the data. Before the cut the distributions of electrons is clearly affected by the detector. When the cut is applied, the distribution reflects the physics of the experiment rather than features of the detector.

Figure C.7 shows the scattered electron momentum distribution at different stages of the procedure. Around half of the electrons are discarded by the fiducial cut. Most of the discarded electrons are from the high momentum region of the spectrum. This is because most of the high momentum electrons are directed at small $\theta_{e'}$ where the $\phi_{e'}$ acceptance is small. Only electrons with momentum greater than $300MeV/c$ were accepted in the final cut since there were not enough electrons in this region to perform the cut and the fits cannot be extrapolated to this extent.

The cut is implemented by first of all using the momentum of the electron to calculate the parameters θ_0, a_0, b_0, a_1 and b_1. These values are then entered into equation C.4, along with $\phi_{e'}$, to calculate two lower limit values of scattering angle θ - one for upper $\phi_{e'}$ and one for lower $\phi_{e'}$ values. The measured value of $\theta_{e'}$ is then compared to the relevant calculated limit. If the measured $\theta_{e'}$ is above the lower limit

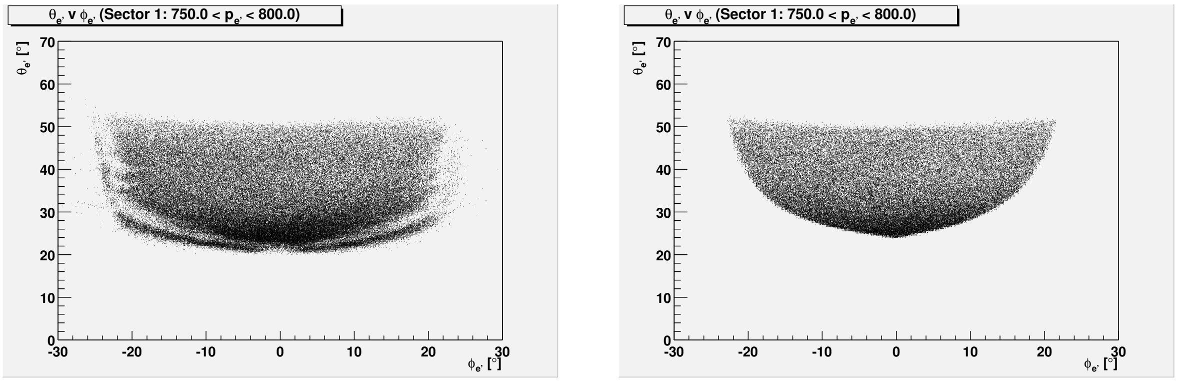

(a) Example angular distribution before any cuts are applied

(b) Example angular distribution with the fiducial cut applied

Figure C.6: Comparison of angular distributions before and after the fiducial cut.

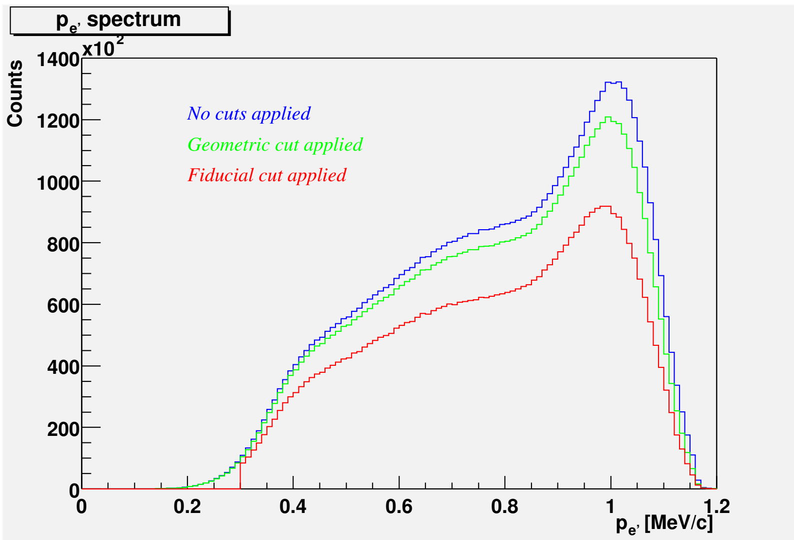

Figure C.7: Comparison of scattered electron momenta at various stages of the correction.

then the electron, and the event, is accepted for analysis. Otherwise, the event is discarded. Figure C.6 shows an example angular distribution before and after the fiducial cut.

The fits described above are not supposed to match the intricate details of the spectra. They fit the general trend and derive the cut function, and this has been shown to be successful.

C.4 Notes

The parameters and cut function have been checked into the CLAS CVS system and are available from the "`e2run`" section. The ROOT (C++) version was incorporated into E2AnaTool which was written for the analysis of e2 rootDSTs. This can be checked out from "`e2run/root`". The PAW (FORTRAN) version is available under "`e2run/packages/nt_functions`" and is called "`EMC_FC_1gev.f`".

All the plots and fits that were performed are available at `http://www.jlab.org/Hall-B/secure/e2/stevenmc/FiducialCuts/efc1.html`.

The fiducial cut was derived for the 1.1*GeV* beam energy runs for e2a. The plots shown here are for the 1500A torus current runs. The method described here is identical to that for the 750A torus current and all the plots are available at the secure web site as described above.

Appendix D

Tables of Cross Sections

W $[GeV/c^2]$	$d^2\sigma/dQ^2dW$ $[\mu b/GeV^3]$			
	Q^2 $[(GeV/c)^2]$			
	0.1875 ± 0.0125	0.2125 ± 0.0125	0.2375 ± 0.0125	0.2625 ± 0.0125
0.705 ± 0.005				
0.715 ± 0.005				
0.725 ± 0.005				
0.735 ± 0.005				
0.745 ± 0.005				
0.755 ± 0.005				
0.765 ± 0.005				
0.775 ± 0.005				
0.785 ± 0.005				
0.795 ± 0.005				0.567 ± 0.084
0.805 ± 0.005			0.558 ± 0.140	1.867 ± 0.173
0.815 ± 0.005			2.272 ± 0.245	3.158 ± 0.239
0.825 ± 0.005		3.267 ± 0.483	5.473 ± 0.465	5.512 ± 0.414
0.835 ± 0.005	3.954 ± 1.060	9.632 ± 1.025	7.550 ± 0.570	6.721 ± 0.468
0.845 ± 0.005	11.475 ± 1.556	13.502 ± 1.251	9.355 ± 0.698	8.910 ± 0.566
0.855 ± 0.005	15.156 ± 1.672	15.279 ± 1.362	15.577 ± 1.151	13.146 ± 0.853
0.865 ± 0.005	15.765 ± 1.734	20.718 ± 1.814	20.108 ± 1.403	16.483 ± 1.055
0.875 ± 0.005	18.750 ± 2.064	24.441 ± 1.888	23.027 ± 1.652	17.655 ± 1.067
0.885 ± 0.005	26.272 ± 2.692	27.965 ± 2.248	25.905 ± 1.742	21.089 ± 1.297
0.895 ± 0.005	28.501 ± 2.994	33.175 ± 2.614	32.334 ± 2.181	27.911 ± 1.808
0.905 ± 0.005	25.536 ± 2.604	36.089 ± 2.912	33.717 ± 2.270	28.285 ± 1.744
0.915 ± 0.005	33.240 ± 3.611	41.615 ± 3.307	32.444 ± 2.063	29.905 ± 1.787
0.925 ± 0.005	30.747 ± 3.284	40.571 ± 3.178	37.731 ± 2.464	33.370 ± 1.974
0.935 ± 0.005	33.577 ± 3.651	48.271 ± 3.797	38.499 ± 2.415	32.783 ± 1.886
0.945 ± 0.005	39.504 ± 4.465	45.238 ± 3.630	41.400 ± 2.564	33.381 ± 1.905
0.955 ± 0.005	35.820 ± 3.887	42.070 ± 3.184	42.240 ± 2.552	33.088 ± 1.829
0.965 ± 0.005	27.808 ± 2.800	44.299 ± 3.386	41.152 ± 2.480	37.202 ± 2.171
0.975 ± 0.005	34.064 ± 3.570	38.467 ± 2.791	45.021 ± 2.789	33.707 ± 1.878
0.985 ± 0.005	37.450 ± 4.293	44.669 ± 3.260	38.230 ± 2.237	34.336 ± 1.877
0.995 ± 0.005	33.708 ± 3.649	40.795 ± 2.960	34.444 ± 1.975	32.155 ± 1.702
1.005 ± 0.005	28.659 ± 2.903	32.022 ± 2.243	35.185 ± 2.038	29.967 ± 1.543
1.015 ± 0.005	27.378 ± 2.778	32.548 ± 2.224	32.867 ± 1.899	27.078 ± 1.389
1.025 ± 0.005	22.043 ± 2.181	29.694 ± 1.991	28.021 ± 1.587	26.019 ± 1.299
1.035 ± 0.005	20.050 ± 1.966	27.001 ± 1.747	24.609 ± 1.347	22.197 ± 1.094
1.045 ± 0.005	20.111 ± 1.946	23.889 ± 1.536	23.443 ± 1.244	21.192 ± 1.051
1.055 ± 0.005	18.090 ± 1.667	22.665 ± 1.407	21.463 ± 1.161	20.674 ± 1.042
1.065 ± 0.005	16.286 ± 1.462	20.795 ± 1.274	19.073 ± 1.013	18.544 ± 0.919
1.075 ± 0.005	14.029 ± 1.185	21.116 ± 1.273	18.524 ± 0.984	17.350 ± 0.819
1.085 ± 0.005	14.001 ± 1.118	18.361 ± 1.068	18.239 ± 0.942	16.126 ± 0.764
1.095 ± 0.005	14.564 ± 1.138	19.076 ± 1.113	18.827 ± 0.959	17.120 ± 0.798
1.105 ± 0.005	14.892 ± 1.159	18.350 ± 1.038	16.031 ± 0.796	16.757 ± 0.780
1.115 ± 0.005	13.740 ± 1.008	17.816 ± 0.984	17.587 ± 0.847	15.001 ± 0.664
1.125 ± 0.005	16.046 ± 1.177	18.493 ± 0.981	17.088 ± 0.817	15.829 ± 0.697
1.135 ± 0.005	15.306 ± 1.122	18.263 ± 0.972	16.907 ± 0.786	15.419 ± 0.661
1.145 ± 0.005	16.073 ± 1.113	18.993 ± 0.989	17.012 ± 0.772	14.799 ± 0.618

Table D.1: Inclusive cross sections $d^2\sigma/dQ^2dW$ for $0.1875 \leq Q^2 \leq 0.2625$ $(GeV/c)^2$ and $0.705 \leq W \leq 1.145\, GeV/c^2$.

W $[GeV/c^2]$	$d^2\sigma/dQ^2dW$ $[\mu b/GeV^3]$		
	Q^2 $[(GeV/c)^2]$		
	0.2875 ± 0.0125	0.3125 ± 0.0125	0.3375 ± 0.0125
0.705 ± 0.005			
0.715 ± 0.005			
0.725 ± 0.005			
0.735 ± 0.005			
0.745 ± 0.005			0.012 ± 0.003
0.755 ± 0.005			0.175 ± 0.030
0.765 ± 0.005		0.152 ± 0.029	0.509 ± 0.054
0.775 ± 0.005	0.053 ± 0.016	0.657 ± 0.073	0.670 ± 0.059
0.785 ± 0.005	0.584 ± 0.072	1.128 ± 0.094	1.239 ± 0.098
0.795 ± 0.005	1.367 ± 0.118	1.805 ± 0.136	1.992 ± 0.140
0.805 ± 0.005	2.416 ± 0.176	2.693 ± 0.192	2.673 ± 0.170
0.815 ± 0.005	3.572 ± 0.248	4.111 ± 0.277	3.745 ± 0.235
0.825 ± 0.005	4.851 ± 0.313	5.390 ± 0.349	4.464 ± 0.269
0.835 ± 0.005	7.437 ± 0.457	5.605 ± 0.331	4.721 ± 0.275
0.845 ± 0.005	9.531 ± 0.575	8.399 ± 0.489	6.689 ± 0.383
0.855 ± 0.005	11.356 ± 0.682	9.391 ± 0.547	8.469 ± 0.480
0.865 ± 0.005	13.991 ± 0.824	11.965 ± 0.695	10.486 ± 0.575
0.875 ± 0.005	15.115 ± 0.877	13.534 ± 0.737	10.687 ± 0.571
0.885 ± 0.005	18.891 ± 1.056	16.724 ± 0.914	13.473 ± 0.744
0.895 ± 0.005	22.567 ± 1.305	17.414 ± 0.920	13.303 ± 0.701
0.905 ± 0.005	23.300 ± 1.274	20.617 ± 1.102	15.980 ± 0.822
0.915 ± 0.005	25.927 ± 1.407	20.217 ± 1.060	16.580 ± 0.854
0.925 ± 0.005	27.692 ± 1.467	22.003 ± 1.144	17.405 ± 0.860
0.935 ± 0.005	28.994 ± 1.534	22.983 ± 1.212	19.440 ± 0.990
0.945 ± 0.005	28.639 ± 1.555	23.092 ± 1.184	18.744 ± 0.930
0.955 ± 0.005	32.442 ± 1.762	23.790 ± 1.186	19.632 ± 0.953
0.965 ± 0.005	31.154 ± 1.629	23.674 ± 1.167	19.297 ± 0.928
0.975 ± 0.005	30.200 ± 1.554	20.624 ± 1.009	18.510 ± 0.876
0.985 ± 0.005	30.181 ± 1.522	23.000 ± 1.095	18.745 ± 0.888
0.995 ± 0.005	27.097 ± 1.371	22.676 ± 1.124	16.656 ± 0.772
1.005 ± 0.005	24.467 ± 1.216	18.983 ± 0.887	16.878 ± 0.768
1.015 ± 0.005	24.685 ± 1.218	18.838 ± 0.890	16.352 ± 0.725
1.025 ± 0.005	21.785 ± 1.041	18.136 ± 0.841	14.703 ± 0.650
1.035 ± 0.005	20.215 ± 0.983	16.318 ± 0.736	14.995 ± 0.663
1.045 ± 0.005	19.463 ± 0.949	15.979 ± 0.721	12.906 ± 0.561
1.055 ± 0.005	18.011 ± 0.847	13.923 ± 0.621	12.487 ± 0.530
1.065 ± 0.005	16.923 ± 0.780	14.432 ± 0.648	13.078 ± 0.576
1.075 ± 0.005	14.387 ± 0.630	12.311 ± 0.516	11.476 ± 0.479
1.085 ± 0.005	13.454 ± 0.591	11.989 ± 0.511	10.888 ± 0.449
1.095 ± 0.005	13.610 ± 0.586	12.896 ± 0.541	10.865 ± 0.448
1.105 ± 0.005	12.865 ± 0.549	11.736 ± 0.478	10.035 ± 0.400
1.115 ± 0.005	12.846 ± 0.542	12.127 ± 0.491	10.574 ± 0.414
1.125 ± 0.005	13.646 ± 0.566	11.031 ± 0.436	9.934 ± 0.382
1.135 ± 0.005	12.968 ± 0.534	12.062 ± 0.473	9.608 ± 0.364
1.145 ± 0.005	13.307 ± 0.538	11.449 ± 0.436	10.570 ± 0.402

Table D.2: Inclusive cross sections $d^2\sigma/dQ^2dW$ for $0.2875 \leq Q^2 \leq 0.3375\ (GeV/c)^2$ and $0.705 \leq W \leq 1.145\,GeV/c^2$.

W $[GeV/c^2]$	$d^2\sigma/dQ^2dW$ $[\mu b/GeV^3]$ Q^2 $[(GeV/c)^2]$			
	0.1875 ± 0.0125	0.2125 ± 0.0125	0.2375 ± 0.0125	0.2625 ± 0.0125
1.155 ± 0.005	16.517 ± 1.106	18.059 ± 0.919	16.507 ± 0.726	16.268 ± 0.666
1.165 ± 0.005	17.057 ± 1.092	19.506 ± 0.968	18.175 ± 0.800	15.653 ± 0.641
1.175 ± 0.005	16.547 ± 1.055	20.276 ± 1.007	18.286 ± 0.798	15.956 ± 0.643
1.185 ± 0.005	17.939 ± 1.132	18.761 ± 0.883	19.748 ± 0.849	16.130 ± 0.635
1.195 ± 0.005	17.724 ± 1.051	20.298 ± 0.929	17.693 ± 0.735	16.803 ± 0.658
1.205 ± 0.005	18.631 ± 1.087	21.459 ± 0.993	19.408 ± 0.811	15.786 ± 0.600
1.215 ± 0.005	19.476 ± 1.102	19.605 ± 0.870	19.248 ± 0.781	17.017 ± 0.638
1.225 ± 0.005	17.342 ± 0.951	18.475 ± 0.797	19.149 ± 0.737	16.362 ± 0.592
1.235 ± 0.005	17.614 ± 0.929	19.966 ± 0.854	18.873 ± 0.736	15.404 ± 0.544
1.245 ± 0.005	18.703 ± 0.980	18.630 ± 0.769	18.581 ± 0.689	15.893 ± 0.555
1.255 ± 0.005	16.817 ± 0.858	18.123 ± 0.718	17.451 ± 0.644	15.948 ± 0.534
1.265 ± 0.005	17.643 ± 0.872	18.680 ± 0.748	17.499 ± 0.626	15.432 ± 0.521
1.275 ± 0.005	16.381 ± 0.781	17.434 ± 0.679	17.090 ± 0.599	15.122 ± 0.495
1.285 ± 0.005	14.743 ± 0.692	18.397 ± 0.704	16.519 ± 0.567	15.035 ± 0.480
1.295 ± 0.005	15.774 ± 0.716	17.074 ± 0.635	15.294 ± 0.506	14.480 ± 0.459
1.305 ± 0.005	14.567 ± 0.639	16.330 ± 0.599	15.752 ± 0.514	14.208 ± 0.439
1.315 ± 0.005	14.645 ± 0.631	15.617 ± 0.564	14.206 ± 0.457	13.459 ± 0.407
1.325 ± 0.005	14.222 ± 0.598	15.447 ± 0.534	14.439 ± 0.452	13.056 ± 0.388
1.335 ± 0.005	13.157 ± 0.527	15.201 ± 0.511		
1.345 ± 0.005	13.945 ± 0.549	14.355 ± 0.472		
1.355 ± 0.005	13.740 ± 0.530	15.589 ± 0.504		
1.365 ± 0.005	13.497 ± 0.504			
1.375 ± 0.005	13.778 ± 0.510			
1.385 ± 0.005				
1.395 ± 0.005				
1.405 ± 0.005				
1.415 ± 0.005				
1.425 ± 0.005				
1.435 ± 0.005				
1.445 ± 0.005				
1.455 ± 0.005				
1.465 ± 0.005				
1.475 ± 0.005				
1.485 ± 0.005				
1.495 ± 0.005				
1.505 ± 0.005				
1.515 ± 0.005				
1.525 ± 0.005				
1.535 ± 0.005				
1.545 ± 0.005				
1.555 ± 0.005				
1.565 ± 0.005				
1.575 ± 0.005				
1.585 ± 0.005				
1.595 ± 0.005				

Table D.3: Inclusive cross sections $d^2\sigma/dQ^2dW$ for $0.1875 \leq Q^2 \leq 0.2625$ $(GeV/c)^2$ and $1.155 \leq W \leq 1.595\,GeV/c^2$.

W $\left[GeV/c^2\right]$	$d^2\sigma/dQ^2dW$ $\left[\mu b/GeV^3\right]$ Q^2 $\left[(GeV/c)^2\right]$ 0.2875 ± 0.0125	0.3125 ± 0.0125	0.3375 ± 0.0125
1.155 ± 0.005	13.882 ± 0.554	12.015 ± 0.450	10.254 ± 0.382
1.165 ± 0.005	13.494 ± 0.523	11.179 ± 0.415	10.033 ± 0.362
1.175 ± 0.005	14.645 ± 0.549	12.319 ± 0.450	10.783 ± 0.385
1.185 ± 0.005	13.218 ± 0.488	11.698 ± 0.415	10.580 ± 0.372
1.195 ± 0.005	14.555 ± 0.532	12.655 ± 0.446	10.598 ± 0.363
1.205 ± 0.005	14.052 ± 0.502	12.284 ± 0.421	9.997 ± 0.337
1.215 ± 0.005	14.019 ± 0.493	11.853 ± 0.397	10.624 ± 0.349
1.225 ± 0.005	13.619 ± 0.463	12.508 ± 0.421	9.637 ± 0.315
1.235 ± 0.005	14.206 ± 0.476	11.765 ± 0.387	10.353 ± 0.335
1.245 ± 0.005	13.541 ± 0.453	11.770 ± 0.378	10.285 ± 0.323
1.255 ± 0.005	13.743 ± 0.449	11.476 ± 0.360	9.898 ± 0.306
1.265 ± 0.005	13.320 ± 0.424	11.372 ± 0.350	9.678 ± 0.296
1.275 ± 0.005	12.692 ± 0.400	11.247 ± 0.342	9.270 ± 0.278
1.285 ± 0.005	12.325 ± 0.380	10.950 ± 0.332	9.018 ± 0.264
1.295 ± 0.005	12.435 ± 0.381	10.774 ± 0.317	9.163 ± 0.268
1.305 ± 0.005	12.120 ± 0.360		
1.315 ± 0.005	11.910 ± 0.350		
1.325 ± 0.005			
1.335 ± 0.005			
1.345 ± 0.005			
1.355 ± 0.005			
1.365 ± 0.005			
1.375 ± 0.005			
1.385 ± 0.005			
1.395 ± 0.005			
1.405 ± 0.005			
1.415 ± 0.005			
1.425 ± 0.005			
1.435 ± 0.005			
1.445 ± 0.005			
1.455 ± 0.005			
1.465 ± 0.005			
1.475 ± 0.005			
1.485 ± 0.005			
1.495 ± 0.005			
1.505 ± 0.005			
1.515 ± 0.005			
1.525 ± 0.005			
1.535 ± 0.005			
1.545 ± 0.005			
1.555 ± 0.005			
1.565 ± 0.005			
1.575 ± 0.005			
1.585 ± 0.005			
1.595 ± 0.005			

Table D.4: Inclusive cross sections $d^2\sigma/dQ^2dW$ for $0.2875 \leq Q^2 \leq 0.3375\,(GeV/c)^2$ and $1.155 \leq W \leq 1.595\,GeV/c^2$.

W $\left[GeV/c^2\right]$	$d^2\sigma/dQ^2dW$ $\left[\mu b/GeV^3\right]$		
	Q^2 $\left[(GeV/c)^2\right]$		
	0.1875 ± 0.0125	0.2125 ± 0.0125	0.2375 ± 0.0125
0.705 ± 0.005			
0.715 ± 0.005			
0.725 ± 0.005			
0.735 ± 0.005			
0.745 ± 0.005			
0.755 ± 0.005			
0.765 ± 0.005			
0.775 ± 0.005			
0.785 ± 0.005			
0.795 ± 0.005			
0.805 ± 0.005			
0.815 ± 0.005			
0.825 ± 0.005			
0.835 ± 0.005			
0.845 ± 0.005			
0.855 ± 0.005			
0.865 ± 0.005			
0.875 ± 0.005			
0.885 ± 0.005			
0.895 ± 0.005			
0.905 ± 0.005			
0.915 ± 0.005			
0.925 ± 0.005			
0.935 ± 0.005			
0.945 ± 0.005			
0.955 ± 0.005			
0.965 ± 0.005			
0.975 ± 0.005			
0.985 ± 0.005			
0.995 ± 0.005			
1.005 ± 0.005			0.107 ± 0.048
1.015 ± 0.005			0.042 ± 0.022
1.025 ± 0.005	0.049 ± 0.031	0.051 ± 0.027	0.111 ± 0.035
1.035 ± 0.005	0.042 ± 0.026	0.107 ± 0.032	0.083 ± 0.024
1.045 ± 0.005	0.397 ± 0.134	0.172 ± 0.041	0.159 ± 0.033
1.055 ± 0.005	0.101 ± 0.030	0.163 ± 0.035	0.176 ± 0.035
1.065 ± 0.005	0.181 ± 0.044	0.246 ± 0.047	0.234 ± 0.039
1.075 ± 0.005	0.242 ± 0.052	0.251 ± 0.042	0.292 ± 0.042
1.085 ± 0.005	0.233 ± 0.043	0.384 ± 0.054	0.479 ± 0.058
1.095 ± 0.005	0.561 ± 0.097	0.468 ± 0.060	0.453 ± 0.052
1.105 ± 0.005	0.496 ± 0.072	0.632 ± 0.073	0.479 ± 0.053
1.115 ± 0.005	0.689 ± 0.106	0.860 ± 0.093	0.666 ± 0.066
1.125 ± 0.005	0.848 ± 0.109	0.845 ± 0.086	0.679 ± 0.062
1.135 ± 0.005	0.805 ± 0.100	1.034 ± 0.099	0.843 ± 0.077
1.145 ± 0.005	0.895 ± 0.102	1.152 ± 0.101	0.989 ± 0.081

Table D.5: Semi inclusive cross sections $d^2\sigma/dQ^2dW$ for $0.1875 \leq Q^2 \leq 0.2375\,(GeV/c)^2$ and $0.705 \leq W \leq 1.145\,GeV/c^2$.

W $\left[GeV/c^2\right]$	$d^2\sigma/dQ^2dW$ $\left[\mu b/GeV^3\right]$		
	Q^2 $\left[(GeV/c)^2\right]$		
	0.2625 ± 0.0125	0.2875 ± 0.0125	0.3125 ± 0.0125
0.705 ± 0.005			
0.715 ± 0.005			
0.725 ± 0.005			
0.735 ± 0.005			
0.745 ± 0.005			
0.755 ± 0.005			
0.765 ± 0.005			
0.775 ± 0.005			
0.785 ± 0.005			
0.795 ± 0.005			
0.805 ± 0.005			
0.815 ± 0.005			
0.825 ± 0.005			
0.835 ± 0.005			
0.845 ± 0.005			
0.855 ± 0.005			
0.865 ± 0.005			
0.875 ± 0.005			
0.885 ± 0.005			
0.895 ± 0.005			
0.905 ± 0.005			
0.915 ± 0.005			
0.925 ± 0.005			
0.935 ± 0.005			
0.945 ± 0.005			
0.955 ± 0.005			
0.965 ± 0.005			
0.975 ± 0.005			0.028 ± 0.020
0.985 ± 0.005		0.073 ± 0.038	0.039 ± 0.020
0.995 ± 0.005	0.056 ± 0.029	0.023 ± 0.017	0.024 ± 0.014
1.005 ± 0.005	0.088 ± 0.035	0.037 ± 0.019	0.060 ± 0.021
1.015 ± 0.005	0.062 ± 0.023	0.038 ± 0.016	0.064 ± 0.019
1.025 ± 0.005	0.099 ± 0.028	0.090 ± 0.023	0.061 ± 0.018
1.035 ± 0.005	0.102 ± 0.026	0.064 ± 0.018	0.096 ± 0.022
1.045 ± 0.005	0.145 ± 0.031	0.143 ± 0.027	0.123 ± 0.025
1.055 ± 0.005	0.166 ± 0.030	0.160 ± 0.027	0.172 ± 0.028
1.065 ± 0.005	0.238 ± 0.038	0.169 ± 0.029	0.139 ± 0.023
1.075 ± 0.005	0.448 ± 0.055	0.234 ± 0.033	0.237 ± 0.033
1.085 ± 0.005	0.337 ± 0.041	0.294 ± 0.036	0.261 ± 0.033
1.095 ± 0.005	0.478 ± 0.053	0.340 ± 0.040	0.246 ± 0.031
1.105 ± 0.005	0.440 ± 0.047	0.447 ± 0.047	0.294 ± 0.033
1.115 ± 0.005	0.569 ± 0.058	0.438 ± 0.043	0.317 ± 0.034
1.125 ± 0.005	0.644 ± 0.059	0.494 ± 0.047	0.421 ± 0.042
1.135 ± 0.005	0.858 ± 0.076	0.711 ± 0.061	0.620 ± 0.052
1.145 ± 0.005	0.841 ± 0.069	0.682 ± 0.057	0.624 ± 0.052

Table D.6: Semi inclusive cross sections $d^2\sigma/dQ^2dW$ for $0.2625 \leq Q^2 \leq 0.3125\,(GeV/c)^2$ and $0.705 \leq W \leq 1.145\,GeV/c^2$.

W $[GeV/c^2]$	$d^2\sigma/dQ^2dW$ $[\mu b/GeV^3]$		
	Q^2 $\left[(GeV/c)^2\right]$		
	0.1875 ± 0.0125	0.2125 ± 0.0125	0.2375 ± 0.0125
1.155 ± 0.005	1.153 ± 0.126	1.199 ± 0.105	1.196 ± 0.100
1.165 ± 0.005	1.029 ± 0.105	1.411 ± 0.118	1.101 ± 0.085
1.175 ± 0.005	1.280 ± 0.125	1.454 ± 0.116	1.419 ± 0.108
1.185 ± 0.005	1.516 ± 0.146	1.471 ± 0.110	1.387 ± 0.099
1.195 ± 0.005	1.523 ± 0.138	1.571 ± 0.117	1.394 ± 0.097
1.205 ± 0.005	1.876 ± 0.164	1.650 ± 0.115	1.448 ± 0.098
1.215 ± 0.005	1.860 ± 0.166	1.655 ± 0.117	1.594 ± 0.106
1.225 ± 0.005	1.561 ± 0.129	1.629 ± 0.114	1.579 ± 0.102
1.235 ± 0.005	1.560 ± 0.122	1.654 ± 0.115	1.384 ± 0.088
1.245 ± 0.005	1.667 ± 0.135	1.516 ± 0.099	1.529 ± 0.092
1.255 ± 0.005	1.707 ± 0.135	1.650 ± 0.105	1.539 ± 0.094
1.265 ± 0.005	1.601 ± 0.121	1.861 ± 0.120	1.557 ± 0.094
1.275 ± 0.005	1.465 ± 0.106	1.606 ± 0.100	1.506 ± 0.090
1.285 ± 0.005	1.558 ± 0.110	1.586 ± 0.097	1.731 ± 0.098
1.295 ± 0.005	1.570 ± 0.111	1.634 ± 0.099	1.535 ± 0.085
1.305 ± 0.005	1.500 ± 0.104	1.366 ± 0.082	1.575 ± 0.088
1.315 ± 0.005	1.538 ± 0.103	1.647 ± 0.096	1.483 ± 0.081
1.325 ± 0.005	1.434 ± 0.094	1.478 ± 0.085	1.430 ± 0.077
1.335 ± 0.005	1.422 ± 0.093	1.541 ± 0.087	1.390 ± 0.074
1.345 ± 0.005	1.453 ± 0.090		
1.355 ± 0.005	1.373 ± 0.085		
1.365 ± 0.005	1.245 ± 0.076		
1.375 ± 0.005	1.565 ± 0.094		
1.385 ± 0.005			
1.395 ± 0.005			
1.405 ± 0.005			
1.415 ± 0.005			
1.425 ± 0.005			
1.435 ± 0.005			
1.445 ± 0.005			
1.455 ± 0.005			
1.465 ± 0.005			
1.475 ± 0.005			
1.485 ± 0.005			
1.495 ± 0.005			
1.505 ± 0.005			
1.515 ± 0.005			
1.525 ± 0.005			
1.535 ± 0.005			
1.545 ± 0.005			
1.555 ± 0.005			
1.565 ± 0.005			
1.575 ± 0.005			
1.585 ± 0.005			
1.595 ± 0.005			

Table D.7: Semi inclusive cross sections $d^2\sigma/dQ^2dW$ for $0.1875 \leq Q^2 \leq 0.2375\,(GeV/c)^2$ and $1.155 \leq W \leq 1.595\,GeV/c^2$.

W $\left[GeV/c^2\right]$	$d^2\sigma/dQ^2dW$ $\left[\mu b/GeV^3\right]$		
	Q^2 $\left[(GeV/c)^2\right]$		
	0.2625 ± 0.0125	0.2875 ± 0.0125	0.2375 ± 0.0125
1.155 ± 0.005	0.999 ± 0.077	0.747 ± 0.058	0.671 ± 0.052
1.165 ± 0.005	1.084 ± 0.082	0.841 ± 0.062	0.770 ± 0.056
1.175 ± 0.005	1.199 ± 0.086	0.965 ± 0.067	0.735 ± 0.054
1.185 ± 0.005	1.130 ± 0.080	1.089 ± 0.074	0.779 ± 0.057
1.195 ± 0.005	1.236 ± 0.084	1.029 ± 0.069	0.850 ± 0.058
1.205 ± 0.005	1.277 ± 0.084	1.193 ± 0.075	0.887 ± 0.060
1.215 ± 0.005	1.260 ± 0.082	1.128 ± 0.071	0.956 ± 0.062
1.225 ± 0.005	1.398 ± 0.089	1.173 ± 0.074	1.083 ± 0.069
1.235 ± 0.005	1.375 ± 0.083	1.290 ± 0.079	0.903 ± 0.057
1.245 ± 0.005	1.463 ± 0.087	1.233 ± 0.074	0.952 ± 0.059
1.255 ± 0.005	1.361 ± 0.081	1.170 ± 0.068	1.056 ± 0.062
1.265 ± 0.005	1.431 ± 0.082	1.223 ± 0.071	0.889 ± 0.054
1.275 ± 0.005	1.408 ± 0.080	1.140 ± 0.066	1.063 ± 0.063
1.285 ± 0.005	1.503 ± 0.083	1.140 ± 0.065	1.026 ± 0.059
1.295 ± 0.005	1.291 ± 0.071	1.121 ± 0.064	0.942 ± 0.055
1.305 ± 0.005	1.324 ± 0.073	1.096 ± 0.061	0.958 ± 0.055
1.315 ± 0.005	1.282 ± 0.069		0.973 ± 0.055
1.325 ± 0.005	1.366 ± 0.071		
1.335 ± 0.005	1.160 ± 0.063		
1.345 ± 0.005			
1.355 ± 0.005			
1.365 ± 0.005			
1.375 ± 0.005			
1.385 ± 0.005			
1.395 ± 0.005			
1.405 ± 0.005			
1.415 ± 0.005			
1.425 ± 0.005			
1.435 ± 0.005			
1.445 ± 0.005			
1.455 ± 0.005			
1.465 ± 0.005			
1.475 ± 0.005			
1.485 ± 0.005			
1.495 ± 0.005			
1.505 ± 0.005			
1.515 ± 0.005			
1.525 ± 0.005			
1.535 ± 0.005			
1.545 ± 0.005			
1.555 ± 0.005			
1.565 ± 0.005			
1.575 ± 0.005			
1.585 ± 0.005			
1.595 ± 0.005			

Table D.8: Semi inclusive cross sections $d^2\sigma/dQ^2dW$ for $0.2625 \leq Q^2 \leq 0.3125\,(GeV/c)^2$ and $1.155 \leq W \leq 1.595\,GeV/c^2$.

W $[GeV/c^2]$	$d^2\sigma/dQ^2dW$ $[\mu b/GeV^3]$		
	Q^2 $\left[(GeV/c)^2\right]$		
	0.225 ± 0.025	0.275 ± 0.025	0.325 ± 0.025
0.705 ± 0.005			
0.715 ± 0.005			
0.725 ± 0.005			
0.735 ± 0.005			
0.745 ± 0.005			
0.755 ± 0.005			
0.765 ± 0.005			
0.775 ± 0.005			
0.785 ± 0.005			
0.795 ± 0.005			
0.805 ± 0.005			
0.815 ± 0.005			
0.825 ± 0.005			
0.835 ± 0.005			
0.845 ± 0.005			
0.855 ± 0.005			
0.865 ± 0.005			
0.875 ± 0.005			
0.885 ± 0.005			
0.895 ± 0.005			
0.905 ± 0.005			
0.915 ± 0.005			
0.925 ± 0.005			
0.935 ± 0.005			
0.945 ± 0.005			
0.955 ± 0.005			
0.965 ± 0.005			
0.975 ± 0.005			
0.985 ± 0.005			
0.995 ± 0.005			
1.005 ± 0.005			
1.015 ± 0.005			
1.025 ± 0.005			
1.035 ± 0.005			
1.045 ± 0.005			
1.055 ± 0.005			
1.065 ± 0.005			
1.075 ± 0.005			0.226 ± 0.044
1.085 ± 0.005			0.183 ± 0.036
1.095 ± 0.005		0.334 ± 0.058	0.156 ± 0.030
1.105 ± 0.005		0.307 ± 0.049	0.225 ± 0.035
1.115 ± 0.005	0.570 ± 0.083	0.377 ± 0.052	0.224 ± 0.033
1.125 ± 0.005	0.586 ± 0.082	0.302 ± 0.041	0.213 ± 0.031
1.135 ± 0.005	0.638 ± 0.086	0.400 ± 0.048	0.260 ± 0.033
1.145 ± 0.005	0.756 ± 0.093	0.498 ± 0.054	0.315 ± 0.037

Table D.9: Exclusive cross sections $d^2\sigma/dQ^2dW$ for $0.225 \leq Q^2 \leq 0.325\,(GeV/c)^2$ and $0.705 \leq W \leq 1.145\,GeV/c^2$.

W $\left[GeV/c^2\right]$	$d^2\sigma/dQ^2dW$ $\left[\mu b/GeV^3\right]$	
	Q^2 $\left[(GeV/c)^2\right]$	
	0.375 ± 0.025	0.425 ± 0.025
0.705 ± 0.005		
0.715 ± 0.005		
0.725 ± 0.005		
0.735 ± 0.005		
0.745 ± 0.005		
0.755 ± 0.005		
0.765 ± 0.005		
0.775 ± 0.005		
0.785 ± 0.005		
0.795 ± 0.005		
0.805 ± 0.005		
0.815 ± 0.005		
0.825 ± 0.005		
0.835 ± 0.005		
0.845 ± 0.005		
0.855 ± 0.005		
0.865 ± 0.005		
0.875 ± 0.005		
0.885 ± 0.005		
0.895 ± 0.005		
0.905 ± 0.005		
0.915 ± 0.005		
0.925 ± 0.005		
0.935 ± 0.005		
0.945 ± 0.005		
0.955 ± 0.005		
0.965 ± 0.005		
0.975 ± 0.005		
0.985 ± 0.005		
0.995 ± 0.005		
1.005 ± 0.005		
1.015 ± 0.005		
1.025 ± 0.005		
1.035 ± 0.005		0.035 ± 0.016
1.045 ± 0.005		0.020 ± 0.010
1.055 ± 0.005	0.120 ± 0.030	0.085 ± 0.021
1.065 ± 0.005	0.102 ± 0.025	0.047 ± 0.015
1.075 ± 0.005	0.101 ± 0.024	0.054 ± 0.015
1.085 ± 0.005	0.076 ± 0.019	0.063 ± 0.015
1.095 ± 0.005	0.135 ± 0.026	0.066 ± 0.016
1.105 ± 0.005	0.144 ± 0.024	0.083 ± 0.017
1.115 ± 0.005	0.179 ± 0.027	0.103 ± 0.019
1.125 ± 0.005	0.134 ± 0.021	0.111 ± 0.019
1.135 ± 0.005	0.213 ± 0.028	0.137 ± 0.023
1.145 ± 0.005	0.238 ± 0.029	0.151 ± 0.022

Table D.10: Exclusive cross sections $d^2\sigma/dQ^2dW$ for $0.375 \leq Q^2 \leq 0.425\ (GeV/c)^2$ and $0.705 \leq W \leq 1.145\, GeV/c^2$.

W $\left[GeV/c^2\right]$	$d^2\sigma/dQ^2dW$ $\left[\mu b/GeV^3\right]$		
	Q^2 $\left[(GeV/c)^2\right]$		
	0.225 ± 0.025	0.275 ± 0.025	0.325 ± 0.025
1.155 ± 0.005	0.587 ± 0.064	0.573 ± 0.060	0.328 ± 0.037
1.165 ± 0.005	0.803 ± 0.081	0.560 ± 0.054	0.376 ± 0.040
1.175 ± 0.005	0.725 ± 0.076	0.521 ± 0.053	0.327 ± 0.035
1.185 ± 0.005	0.712 ± 0.068	0.588 ± 0.057	0.309 ± 0.033
1.195 ± 0.005	0.748 ± 0.070	0.550 ± 0.052	0.320 ± 0.034
1.205 ± 0.005	0.799 ± 0.075	0.536 ± 0.048	0.382 ± 0.037
1.215 ± 0.005	0.713 ± 0.061	0.478 ± 0.044	0.361 ± 0.034
1.225 ± 0.005	0.697 ± 0.060	0.482 ± 0.041	0.337 ± 0.033
1.235 ± 0.005	0.580 ± 0.051	0.503 ± 0.043	0.258 ± 0.027
1.245 ± 0.005	0.613 ± 0.053	0.443 ± 0.038	0.267 ± 0.027
1.255 ± 0.005	0.628 ± 0.054	0.454 ± 0.039	0.294 ± 0.028
1.265 ± 0.005	0.494 ± 0.043	0.396 ± 0.034	0.231 ± 0.023
1.275 ± 0.005	0.478 ± 0.041	0.404 ± 0.036	0.233 ± 0.023
1.285 ± 0.005	0.497 ± 0.044	0.332 ± 0.030	0.231 ± 0.023
1.295 ± 0.005	0.420 ± 0.036	0.276 ± 0.027	0.255 ± 0.025
1.305 ± 0.005	0.318 ± 0.030	0.283 ± 0.025	0.226 ± 0.022
1.315 ± 0.005	0.378 ± 0.034	0.246 ± 0.023	0.192 ± 0.020
1.325 ± 0.005	0.342 ± 0.031	0.270 ± 0.025	0.197 ± 0.022
1.335 ± 0.005	0.312 ± 0.028	0.199 ± 0.021	
1.345 ± 0.005	0.254 ± 0.025	0.196 ± 0.021	
1.355 ± 0.005	0.249 ± 0.025	0.249 ± 0.025	
1.365 ± 0.005	0.297 ± 0.027		
1.375 ± 0.005	0.249 ± 0.025		
1.385 ± 0.005	0.280 ± 0.028		
1.395 ± 0.005			
1.405 ± 0.005			
1.415 ± 0.005			
1.425 ± 0.005			
1.435 ± 0.005			
1.445 ± 0.005			
1.455 ± 0.005			
1.465 ± 0.005			
1.475 ± 0.005			
1.485 ± 0.005			
1.495 ± 0.005			
1.505 ± 0.005			
1.515 ± 0.005			
1.525 ± 0.005			
1.535 ± 0.005			
1.545 ± 0.005			
1.555 ± 0.005			
1.565 ± 0.005			
1.575 ± 0.005			
1.585 ± 0.005			
1.595 ± 0.005			

Table D.11: Exclusive cross sections $d^2\sigma/dQ^2dW$ for $0.225 \leq Q^2 \leq 0.325\ (GeV/c)^2$ and $0.155 \leq W \leq 1.595\,GeV/c^2$.

W $[GeV/c^2]$	$d^2\sigma/dQ^2dW$ $[\mu b/GeV^3]$	
	Q^2 $\left[(GeV/c)^2\right]$	
	0.375 ± 0.025	0.425 ± 0.025
1.155 ± 0.005	0.216 ± 0.026	0.124 ± 0.020
1.165 ± 0.005	0.225 ± 0.027	0.149 ± 0.021
1.175 ± 0.005	0.239 ± 0.029	0.143 ± 0.019
1.185 ± 0.005	0.206 ± 0.024	0.158 ± 0.021
1.195 ± 0.005	0.228 ± 0.025	0.150 ± 0.018
1.205 ± 0.005	0.289 ± 0.030	0.165 ± 0.021
1.215 ± 0.005	0.169 ± 0.020	0.144 ± 0.019
1.225 ± 0.005	0.179 ± 0.021	0.134 ± 0.018
1.235 ± 0.005	0.269 ± 0.027	0.135 ± 0.017
1.245 ± 0.005	0.191 ± 0.022	0.115 ± 0.016
1.255 ± 0.005	0.210 ± 0.023	0.147 ± 0.018
1.265 ± 0.005	0.179 ± 0.020	0.108 ± 0.015
1.275 ± 0.005	0.156 ± 0.019	0.106 ± 0.015
1.285 ± 0.005	0.162 ± 0.019	0.078 ± 0.013
1.295 ± 0.005		
1.305 ± 0.005		
1.315 ± 0.005		
1.325 ± 0.005		
1.335 ± 0.005		
1.345 ± 0.005		
1.355 ± 0.005		
1.365 ± 0.005		
1.375 ± 0.005		
1.385 ± 0.005		
1.395 ± 0.005		
1.405 ± 0.005		
1.415 ± 0.005		
1.425 ± 0.005		
1.435 ± 0.005		
1.445 ± 0.005		
1.455 ± 0.005		
1.465 ± 0.005		
1.475 ± 0.005		
1.485 ± 0.005		
1.495 ± 0.005		
1.505 ± 0.005		
1.515 ± 0.005		
1.525 ± 0.005		
1.535 ± 0.005		
1.545 ± 0.005		
1.555 ± 0.005		
1.565 ± 0.005		
1.575 ± 0.005		
1.585 ± 0.005		
1.595 ± 0.005		

Table D.12: Exclusive cross sections $d^2\sigma/dQ^2dW$ for $0.375 \leq Q^2 \leq 0.425\ (GeV/c)^2$ and $0.155 \leq W \leq 1.595\,GeV/c^2$.

$M_{p\pi^-}$ $[GeV/c^2]$	$d^2\sigma/dQ^2dM_{p\pi^-}$ $[\mu b/GeV^3]$			
	Q^2 $\left[(GeV/c)^2\right]$			
	0.175 ± 0.025	0.225 ± 0.025	0.275 ± 0.025	0.325 ± 0.025
0.705 ± 0.005				
0.715 ± 0.005				
0.725 ± 0.005				
0.735 ± 0.005				
0.745 ± 0.005				
0.755 ± 0.005				
0.765 ± 0.005				
0.775 ± 0.005				
0.785 ± 0.005				
0.795 ± 0.005				
0.805 ± 0.005				
0.815 ± 0.005				
0.825 ± 0.005				
0.835 ± 0.005				
0.845 ± 0.005				
0.855 ± 0.005				
0.865 ± 0.005				
0.875 ± 0.005				
0.885 ± 0.005				
0.895 ± 0.005				
0.905 ± 0.005				
0.915 ± 0.005				
0.925 ± 0.005				
0.935 ± 0.005				
0.945 ± 0.005				
0.955 ± 0.005				
0.965 ± 0.005				
0.975 ± 0.005				
0.985 ± 0.005				
0.995 ± 0.005				
1.005 ± 0.005				
1.015 ± 0.005				
1.025 ± 0.005				
1.035 ± 0.005				
1.045 ± 0.005				
1.055 ± 0.005				
1.065 ± 0.005				
1.075 ± 0.005				
1.085 ± 0.005				
1.095 ± 0.005				
1.105 ± 0.005				
1.115 ± 0.005	0.688 ± 0.116	0.883 ± 0.096	0.729 ± 0.084	0.462 ± 0.061
1.125 ± 0.005	0.546 ± 0.077	0.979 ± 0.095	0.666 ± 0.067	0.480 ± 0.057
1.135 ± 0.005	0.601 ± 0.084	0.825 ± 0.078	0.641 ± 0.064	0.454 ± 0.049
1.145 ± 0.005	0.443 ± 0.058	0.878 ± 0.076	0.691 ± 0.063	0.484 ± 0.049

Table D.13: Exclusive cross sections $d^2\sigma/dQ^2dM_{p\pi^-}$ for $0.175 \leq Q^2 \leq 0.325$ $(GeV/c)^2$ and $0.705 \leq M_{p\pi^-} \leq 1.145\,GeV/c^2$.

$M_{p\pi^-}$ $\left[GeV/c^2\right]$	$d^2\sigma/dQ^2dM_{p\pi^-}$ $\left[\mu b/GeV^3\right]$ Q^2 $\left[(GeV/c)^2\right]$		
	0.375 ± 0.025	0.425 ± 0.025	0.475 ± 0.025
0.705 ± 0.005			
0.715 ± 0.005			
0.725 ± 0.005			
0.735 ± 0.005			
0.745 ± 0.005			
0.755 ± 0.005			
0.765 ± 0.005			
0.775 ± 0.005			
0.785 ± 0.005			
0.795 ± 0.005			
0.805 ± 0.005			
0.815 ± 0.005			
0.825 ± 0.005			
0.835 ± 0.005			
0.845 ± 0.005			
0.855 ± 0.005			
0.865 ± 0.005			
0.875 ± 0.005			
0.885 ± 0.005			
0.895 ± 0.005			
0.905 ± 0.005			
0.915 ± 0.005			
0.925 ± 0.005			
0.935 ± 0.005			
0.945 ± 0.005			
0.955 ± 0.005			
0.965 ± 0.005			
0.975 ± 0.005			
0.985 ± 0.005			
0.995 ± 0.005			
1.005 ± 0.005			
1.015 ± 0.005			
1.025 ± 0.005			
1.035 ± 0.005			
1.045 ± 0.005			
1.055 ± 0.005			
1.065 ± 0.005			
1.075 ± 0.005			
1.085 ± 0.005			
1.095 ± 0.005			
1.105 ± 0.005			
1.115 ± 0.005	0.435 ± 0.060	0.227 ± 0.043	0.141 ± 0.032
1.125 ± 0.005	0.429 ± 0.056	0.208 ± 0.035	0.146 ± 0.030
1.135 ± 0.005	0.359 ± 0.043	0.233 ± 0.035	0.118 ± 0.025
1.145 ± 0.005	0.336 ± 0.039	0.232 ± 0.034	0.158 ± 0.026

Table D.14: Exclusive cross sections $d^2\sigma/dQ^2dM_{p\pi^-}$ for $0.375 \leq Q^2 \leq 0.475$ $(GeV/c)^2$ and $0.705 \leq M_{p\pi^-} \leq 1.145\, GeV/c^2$.

$M_{p\pi^-}$ $[GeV/c^2]$	$d^2\sigma/dQ^2dM_{p\pi^-}$ $[\mu b/GeV^3]$			
	Q^2 $\left[(GeV/c)^2\right]$			
	0.175 ± 0.025	0.225 ± 0.025	0.275 ± 0.025	0.325 ± 0.025
1.155 ± 0.005	0.700 ± 0.087	0.927 ± 0.075	0.714 ± 0.061	0.477 ± 0.047
1.165 ± 0.005	0.593 ± 0.069	0.751 ± 0.061	0.669 ± 0.053	0.586 ± 0.051
1.175 ± 0.005	0.568 ± 0.064	1.008 ± 0.080	0.826 ± 0.064	0.514 ± 0.045
1.185 ± 0.005	0.699 ± 0.078	0.849 ± 0.067	0.744 ± 0.056	0.546 ± 0.047
1.195 ± 0.005	0.619 ± 0.067	0.973 ± 0.074	0.732 ± 0.057	0.557 ± 0.046
1.205 ± 0.005	0.633 ± 0.070	0.960 ± 0.072	0.740 ± 0.058	0.496 ± 0.042
1.215 ± 0.005	0.556 ± 0.061	0.773 ± 0.060	0.655 ± 0.050	0.434 ± 0.038
1.225 ± 0.005	0.584 ± 0.063	0.772 ± 0.060	0.702 ± 0.054	0.458 ± 0.040
1.235 ± 0.005	0.419 ± 0.044	0.714 ± 0.058	0.603 ± 0.050	0.472 ± 0.040
1.245 ± 0.005	0.443 ± 0.049	0.567 ± 0.047	0.510 ± 0.044	0.411 ± 0.038
1.255 ± 0.005	0.375 ± 0.042	0.546 ± 0.046	0.414 ± 0.038	0.278 ± 0.029
1.265 ± 0.005	0.322 ± 0.039	0.451 ± 0.042	0.347 ± 0.033	0.299 ± 0.032
1.275 ± 0.005	0.331 ± 0.039	0.413 ± 0.037	0.403 ± 0.038	0.165 ± 0.021
1.285 ± 0.005	0.196 ± 0.025	0.420 ± 0.040	0.321 ± 0.031	0.263 ± 0.030
1.295 ± 0.005	0.232 ± 0.029	0.313 ± 0.033	0.267 ± 0.029	0.191 ± 0.023
1.305 ± 0.005	0.228 ± 0.030	0.277 ± 0.030	0.217 ± 0.025	0.176 ± 0.022
1.315 ± 0.005	0.229 ± 0.030	0.349 ± 0.036	0.279 ± 0.030	0.221 ± 0.027
1.325 ± 0.005	0.233 ± 0.031	0.307 ± 0.034	0.219 ± 0.026	0.153 ± 0.021
1.335 ± 0.005	0.251 ± 0.032	0.323 ± 0.036	0.200 ± 0.025	0.126 ± 0.019
1.345 ± 0.005	0.167 ± 0.024	0.242 ± 0.028	0.165 ± 0.023	0.128 ± 0.019
1.355 ± 0.005	0.218 ± 0.030	0.244 ± 0.030	0.132 ± 0.020	0.147 ± 0.022
1.365 ± 0.005	0.227 ± 0.031	0.223 ± 0.028	0.120 ± 0.019	0.124 ± 0.020
1.375 ± 0.005	0.173 ± 0.027	0.213 ± 0.028	0.158 ± 0.024	0.095 ± 0.018
1.385 ± 0.005	0.161 ± 0.026	0.231 ± 0.029	0.106 ± 0.018	0.091 ± 0.017
1.395 ± 0.005	0.181 ± 0.028	0.187 ± 0.026	0.118 ± 0.021	0.091 ± 0.018
1.405 ± 0.005	0.152 ± 0.025	0.239 ± 0.032	0.138 ± 0.023	0.076 ± 0.017
1.415 ± 0.005	0.170 ± 0.030	0.180 ± 0.026	0.125 ± 0.021	0.055 ± 0.014
1.425 ± 0.005	0.162 ± 0.026	0.201 ± 0.029	0.118 ± 0.021	0.113 ± 0.021
1.435 ± 0.005	0.189 ± 0.033	0.243 ± 0.036	0.138 ± 0.025	0.071 ± 0.016
1.445 ± 0.005	0.187 ± 0.035	0.166 ± 0.028	0.115 ± 0.023	0.051 ± 0.014
1.455 ± 0.005	0.154 ± 0.028	0.183 ± 0.030	0.147 ± 0.028	0.064 ± 0.017
1.465 ± 0.005	0.195 ± 0.036	0.128 ± 0.025	0.102 ± 0.022	0.066 ± 0.020
1.475 ± 0.005	0.238 ± 0.045	0.162 ± 0.028	0.082 ± 0.019	0.037 ± 0.013
1.485 ± 0.005	0.155 ± 0.032	0.110 ± 0.022	0.098 ± 0.023	0.037 ± 0.013
1.495 ± 0.005	0.136 ± 0.030	0.164 ± 0.031	0.099 ± 0.025	0.059 ± 0.018
1.505 ± 0.005	0.143 ± 0.033	0.067 ± 0.019	0.103 ± 0.027	0.022 ± 0.011
1.515 ± 0.005	0.136 ± 0.033	0.091 ± 0.025	0.084 ± 0.023	0.048 ± 0.017
1.525 ± 0.005	0.138 ± 0.036	0.113 ± 0.030	0.042 ± 0.016	0.007 ± 0.007
1.535 ± 0.005	0.056 ± 0.021	0.038 ± 0.016	0.062 ± 0.023	0.016 ± 0.012
1.545 ± 0.005	0.068 ± 0.021	0.069 ± 0.022	0.031 ± 0.016	0.039 ± 0.018
1.555 ± 0.005	0.030 ± 0.016			0.013 ± 0.010
1.565 ± 0.005		0.053 ± 0.021		0.021 ± 0.012
1.575 ± 0.005	0.044 ± 0.019	0.031 ± 0.016	0.008 ± 0.008	0.014 ± 0.010
1.585 ± 0.005	0.035 ± 0.017		0.013 ± 0.009	
1.595 ± 0.005	0.008 ± 0.008	0.008 ± 0.008	0.007 ± 0.007	0.007 ± 0.008

Table D.15: Exclusive cross sections $d^2\sigma/dQ^2dM_{p\pi^-}$ for $0.175 \leq Q^2 \leq 0.325$ $(GeV/c)^2$ and $1.155 \leq M_{p\pi^-} \leq 1.595\,GeV/c^2$.

$M_{p\pi^-}$ $\left[GeV/c^2\right]$	$d^2\sigma/dQ^2dM_{p\pi^-}$ $\left[\mu b/GeV^3\right]$ Q^2 $\left[(GeV/c)^2\right]$		
	0.375 ± 0.025	0.425 ± 0.025	0.475 ± 0.025
1.155 ± 0.005	0.359 ± 0.038	0.242 ± 0.032	0.147 ± 0.024
1.165 ± 0.005	0.375 ± 0.040	0.219 ± 0.029	0.131 ± 0.022
1.175 ± 0.005	0.434 ± 0.042	0.247 ± 0.030	0.195 ± 0.027
1.185 ± 0.005	0.451 ± 0.042	0.289 ± 0.032	0.148 ± 0.023
1.195 ± 0.005	0.376 ± 0.036	0.292 ± 0.031	0.162 ± 0.023
1.205 ± 0.005	0.415 ± 0.037	0.266 ± 0.029	0.148 ± 0.022
1.215 ± 0.005	0.376 ± 0.035	0.240 ± 0.027	0.163 ± 0.023
1.225 ± 0.005	0.339 ± 0.033	0.219 ± 0.027	0.174 ± 0.023
1.235 ± 0.005	0.234 ± 0.026	0.174 ± 0.022	0.121 ± 0.019
1.245 ± 0.005	0.254 ± 0.028	0.208 ± 0.026	0.109 ± 0.019
1.255 ± 0.005	0.201 ± 0.024	0.126 ± 0.019	0.087 ± 0.016
1.265 ± 0.005	0.213 ± 0.025	0.116 ± 0.018	0.067 ± 0.013
1.275 ± 0.005	0.157 ± 0.020	0.134 ± 0.019	0.041 ± 0.011
1.285 ± 0.005	0.147 ± 0.019	0.075 ± 0.014	0.045 ± 0.011
1.295 ± 0.005	0.161 ± 0.022	0.078 ± 0.015	0.030 ± 0.009
1.305 ± 0.005	0.104 ± 0.016	0.070 ± 0.014	0.028 ± 0.009
1.315 ± 0.005	0.103 ± 0.017	0.042 ± 0.011	0.042 ± 0.011
1.325 ± 0.005	0.125 ± 0.018	0.074 ± 0.015	0.024 ± 0.009
1.335 ± 0.005	0.115 ± 0.018	0.058 ± 0.013	0.035 ± 0.011
1.345 ± 0.005	0.097 ± 0.018	0.042 ± 0.011	0.032 ± 0.010
1.355 ± 0.005	0.083 ± 0.016	0.056 ± 0.013	0.032 ± 0.010
1.365 ± 0.005	0.075 ± 0.015	0.033 ± 0.010	0.011 ± 0.006
1.375 ± 0.005	0.070 ± 0.015	0.032 ± 0.010	0.015 ± 0.007
1.385 ± 0.005	0.070 ± 0.015	0.026 ± 0.009	0.011 ± 0.007
1.395 ± 0.005	0.047 ± 0.013	0.014 ± 0.007	0.011 ± 0.007
1.405 ± 0.005	0.045 ± 0.012	0.021 ± 0.009	0.009 ± 0.006
1.415 ± 0.005	0.031 ± 0.010	0.007 ± 0.005	0.013 ± 0.008
1.425 ± 0.005	0.033 ± 0.011	0.011 ± 0.007	0.011 ± 0.008
1.435 ± 0.005	0.047 ± 0.014	0.020 ± 0.009	
1.445 ± 0.005	0.031 ± 0.011	0.010 ± 0.007	0.034 ± 0.014
1.455 ± 0.005	0.037 ± 0.012	0.022 ± 0.010	
1.465 ± 0.005	0.034 ± 0.012	0.014 ± 0.008	
1.475 ± 0.005	0.026 ± 0.012	0.006 ± 0.006	
1.485 ± 0.005	0.031 ± 0.012	0.012 ± 0.008	
1.495 ± 0.005	0.031 ± 0.013	0.006 ± 0.006	
1.505 ± 0.005	0.018 ± 0.010	0.006 ± 0.006	
1.515 ± 0.005	0.007 ± 0.007	0.008 ± 0.008	
1.525 ± 0.005	0.007 ± 0.007		
1.535 ± 0.005	0.008 ± 0.008		
1.545 ± 0.005			
1.555 ± 0.005			
1.565 ± 0.005			
1.575 ± 0.005			
1.585 ± 0.005			
1.595 ± 0.005			

Table D.16: Exclusive cross sections $d^2\sigma/dQ^2dM_{p\pi^-}$ for $0.375 \leq Q^2 \leq 0.475$ $(GeV/c)^2$ and $1.155 \leq M_{p\pi^-} \leq 1.595\, GeV/c^2$.

Bibliography

[1] T. Ericson and W. Weise. *Pions and Nuclei*. Oxford Science Publications, 1988.

[2] G. Cattapan and L. S. Ferreira. The role of the Δ in nuclear physics. *Physics Reports*, 362:303–407, 2002.

[3] R. M. Sealock et al. Electroexcitation of the $\Delta(1232)$ in nuclei. *Physical Review Letters*, 62(12):1350–1353, March 1989.

[4] Kenneth S. Krane. *Introductory Nuclear Physics*. John Wiley & Sons, 1988.

[5] J. S. O' Connell and R. M. Sealock. Phenomenological Δ-nucleus potential from inclusive electron-nucleus scattering data. *Physical Review C*, 42(6):2290–2294, December 1990.

[6] H. P. Blok. Electron scattering. Lecture Notes.

[7] Donald H. Perkins. *Introduction to High Energy Physics*. Addison-Wesley, third edition, 1987.

[8] Particle physics booklet. Extracted from the Review of particle physics.

[9] J. H. Koch and N. Ohtsuka. Inclusive electron scattering from light nuclei at intermediate energies. *Nuclear Physics A*, 435:765–790, 1984.

[10] H. Kim, S. Schramm and S. H. Lee. $\Delta(1232)$ decay in the nuclear medium. *Physical Review C*, 56(3):1582–1587, September 1997.

[11] Y. I. Titov et al. *Soviet Journal of Nuclear Physics*, 9:772, 1969.

[12] Y. I. Titov et al. Electroproduction of pions on proton. *Soviet Journal of Nuclear Physics*, 11:145, 1970.

[13] Y. I. Titov et al. Experimental study of pion electroproduction mechanism on complex nuclei. *Soviet Journal of Nuclear Physics*, 12:660, 1971.

[14] Y. I. Titov et al. Inelastic scattering of electrons on protons and the ^6Li nucleus. *Soviet Journal of Nuclear Physics*, 15:361, 1972.

[15] F. H. Heimlich et al. High energy scattering from ^{6}Li and ^{12}C. *Nuclear Physics A*, 231:509–520, 1974.

[16] U. Glawe, U. Strohbusch et al. High energy electron scattering on ^{6}Li and ^{12}C as an incoherent superposition of single nucleon processes. *Physics Letters*, 89B(1):44–47, December 1979.

[17] P. Barreau et al. Deep-inelastic electron scattering from carbon. *Nuclear Physics A*, 402:515–540, 1983.

[18] J. S. O' Connell et al. Electron scattering in excitation region of the Δ resonance on nuclei with $A = 1$ to 16. *Physical Review Letters*, 53(17):1627–1629, October 1984.

[19] J. S. O' Connell et al. Electromagnetic excitation of the Δ resonance in nuclei. *Physical Review C*, 35(3):1063–1071, March 1987.

[20] Z. E. Meziani et al. Transverse response functions in deep-inelastic electron scattering for ^{40}Ca, ^{48}Ca, and ^{56}Fe. *Physical Review Letters*, 54(12):1233–1236, March 1985.

[21] D. T. Barran et al. Δ electroproduction and inelastic charge scattering from carbon and iron. *Physical Review Letters*, 61(4):400–403, July 1988.

[22] P. Leconte et al. The electron scattering facility at the Saclay 600 MeV linear accelerator. *Nuclear Instruments and Methods*, 169:401–412, 1980.

[23] M. Cantin et al. Silica aerogels used as Cherenkov radiators. *Nuclear Instruments and Methods*, 118:177–182, 1974.

[24] J. Arends et al. Measurement of total photonuclear cross sections in the Δ-resonance region. *Physics Letters B*, 98B:423–426, 1981.

[25] J. Haimson. *Linear Accelerators*, chapter B.3.2, pages 415–470. 1969.

[26] J. Haimson. Initial operation of the mit electron linear accelerator. *IEEE Transactions on Nuclear Science*, 20:914–918, 1973.

[27] P. C. Dunn et al. ^{3}He magnetic form factor. *Physical Review C*, 27:71–82, 1983.

[28] W. Bertozzi et al. Focal plane instrumentation: a very high resolution MWPC system for inclined tracks. *Nuclear Instruments and Methods*, 141:457–476, 1977.

[29] W. Bertozzi et al. High resolution spectrometers for electron scattering. *Nuclear Instruments and Methods*, 162:211–238, 1979.

[30] R. Anderson, D. Gustavson, R. Prepost and D. Ritson. 1.6 GeV/c charged particle spectrometer facility at the Stanford Linear Accelerator Center. *Nuclear Instruments and Methods*, 66:328–335, 1968.

[31] R. M. Sealock. Electroexcitation of the $\Delta(1232)$ in nuclei. CEBAF Proposal.

[32] M. Danos and H. T. Williams. Shell model for the interaction of the Δ_{33} with the nucleus. *Physics Letters*, 89B:169–172, 1980.

[33] Y. Horikawa, M. Thies and F. Lenz. The Δ-nucleus spin-orbit interaction in π-nucleus scattering. *Nuclear Physics A*, 345:386–408, 1980.

[34] R. W. Lourie et al. Reaction $^{12}C(e,e'p)$ in the dip region. *Physical Review Letters*, 56:2364–2367, 1986.

[35] H. Baghaei et al. Electroexcitation of the Δ resonance in the $(e,e'p)$ reaction. *Physical Review C*, 39(1):177–180, January 1989.

[36] L. B. Weinstein et al. Quasielastic reaction mechanism studied using the reaction $^{12}C(e,e'p)$. *Physical Review Letters*, 64(14):1646–1649, April 1990.

[37] L. B. Weinstein. PhD thesis, MIT, 1988.

[38] D. Branford et al. Investigation of Δ-medium effects using the $^4He(\gamma,\pi^+n)^3He$ and $^4He(\gamma,\pi^+p)nnn$ reactions. *Physical Review C*, 66:015208, 2002.

[39] M. Liang et al. $^{12}C(\gamma,\pi^+n)$ and $^{12}C(\gamma,\pi^+p)$ reactions across the Δ resonance region. *Physics Letters B*, 411:244–248, October 1997.

[40] J. A. MacKenzie et al. Quasifree π^+ production studied using the $^{12}C(\gamma,\pi^+n)^{11}B$ reaction in the $\Delta(1232)$ resonance region. *Physical Review C*, 54(1):R6–R9, July 1996.

[41] A. Bodek et al. Experimental studies of the neutron and proton electromagnetic structure functions. *Physical Review D*, 20(7):1471–1552, October 1979.

[42] B. A. Mecking et al. The CEBAF Large Acceptance Spectrometer. Draft.

[43] W. Ingram. *Semi-exclusive studies of* $\Delta(1232)$ *electroproduction in* ^3He. PhD thesis, University of Glasgow, 2002. Submitted.

[44] Gayle Sundeen-Coleman. Accelerator division. http://www.jlab.org/accel/.

[45] M. D. Mestayer, D. S. Carman et al. The CLAS drift chamber system. *Nuclear Instruments and Methods A*, 449:81–111, 2000.

[46] G. Adams et al. The CLAS Cherenkov detector. *Nuclear Instruments and Methods A*, 465:414–427, 2001.

[47] B. Zhang. *Searching for Short Range Correlations Using* $(e, e'NN)$ *Reactions*. PhD thesis, Massachusetts Institute of Technology, 2003.

[48] E. S. Smith et al. The time-of-flight system for CLAS. *Nucl. Instr. Meth. A*, 432:265–298, 1999.

[49] M. Amarian et al. The CLAS forward electromagnetic calorimeter. *Nuclear Instruments and Methods A*, 460:239–265, 2001.

[50] D. Protopopescu. *A Survey of Beam Asymmetries in Semi-Exclusive Electron Scattering on* ^4He *and* ^{12}C. PhD thesis, University of New Hampshire, 2002.

[51] R. Niyazov. PhD thesis, Old Dominion University, 2002.

[52] A. V. Vlassov, V. A. Serov and A. V. Stavinsky. Jefferson Laboratory, 1999. CLAS-NOTE 1999-005.

[53] A. V. Vlassov. CC Calibration. http://www.jlab.org/∼vlassov/cc/index.html.

[54] D. Lawrence et al. CLAS Drift Chamber Calibration: Software and Procedures. Jefferson Laboratory, 1999. CLAS-NOTE 1999-018.

[55] E. S. Smith et al. Calibration of the CLAS TOF System. Jefferson Laboratory, 1999. CLAS-NOTE 1999-011.

[56] R. Niyazov and L. B. Weinstein. Fiducial Cut for Positive Hadrons in CLAS/E2 Data at 4.4 GeV. Jefferson Laboratory, 2001. CLAS-NOTE 2001-013.

[57] W. Brooks and D. Rowntree. CLAS acceptance calculations: basic principles, recommended procedures. Draft release, October 2001.

[58] E. Byckling and K. Kajantie. *Particle Kinematics*. Wiley-Interscience, 1973.

[59] M. Holtrop. CLAS GEANT Simulation - GSIM. http://improv.unh.edu/Maurik/gsim_info.shtml.

[60] N. Dashyan. Targets for CLAS/E2a runs. http://www.jlab.org/Hall-B/secure/e2/natasha/target/.

[61] Stepan Stepanyan. Private communication. February 2001.

[62] J. W. Lightbody, Jr and J. S. O' Connell. *Computational Physics*, 2(3):57, 1988.

[63] G. D'Agostini. A multidimensional unfolding method based on Bayes' theorem. *Nucl. Instr. Meth. A*, 362:487–498, 1995.

[64] D. G. Ireland. Private communication. March 2002.